Master Thesis

Near field enhancement of optical transition in carbon nanotubes

Graduate School of Science, Tohoku University
Department of Physics

Piyawath Tapsanit

2012

Acknowledgements

I would like to thank Prof. Riichiro Saito for his guidance during my two years Master course in physics. He has taught me physics in the way of deep understanding. He has tried very hard to direct me in the correct way of physics.I am very grateful to him. I would like to express my gratitude to Dr. Kentaro Sato who help me a lot in this thesis. He gave me very nice and kind discussions about the carbon nanotube and exciton in carbon nanotube. He always guide me when I have some problems. I am also very much grateful Dr. Jie Jiang (past member of our group) who have developed the exciton program to calculate the exciton energies and the wavefunctions in carbon nanotube. His papers frequently cited in this thesis help me a lot to understand the exciton in carbon nanotube. I am very thankful to Dr. Rihei Endo (past memeber of ourgroup) who have a discussion to me about the electromagnetism. I also would like to thank my beloved friends in our group : A.R.T Nugraha, E. H. Hasdeo, and Y. Tatsumi. We have read Raman book and the group theory book together every week. Nugraha-san and Hasdeo hepled me a lot to prepare the thesis presentation and this thesis. I want to thank Dr. Wataru Izumida who have been motivating me to do good research. I am very much grateful to Ms. Wako Yoko and Ms. Setsuko Sumino for their kind help and cooperation in praparing many official documents. I expressed my gratitude to DPST for providing me scholarship from Thailand during my Master course.

Contents

Chapter 1

Introduction

1.1 Preface

In theory of electromagnetic radiation, near field is the name used to call the solution of the Maxwell's equations that is localized near the radiating source. The amplitude of the near field diminishes by $1/r^3$ as distance r from the source increases. Therefore, the energy of the near field does not propagate out from the source, but it merely decays. Unlike the near field, far field refers to the solution of Maxwell's equations which behaves as the radiation field carrying the energy out of the source. The amplitude of the far field is proportional to $1/r$, thus it is weak in the region near the source. We call the region of $kr \ll 1$ as near field region. In the near field region, the localized near field plays a more important role than the far field because its amplitude is large compared to that of the far field. The experiment called tip-enhanced Raman spectroscopy (TERS) makes use of the near field generated by a metallic tip (e.g., Ag or Au tip) to make a spectroscopic image of a single wall carbon nanotube (SWNT) [13, 14]. A SWNT is a rolled up hexagonal sheet of carbon atoms, which becomes a one-dimensional material with the small diameter about 1-2 nm [16]. It is impossible to make an image of the SWNT in conventional spectroscopic experiments due to the diffraction limit of light, which gives that the spatial resolution Δx can not be smaller than $\lambda/2$ [15].

Another important result from TERS experiment besides imaging is that the

Raman signal becomes enhanced [13, 17]. Hartschuh *et al.* has shown that the enhancement of the Raman signal resulting from the near field localized at the tip apex by changing the distance between the metallic tip and the SWNT [13]. The amplitude of the near field scattered from the metallic tip is very large compared to the amplitude of the external laser light which have been shown by solving the Maxwell's equations for the cone shape of the metallic tip using the numerical method called finite difference time domain method (FDTD) [18]. Therefore, it is believed that the enhancement of the Raman signal is due to the enhancement of the near field. However, the quantitative calculation of the enhancement of the Raman spectra have not been discussed much yet. Thus it is important to quantitatively calculate the enhancement of the Raman signal and the optical matrix element of the interaction between the near field and the exciton in carbon nanotube. The near field radiated from the metallic tip due to the excitation of the laser light should be modeled and calculated to optimize the appropriate wavelength of the laser light and the appropriate size of the tip apex, because it has been shown experimentally and numerically that the near field enhancement depends on the radius of the tip apex [19, 18].

1.2 Purpose of the study

The purpose of this thesis is (i) to model a metallic tip as a metallic sphere with the same radius as the tip apex, and then to calculate the near field enhancement of the scattered wave radiating out from the metallic spheres (e.g., Ag and Au), and (ii) to calculate the near field enhancement of optical transition in SWNTs. The near field is obtained by solving Maxwell's equations in the spherical coordinate, and the near field enhancement of various wavelength and several diameters of Ag and Au spheres are given. The exciton-photon matrix element proposed by Jiang et *al.* [8] has been modified for the near field. The enhancement of optical matrix elements are discussed and compared with TERS experiment.

1.3 Organization

The organization of this thesis is as follows: The basic backgrounds, that are, (i) review of carbon nanotubes (SWNTs), (ii) concept and experimental facts of excitons in SWNTs, (iii) TERS experiment, (iv) effective enhancement factor, (v) scattering of light by a metallic sphere, and (vi) optical properties of noble metals are reviewed in the remaining part of the chapter 1. In chapter 2, the classical theory of the scattering of light by a metallic sphere known as Mie's theory is explained systematically. The quasi-static approximation and the dynamic depolarization are also added in the chapter 2 in order to understand the near field enhancement from Mie's theory. The exciton theory in carbon nanotube is also described in the chapter 2. In chapter 3, the formulation of the exciton-near field matrix element is described. In chapter 4, the calculation results of the exciton-near field matrix elements of SWNTS have been discussed.

1.4 Background

This section gives a review of SWNTs, basic of excitons in SWNTs, the experimental results of TERS experiment, the definition of effective enhancement factor, concept of Mie's theory, and lastly the optical properties of noble metals.

1.4.1 Review of carbon nanotube

A single wall carbon nanotube (SWNT) is a one-dimentional carbon material whose structure is considered as the rolled up sheet of graphene. One $2s$ valence electron and two $2p$ valence electrons of a carbon atom in the unrolled graphene sheet make sp^2 hybridization giving three sp^2 orbitals. Then each carbon atom forms three covalent bonds with three nearest neighbor atoms in the graphene plane [1]. The properties of a SWNT are determined by the chirality indices n and m of the chiral vector $\boldsymbol{C}_h$ defined as $\boldsymbol{C}_h = n\boldsymbol{a}_1 + m\boldsymbol{a}_2 = (n, m)$, where $\boldsymbol{a}_1 = (\frac{\sqrt{3}}{2}, \frac{1}{2})a$ and $\boldsymbol{a}_2 = (\frac{\sqrt{3}}{2}, -\frac{1}{2})a$ are lattice unit vectors of the graphene lattice, with the lattice constant $a = 0.246$ nm as

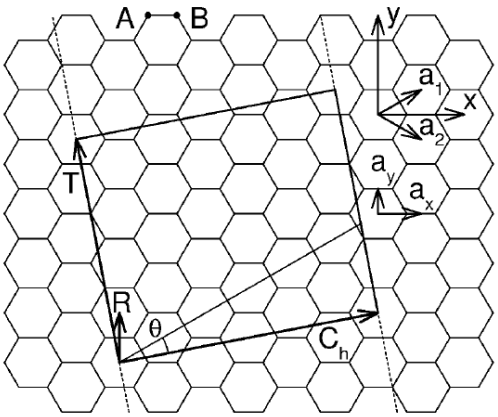

Figure 1-1: **Chiral index C_h and the unrolled unit cell of** $(4, 2)$ **carbon nanotube [2].** x and y axes are defined in armchair and zigzag direction. $\boldsymbol{a}_1$ and $\boldsymbol{a}_2$ are unit lattice vectors of graphene lattice. The rectangle bounded by vectors $\boldsymbol{C}_h$ and $\boldsymbol{T}$ is the unrolled unit cell of the carbon nanotube.

shown in Fig. 1-1 [16]. The chiral vector $\boldsymbol{C}_h = (4, 2)$ is shown in Fig. 1-1. Other important quantities of a SWNT are tube diameter $d_{\rm t}$ and chiral angle θ, whose values can be obtained from the chirality indices as $d_{\rm t} = a\sqrt{n^2 + nm + m^2}/\pi$ and $\tan\theta = \sqrt{3}m/(2n+m)$, respectively. If $n = m$, a SWNT is called an armchair carbon nanotube , with corresponding chiral angle $\theta = \pi/6$. If $n \neq 0$ and $m = 0$, chiral angle becomes $\theta = 0$ and a SWNT is called a zigzag carbon nanotube. Armchair and zigzag carbon nanotubes are both called achiral carbon nanotubes. However, if the chiral angle θ is in between these two values $(0 < \theta < \pi/6)$, a SWNT corresponding to this chirality is called a chiral carbon nanotube [16]. The unit cell of the carbon nanotube is translated periodically along tube axis by a translational vector $\boldsymbol{T} = t_1\boldsymbol{a}_1 + t_2\boldsymbol{a}_2 = (t_1, t_2)$ where $t_1 = \frac{2m+n}{d_R}$ and $t_1 = -\frac{2m+n}{d_R}$. d_R is obtained by $d_R = \gcd(2n+m, 2m+n)$ where gcd is an integer function of the greatest common divisor. For example, the armchair carbon nanotube (n, n) has $d_R = (3n, 3n) = 3n$, thus the translational vector becomes $\boldsymbol{T} = (1, -1)$. The unrolled carbon nanotube unit cell is the rectangle bound by the chiral vector $\boldsymbol{C}_h$ and the translational vector $\boldsymbol{T}$, as shown in Fig. 1-1 for a $(4, 2)$ chiral carbon nanotube. The number of graphene lattices in the carbon nanotube unit cell N is calculated by the area of the carbon nanotube unit cell

Fig. 1-1: fig:/fig:SWNT-Ch.eps

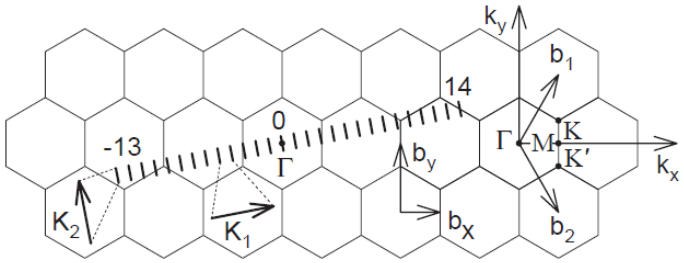

Figure 1-2: **Reciprocal lattice of graphene and cutting lines of (4,2) carbon nanotube [2].** $\boldsymbol{b}_1$ and $\boldsymbol{b}_2$ are the reciprocal lattice unit vectors of graphene lattice. Four symmetry points, Γ, M, K and K', are defined as the center, the middle and the corners points of the first Brillouin zone of graphene lattice, respectively. $\boldsymbol{K}_1$ and $\boldsymbol{K}_2$ are the reciprocal lattice unit vectors of carbon nanotube in circumferential and tube axis directions, respectively. The cutting line index μ runs from -13 to 14 passing through the Γ point at $\mu = 0$. The number of cutting lines is the same as the number of graphene lattices in carbon nanotube unit cell.

$|\boldsymbol{C}_h \times \boldsymbol{T}|$ divided by the area of the graphene lattice $|\boldsymbol{a}_1 \times \boldsymbol{a}_2| = \sqrt{3}a/2$, and is $N = 2(n^2 + nm + m^2)/d_R$. Because there are two inequivalent carbon atoms in the graphene lattice, the number of carbon atoms in the carbon nanotube unit cell is $2N$. For the $(4, 2)$ carbon nanotube corresponding to $d_R = 2$, we have $N = 28$ and the number of carbon atoms is 56.

The electronic properties of the carbon nanotube are discussed in the reciprocal space which can be constructed from the reciprocal space of graphene as shown in Fig. 1-2. $\boldsymbol{b}_1$ and $\boldsymbol{b}_2$ are the reciprocal lattice unit vectors of graphene obtained from the definition $\boldsymbol{a}_i \cdot \boldsymbol{b}_j = 2\pi\delta_{ij}$, which are then expressed as $\boldsymbol{b}_1 = (\frac{2\pi}{\sqrt{3}}, 2\pi)\frac{1}{a}$ and $\boldsymbol{b}_2 = (\frac{2\pi}{\sqrt{3}}, -2\pi)\frac{1}{a}$ [16]. The reciprocal lattice unit vectors of carbon nanotube $\boldsymbol{K}_1$ and $\boldsymbol{K}_2$ are obtained by the definition : $\boldsymbol{C}_h \cdot \boldsymbol{K}_1 = \boldsymbol{T} \cdot \boldsymbol{K}_2 = 2\pi$ and $\boldsymbol{C}_h \cdot \boldsymbol{K}_2 = \boldsymbol{T} \cdot \boldsymbol{K}_1 = 0$. Then, $\boldsymbol{K}_1$ directs in circumferential direction with length $|\boldsymbol{K}_1| = 2/d_t$, and $\boldsymbol{K}_2$ directs in tube axis direction with length $|\boldsymbol{K}_2| = 2\pi/T$. By applying periodic boundary condition to the circumferential direction, N finite wave vectors along tube axis are obtained, where N is number of graphene lattices in the carbon nanotube unit cell. The index μ varying from $1 - N/2$ to $N/2$ are defined to denote these vectors as $\mu\boldsymbol{K}_1$. The wave vector along tube axis is continuous varying from $-\pi/T$ to π/T in the first

Fig. 1-2: fig:/fig:SWNT-reciprocal.eps

Brillouin zone. Therefore, the Brillouin zone of a SWNT is composed of N discrete lines of wave vectors along the circumferential direction, and each line is elongated continuously in the tube axis direction. These lines are called the cutting lines as shown in Fig. 1-2 for a (4,2) SWNT. The wave vectors in the Brillouin zone of a SWNT are then expressed as [16] :

$$\boldsymbol{k} = \mu\boldsymbol{K}_1 + k\frac{\boldsymbol{K}_2}{|\boldsymbol{K}_2|} \quad \text{with} \quad \mu = 1 - N/2, ..., N/2 \quad \text{and} - \frac{\pi}{T} \leq \frac{\pi}{T}. \tag{1.1}$$

N pairs of the electronic energy dispersion of carbon nanotube are cross-sections of the electronic energy dispersion of graphene, obtained by applying the zone-folding scheme [1]. The electronic energy dispersion along the cutting line μ of carbon nanotube is expressed as [16] :

$$E_\mu(k) = E_{g2D}\left(\mu\boldsymbol{K}_1 + k\frac{\boldsymbol{K}_2}{|\boldsymbol{K}_1|}\right), \quad \left(\mu = 0, ..., N-1 \text{and} - \frac{\pi}{T} < k < \frac{\pi}{T}\right), \tag{1.2}$$

where E_{g2D} is the electronic energy dispersion of graphene. The electronic dispersion of graphene can be calculated by the simple tight binding approximation (STB), which takes into account the interaction of a carbon atom with its nearest neighbor atoms. The valence band (π band), the conduction band (π^* band) of graphene, and the cross-sections obtained by applying the zone-folding scheme to the cutting lines of a (4,2) carbon nanotube are shown in Fig. 1-3(a) [2]. The electronic energy dispersion and the calculated electronic density of state (DOS) of (4,2) carbon nanotube obtained from the zone-folding scheme are shown in Fig. 1-3(b) and Fig. 1-3(c), respectively. If there is a cutting line of a particular nanotube (n, m) that passes through the K point where π and π^* bands are degenerate, then the carbon nanotube is metallic because the energy gap is zero. However, if a (n, m) carbon nanotube has no cutting line passing through the K point, the carbon nanotube becomes semiconductor because of finite band gap. Two types of semiconducting carbon nanotube, S1 and S2, are defined as $\text{mod}(2n+m, 3) = 1$ and $\text{mod}(2n+m, 3) = 2$, respectively, and the metallic carbon nanotube corresponds to $\text{mod}(2n+m, 3) = 0$ [1]. Therefore, the (4,2) carbon nanotube as shown in Fig. 1-3 is S1 semiconducting carbon nanotube. The sharp

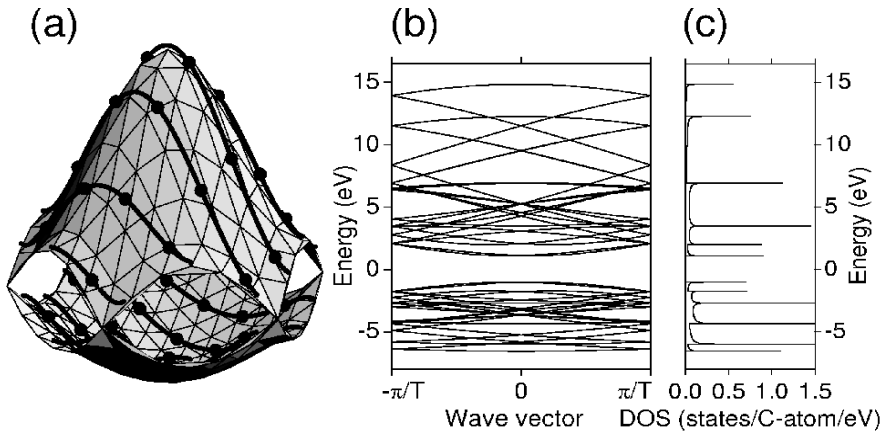

Figure 1-3: **The electronic energy dispersion and DOS of (4,2) carbon nanotube from zone-folding scheme [2].** (a) Valence band (π band) and conduction band (π^* band) of graphene in the Brillouin zone. The thick lines are the cutting lines of (4,2) carbon nanotube by applying zone-folding scheme, and the solid dots denote the end of the cutting lines. (b) The electronic energy dispersion of (4,2) carbon nanotube obtained by zone-folding scheme. (c) The electronic density of state (DOS) per energy per carbon atom of (4,2) carbon nanotube. The peak of DOS is known as van Hove Singularity (vHS).

peak of DOS is known as the van Hove singularity (vHS) [1]. The vHS occurs at the touching point of the cutting line with the equi-energy contour of π electron (energy difference between π and π^* bands) [3]. If the energy of laser light matches the energy difference between valence and conduction bands at the vHS, the electron can absorb light and transit from the valence band to the conduction band. If the laser light is polarized parallel to the tube axis, the electrons make the vertical transitions with the same cutting line index μ between two bands, which is simply called $E_{\mu\mu}$ transition. However, if the laser light is polarized perpendicular to the tube axis, the electrons in the valence band with the cutting line index μ transit to the adjacent cutting lines index $\mu \pm 1$ in the conduction band [3]. We specify the vertical transition of electron in the cutting line which is closet to K point (without passing through K point) as E_{11}, and higher energy vertical transitions in visible region are called E_{22} and E_{33}. The plot of the E_{ii} as a function of tube diameter d_t or the inverse of tube diameter is called the Kataura plot [7]. An accurate Kataura plot which reproduces

Fig. 1-3: fig:/fig:SWNT-dispersion.eps

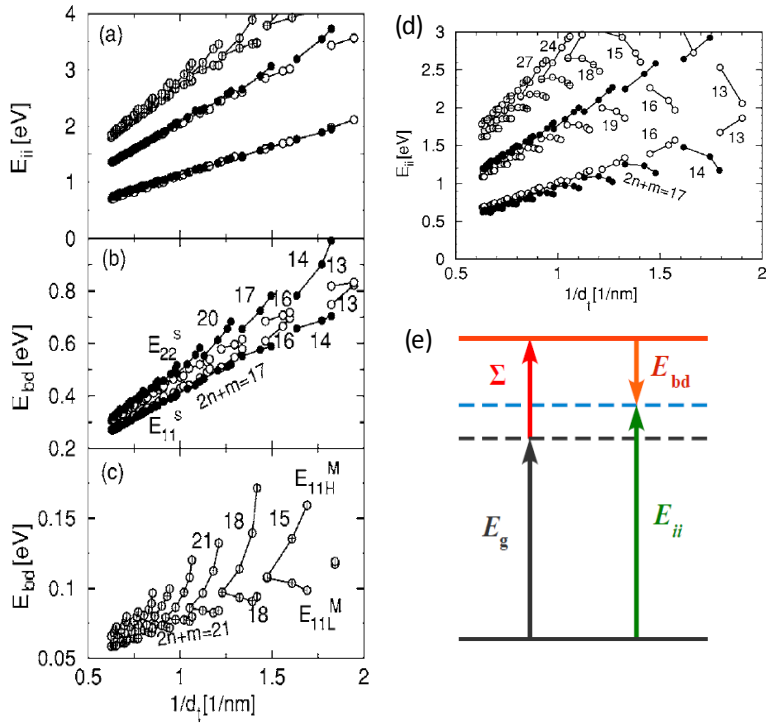

Figure 1-4: **Transition energy E_{ii} and binding energy E_{bd} Kataura plot.** (a) Exciton transition energy E_{ii} calculated from STB nethod as a function of inverse of diameter d_t. Open, filled and crossed circles are for S1, S2 and metallic SWNTs, respectively [7]. (b) Binding energy E_{bd} calculated from the STB method as a function of inverse of diameter d_t. Open and filled circles are S1 and S2 SWNTs, respectively [7]. (c) Binding energy E_{bd} of metallic SWNTs calculated from the STB method as a function of inverse of diameter d_t [7]. (d) Exciton transition energy E_{ii} calculated from the ETB method as a function of inverse of diameter d_t. Open, filled and crossed circles are for S1, S2 and metallic SWNTs, respectively [7]. (e) The correction of transition energy E_{ii} by the exciton theory. The energy gap E_g of single-particle model is added by positive self energy Σ, and then is subtracted by the binding energy E_{bd} [10].

the experiemtal result relies on the exciton theory which is briefly reviewed in the next section.

1.4.2 Concept and experimental facts of excitons in SWNTs

An exciton is the bound state of a photo-excited electron and a hole due to the Coulomb interaction. It can be formed at room temperature for carbon nanotube

Fig. 1-4: fig:/fig:exciton-Eii-Jiang.eps

because of the large binding energy, which can be as large as 1 eV [1, 7]. The exciton is a many-body system in which many wave vectors on the cutting lines are mixed. The exciton theory in carbon nanotubes has been proposed to explain the ratio problem in which the ratio E_{22}/E_{11} of semiconducting SWNTs are not equal to two as predicted by STB model, but it is always less than two from experiment [9]. Another reason is because of the weak dependence of the transition energy E_{ii} on the chiral angle calculated from the STB method [9], which is not consistent with the experimental observation of the Kataura plot showing the large $(2n+m)$-family spread [11]. From the exciton theory, the transition energy E_{ii} is corrected by the electron-electron and electron-hole interactions giving rise to the positive self-energy Σ and the binding energy E_{bd}, respectively, as shown in Fig. 1-4(e) [10]. However, it has been shown by J. Jiang et al., that the excitonic transition energy E_{ii} calculated by the STB method also shows weak spread of E_{ii} on the chiral angle as shown in Fig. 1-4(a) [7]. This problem has been solved by using the extended tight binding method (ETB) in which the mixing of π orbitals with σ orbitals, and the optimization of bond length or the tube structure, are taken into account [1]. The transition energy E_{ii} calculated from ETB method by J. Jiang et al., as shown in Fig. 1-4(d), shows a large $(2n+m)$-family spread which is consistent with experiment [11]. The binding energy E_{bd} of semiconducting and metallic SWNTs are shown in Fig. 1-4(c) and Fig. 1-4(d), respectively, showing the dependence of E_{bd} on diameter and chiral angles of SWNTs.

The elegant experiment confirming the excitonic effect in the optical transitions of SWNTs is the two-photon photoluminescence (PL) experiment by J. Maultzsch et al. [12]. The schematic processes of one-photon PL in the one-particle picture and the exciton picture are shown in Fig. 1-5(a). In the one-particle picture, the electron is excited to make an E_{22} transition to the conduction band. The photo-excited electron then relaxes, and then makes E_{11} emission to the valence band. In the exciton-picture, the one-photon energy gets absorbed by the $1u$ exciton of a E_{22} transition. After that, the $1u$ exciton of the E_{22} transition relaxes to the $1u$ state of

Fig. 1-5: fig:/fig:exciton-2photon.eps

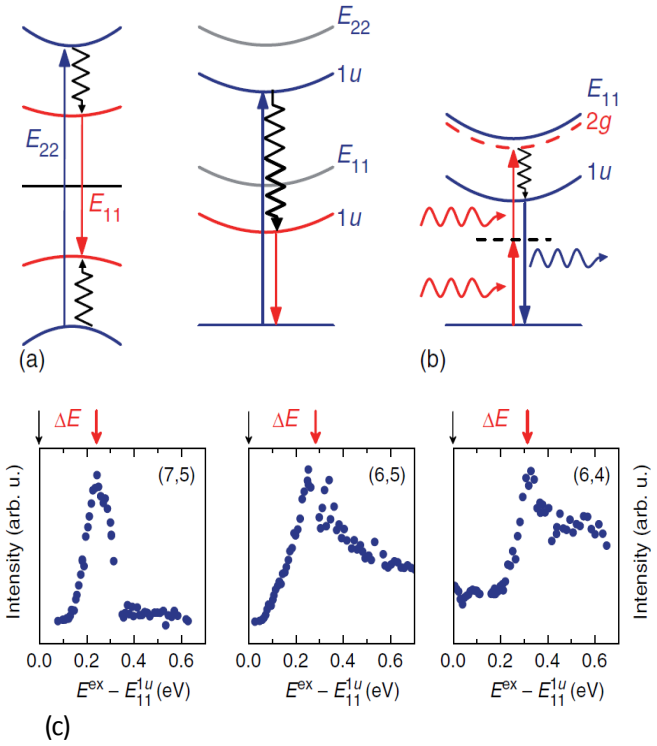

Figure 1-5: **Two-photon photoluminescence (PL) experiment of SWNTs, after [12]** (a) Left picture shows one-photon PL process schematically in one-particle picture. Right picture shows the one-photon PL process schematically in exciton picture in which the $1u$ exciton of optically allowed. (b) Schematic process of two-photon PL experiment in which $2g$ exciton becomes optically allowed. $2g$ exciton is not optically allowed in one-photon PL experiment. (c) Luminescence intensity as a function of two-photon excitation energy of (7,5), (6,5) and (6,4) SWNTs. The black arrows indicate the one-photon emission energy of $1u$ exciton E_{11}^{1u}, the red arrows indicate two-photon absorption maximum identified as E_{11}^{1g}.

an E_{11} transition and then make the E_{11} one-photon emission by recombining process between the photo-excited electron and the hole. However, in the two-photon PL experiment as shown in Fig. 1-5(b), the $2g$ exciton of the E_{11} transition, which is not optically allowed (dark) in one-photon PL, is excited. Then, the $2g$ exciton relaxes to the $1u$ exciton of the same energy transition to make E_{11} one-photon emission by recombining process. The energy difference between the $2g$ and $1u$ excitonic states indicates the strength of the Coulomb interactions. If there were no Coulomb interactions due to the excitonic effect, the two-photon and one-photon allowed states would have approximately the same energy [12]. However, by plotting the emission

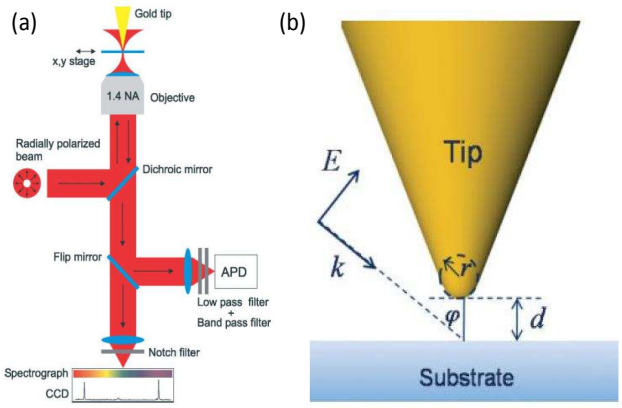

Figure 1-6: **The schematic experimental setting up of TERS experiment** (a) On-axis illumination of the metallic tip using radially polarized laser beam passing through the transparent sample. This near field experiment can't be done with a nontransparent sample [15]. (b) Side illumination of the metallic tip using the linearly polarized laser light. This configuration can be utilized with the sample on the nontransparent substrate [18].

intensity as a function of $E^{ex} - E_{11}^{1u}$ where E^{ex} is an excitation energy as shown in Fig. 1-5(c), the intensity peak of each chiralrity has been observed in range 240 - 325 meV, which is identified as the two-photon allowed E_{11}^{2g} state. The exciton binding energy $E_{bd} = E_{11}^{2g} - E_{11}^{1u}$ is then determined at this maximum point, which is consistent with the first principle calculation [12].

1.4.3 Tip-Enhanced Raman Spectroscopy (TERS)

In TERS experiment, a sharp metallic tip with a cone shape is put at a small distance above the sample. TERS experiments can be categorized into two types based on the transparency property of the sample [20] as : (i) on-axis illumination shown in Fig. 1-6(a) and (ii) side illumination shown in 1-6(b). Here, the TERS experiment in the on-side illumination scheme utilized by L. G. Cancado et al. [15] is reviewed firstly. According to the schematic experimental setting up in Fig. 1-6(a), the gold tip ended with a sphere of about 20 nm diameter produced by the electrochemical etching scans the sample on the x,y stage. The separation distance between the tip

Fig. 1-6: fig:/TERS-setup.eps
Fig. 1-7: fig:/TERS-result-Cancado.eps

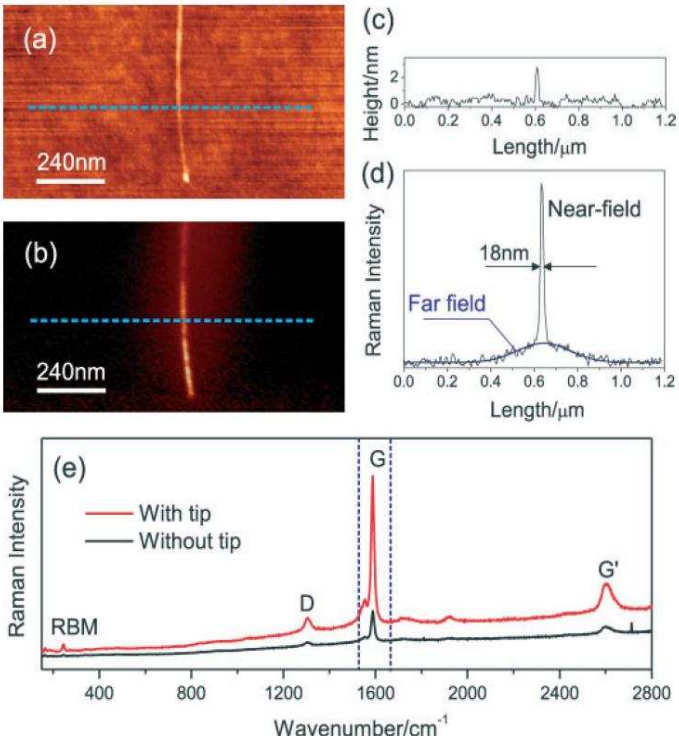

Figure 1-7: **experimental results from TERS in on-axis illumination scheme [15]** (a) Topographic image of the carbon nanotube bundle on glass. (b) TERS image of carbon nanotube bundle on glass. (c) Height profile of the carbon nanotube bundle taken along the dashed blue line of the topographic image. (d) Raman intensity profile of the carbon nanotube bundle measured along the dashed blue line of the TERS image. (e) The Raman intensities as a function of Raman shift measured by with and without the gold tip are indicated by the red and black spectra, respectively. The integration region of the G band Raman intensities is indicated by the vertical dashed lines.

apex and the sample is controlled by a quartz tunning fork attached to the tip. The radially polarized laser beam or a linearly polarized beam is focused onto the sample using a high numerical aperture objective (1.4NA), and the gold tip is positioned in the focused beam. The optical signal is then collected by the same objective and detected either using a single-photon counting avalanche photodiode (APD), or by the combination of a spectrograph and a cooled charge-coupled device (CCD) [15]. In both cases, the tip-enhanced Raman image is obtained simultaneously with the topographic image by raster-scanning the sample [15]. By using a linearly polarized laser with wavelength 632.8 nm and positioning the gold tip about 2 nm above a

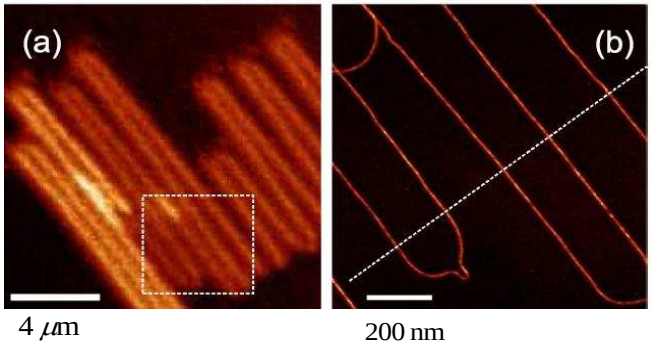

Figure 1-8: **Conventional and tip-enhanced Raman images of a self-organized semiconducting carbon nanotube serpentine done by L. G. Cancado et al. [14]** (a) Conventional Raman image acquired from the G band intensity. (b) Tip-enhanced Raman image acquired from the G band intensity by raster scanning the gold tip at distance 2 nm above the carbon nanotube within the square area enclosed by dashed square in the conventional Raman image. (c) Raman intensity profile taken along the dashed line in the tip-enhanced Raman image.

carbon nanotube bundle on glass, the topographic image and the tip-enhanced Raman image are acquired simultaneously by line scanning of the gold tip, as shown in Fig 1-7(a) and Fig 1-7(b), respectively. The height profile of the carbon nanotube bundle taken along the dashed blue line in the topographic image is shown in Fig 1-7(c). From the height profile of the topographic image, the diameter of the carbon nanotube bundle can be estimated to be about 2.5 nm. The Raman intensity profile measured along the dashed blue line of the TERS image is shown in Fig 1-7(d). From the Raman intensity profile, the spatial resolution of the near field is obtained to be about 18 nm, and the resolution of the far field fitted with Gaussian function is about 290 nm. The resolution of the TERS image is close to the diameter of the tip. Finally, the measured Raman intensities as a function of Raman shift with tip indicated by the red spectrum and without tip indicated by the black spectrum are shown in Fig 1-7(e). The near field enhancement of the Raman intensity can be seen from this figure, and the enhancement factor will be given in the next section. From the energy of RBM mode $\omega_{\mathrm{RBM}} = 245$ cm^{-1}, the chirality of the SWNT is specified as (10,3) semiconducting SWNT, whose E_{22} transition resonances with the energy of laser light.

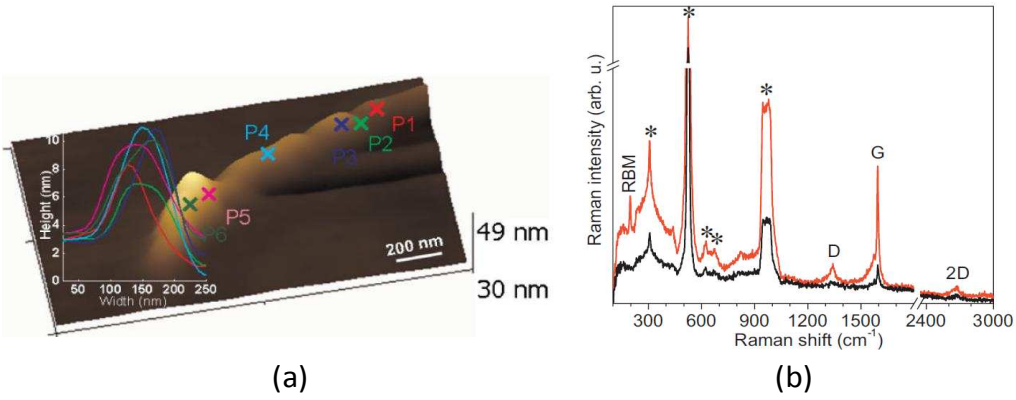

Figure 1-9: **Tip-enhanced Raman intensity of a carbon nanotube bundle produced by HipCO method done by N. Peica et al. [17]** (a) AFM topographic image of a carbon nanotube bundle with the height profiles at six different positions. (b)Tip-enhanced Raman intensity as a function of Raman shift indicated by the red spectrum and the conventional Raman intensity as a function of Raman shift indicated by the black spectrum. The stars denote peak of the substrate. The Raman intensities are taken at the position P4.

The same TERS experiment have been done for a self-organized semiconducting carbon nanotube serpentine by L. G. Cancado et al. [14]. The conventional and tip-enhanced Raman images acquired from the G band intensity are shown in Fig. 1-8(a) and Fig. 1-8(b), respectively. It can be seen that the tip-enhanced Raman image has much higher resolution than the conventional Raman image which has a low resolution. The spatial resolution of the tip-enhanced Raman image can be estimated as about 25 nm from the Raman intensity profile taken along the dashed line in the tip-enhanced Raman image as shown in Fig. 1-8(c).

Lastly, the TERS experiment in the side illumination scheme as shown in Fig 1-6(b) done by N. Peica et al., is reviewed. A carbon nanotube bundle is prepared by high-pressure gas-phase decomposition of CO (HipCO), and it is deposited on a Si/SiO_2 substrate. The laser light with wavelength 532.2 nm is linearly polarized along the tip axis incident on the gold tip produced by depositing gold on the triangular silicon nitride tip. The AFM topographic image of the carbon nanotube bundle with the height profiles at six different positions is shown in Fig. 1-9(a). The conventional

Fig. 1-8: fig:/TERS-result-Cancado2.eps
Fig. 1-9: fig:/TERS-result-Peica.eps

and tip-enhanced Raman intensities as a function of Raman shift indicated by the black spectrum and red spectrum, respectively, acquired at the position P4 are shown in Fig. 1-9(b). The near field enhancement of the Raman signal can be seen from the Raman spectra. The enhancement factors are 3.4×10^3, 3.7×10^3, and 4.8×10^3, for the 2D, D , and G modes.

1.4.4 Effective enhancement factor

Enhancement factor of Raman signals measured by TERS is calculated using different definition by different research groups. Therefore, there is difficulty to compare the reported enhancement factors [23]. For SWNTs, the effective enhancement factor (γ) is introduced to describe the enhancement of Raman intensities obtained from TERS experiment [15, 22, 24]. In addition to measured Raman signals, the areas probed by near field and far field are taken into account in γ because near field strongly interacts with SWNTs only within small extent, but it weakly interacts with SWNTS outside this region.

There are two approaches used to calculate the relative intensities or contrast [23] in TERS. In the first approach, the contrast is obtained by the ratio between integrated Raman intensities of a particular band measured with tip and without tip, $I_{\text{with tip}}$ and $I_{\text{without tip}}$, respectively. The Raman intensities in this case are mixing of near field and far field components. This approach has been utilized by L. G. Cancado et al., to compare the experimental normalized Raman intensities measured by TERS as a function of separation distance between tip apex and SWNTS [14] with theoretical model. Another approach treats far field signal $I_{\text{without tip}}$ as the background, and then near field signal I_{nf} is obtained by the difference between $I_{\text{with tip}}$ and $I_{\text{without tip}}$. The contrast in this approach is calculated by the ratio of I_{nf} and $I_{\text{without tip}}$. This approach has been used by A. Hartschuh et al. [22]. The contrast obtained by two approaches are expressed as follows [23] :

$$\text{approach 1 :} \quad \text{contrast} \quad = \quad \frac{I_{\text{with tip}}}{I_{\text{without tip}}} \tag{1.3}$$

$$\text{approach 2}: \quad \text{contrast} \quad = \quad \frac{I_{\text{nf}}}{I_{\text{without tip}}} = \frac{I_{\text{with tip}} - I_{\text{without tip}}}{I_{\text{without tip}}}. \tag{1.4}$$

When we consider the areas, we will call the area probed by near field and far field as near field area (A_{nf}) and far field area (A_{nf}), respectively. Then, γ is defined as the ratio between the contrast normalized by the ratio between near field and far field areas ($A_{\text{nf}}/A_{\text{ff}}$), expressed as [23]

$$\gamma = \frac{\text{contrast}}{A_{\text{nf}}/A_{\text{ff}}}, \tag{1.5}$$

where contrast is in Eqs. (1.3) or (1.4). The near field area (A_{nf}) is estimated by the product of full width at half maximum (FWHM) of near field and circumference of SWNTs, and the far field area (A_{ff}) is calculated by the product of diameter of focus of laser light (f) and circumference of SWNTs [22].

For example, $I_{\text{with tip}}$ and $I_{\text{without tip}}$ of G band in Fig. 1-7(e) obtained by integrating intensities within the spectral window indicated by dashed vertical lines are 5.9×10^5 and 1.2×10^5 count/cm (approach 1), respectively [15]. $(A_{\text{ff}}) = 725\pi$ nm^2 is calculated by diameter of nanotube bundle 2.5 nm and $f = 290$ nm. The FWHM of near field is about 18 nm, then $A_{\text{nf}} = 45\pi$ nm^2. Therefore, the effective enhancement factor γ og G band is about 79.

1.4.5 Tip-sample distance dependence of the relative Raman intensity

The localization of the near field Raman intensity in the vertical direction can be demonstrated by the relative Raman intensity as a function of the tip-sample distance. A Hartschuh *et al.* [13] have shown that the ratio between the Raman intensity of the G′ band measured with the tip at the distance Δz above a SWNT, $I(\Delta z)$, and the far field Raman intensity of the G′ band measured without the tip decays exponentially with the decay length, the distance at which the Raman intensity decreases by $1/e$, about 11 nm as shown in Fig. 1-10(a). The decay length is close to the tip radius. It

Fig. 1-10: fig:/relInten.eps

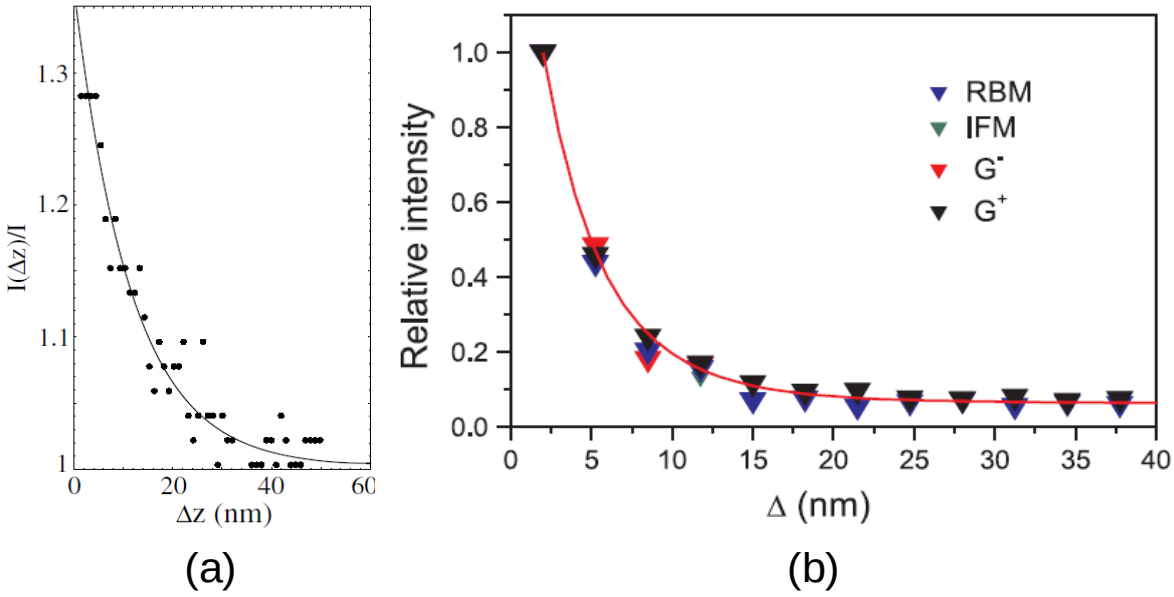

Figure 1-10: **Relative Raman intensity as a function of tip-SWNT distance** (a) The solid points are the experimental ratio between the Raman intensity of the G′ band measured with the tip positioned at the distance Δz above a SWNT, $I(\Delta z)$, and the far field Raman intensity of the G′ band measured without the tip, I,as a function of the distance Δz [13]. The solid line is the exponential fitting function with the decay length 11 nm. The tip is made from silver with the tip radius about 10-15 nm. The He-Ne laser light with the wavelength 633 nm excites the SWNT and the silver tip simultaneously in the on-axis illumination scheme as shown in the Fig. 1-6(a). The SWNT is produced by the CVD method deposited on the SiO_2 substrate. (b) The solid points are the experimental ratio between the $I(\Delta)$ and Raman intensity measured with the tip positioned at the distance about 2 nm above the SWNT, $I_{\max}$, as a function of the distance Δ [14]. The solid line is the fitting function in Eq. (1.6). The tip is made from gold with the tip radius about 15 nm. The He-Ne laser light with the wavelength 633 nm is used to excite the SWNT and the gold tip simultaneously in the on-axis illumination scheme. The SWNT is a self-organized carbon nanotube serpentine as shown in Fig. 1-8.

should be noted that $I(\Delta z)$ is the mixing of the near field Raman intensity and the far field Raman intensity, $I(\Delta z) = I_{\text{nf}}(\Delta z) + I_{\text{ff}}$. The exponential fitting function in the Fig. 1-10(a) can be obtained by using the values of $I(\Delta z)$ at the large distance ($\Delta z > 60$ nm), and at the closet distance ($\Delta z \approx 1$ nm). In 2009, L. G. Cancado *et al.* [14] has performed similar TERS experiment using the gold tip with the tip radius ρ_{tip} about 15 nm. The sample is the self-organized carbon nanotube serpentine as

shown in Fig. 1-8. They have shown that the experimental ratios between the Raman intensities of the RBM, IFM, G^- and G^+ measured with the gold tip at the distance Δ above the SWNT and those measured with the gold tip at the distance 2 nm above the SWNT, $I_{\max}$, are inversely proportional to the 10th power of $\Delta + \rho_{\text{tip}}$ as expressed in Eq. (1.6).

$$\frac{I(\Delta)}{I_{\max}} = \frac{1}{M} + \frac{C}{(\Delta + \rho_{\text{tip}})^{10}}, \tag{1.6}$$

where $M = 16$, $C = 4.5 \times 10^{15}$ nm^{10} and $\rho_{\text{tip}} = 35$ nm are obtained by fitting with the experimental data as shown in Fig. 1-10(b). It can be seen that the tip radius in the fitting function is about two times larger than the exact tip radius obtained by the scanning electron microscopy (SEM) measurement because of the limitation of the point dipole model that they have employed [14]. Moreover, they have found the similar behavior as Fig. 1-10(b) for the SWNTs of other chiralities with the same tip. Therefore, the maximum enhancement M is affected only by the tip properties but not by the tube structure [14]. In addition to the fitting function in Eq. (1.6), we may write the fitting function for the ratio between $I(\Delta)$ and the far field Raman intensity I_{ff} by considering Eq. (1.6) at the large distance where the Raman intensity has only the far field component. Then, from Eq. (1.6), we can have the relation $(M-1)I_{\text{ff}} = I_{\text{nf}}^{\text{amx}}$, where $I_{\text{nf}}^{\max}$ is the near field Raman intensity at the closet distance. By substituting $I_{\text{nf}}^{\max}$ in terms of I_{ff} into Eq. (1.6), the fitting function of $I(\Delta)/I_{\text{ff}}$ can be expressed as

$$\frac{I(\Delta)}{I_{\text{ff}}} = 1 + M\frac{C}{(\Delta + \rho_{\text{tip}})^{10}}. \tag{1.7}$$

We can also obtain the fitting function of $I_{\text{nf}}(\Delta)/I_{\text{ff}}$ by substituting $I(\Delta) = I_{\text{nf}}(\Delta) + I_{\text{ff}}$ into Eq. (1.7). Then, the relative Raman intensity of the near field and the far field as a function of the tip-SWNT distance can be expressed as

$$\frac{I_{\text{nf}}(\Delta)}{I_{\text{ff}}} = M\frac{C}{(\Delta + \rho_{\text{tip}})^{10}}. \tag{1.8}$$

Eq. (1.8) shows that the enhancement of the near field Raman intensity is inversely proportional to the 10th power of summation between the separation distance and

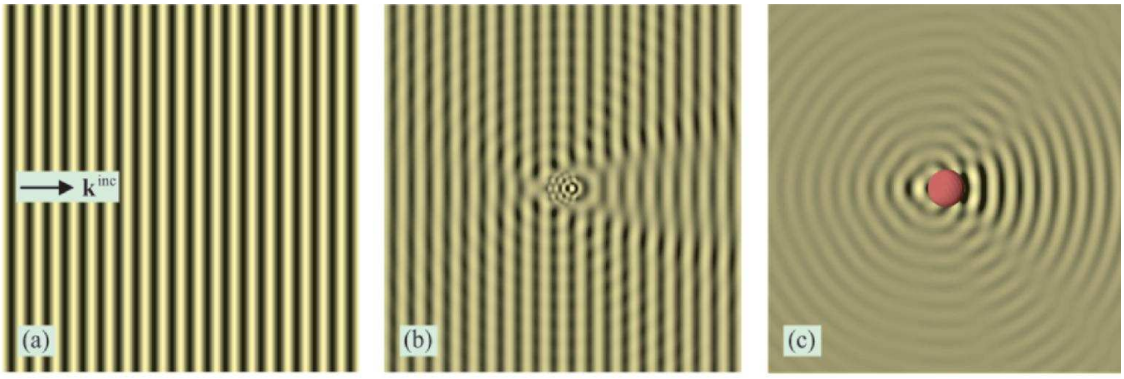

Figure 1-11: **The illustration of the scattering of light by a spherical particle [26]** (a) Real part of the incident electric field traveling from the left side to the right side in nonabsorbing dielectric medium. (b) Real part of total electric field which is the summation of the incident electric field and the scattered electric field radiated from the spherical particle with real refractive index n=2.8 at the center of the figure. (c) Real part of the scattered electric field radiated by the spherical particle at the center of the figure.
Note : Color scale of each figure is different.

the tip radius. It also implies that the near field Raman intensity at the distance Δ dramatically increases by decreasing the tip radius. Eq. (1.8) will be used to compare with the tip-SWNT distance dependence of the relative Raman intensity obtained from this thesis in chapter 4.

1.4.6 Scattering of light by metallic sphere

Because metallic tip employed in TERS experiment is ended with the finite volume sphere and the near field is localized near the tip apex, the near field may be obtained by considering the scattering of laser light by the metallic sphere with the same radius as the tip apex. Then, the solutions of Maxwell's equations can be solved analytically in the spherical coordinate given firstly by Gustav Mie in 1908 [25] by means of the separation of variables method used for solving the vector Helmholtz equations. Mie's theory was later modified in terms of so called vector spherical wave function (VSWFs) by J. A. Stratton in 1941 [27, 28]. Both cases treat the incident light as a linearly polarized plane wave. If the laser light is in another form (e.g., a focused Gaussian

Fig. 1-11: fig:/Mie.eps

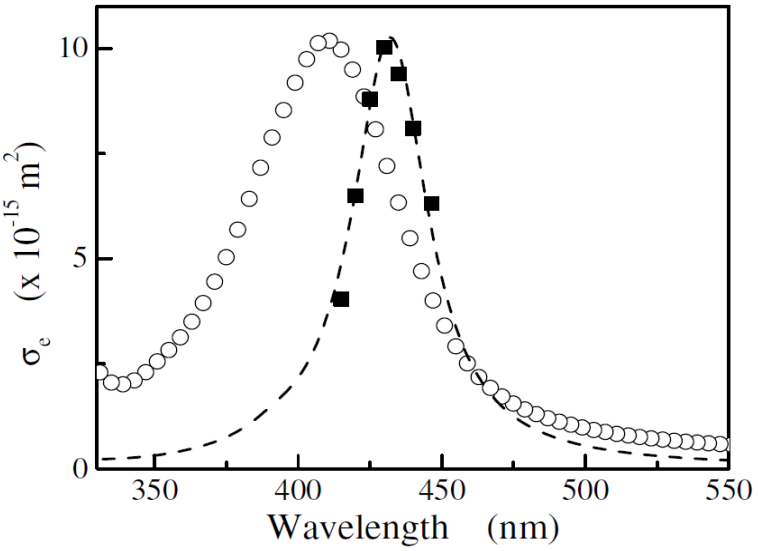

Figure 1-12: **Absorption spectra of single silver sphere [31]** The extinction cross-section σ_e is approximately the same as the absorption cross-section σ_a, $\sigma_e \approx \sigma_a$. The silver sphere has diameter 31 nm deposited on glass. The open circle is the absorption spectrum of the silver sphere on glass substrate without PVOH, the solid square is the absorption spectrum of the silver sphere on glass substrate with PVOH, and the dashed line is the absorption spectrum calculated from Mie theory.

beam), the solutions are called the generalized Mie's theory [29]. In this thesis, we will use the linearly polarized plane wave as the incident light, and the separation of variables method which is straightforward and simpler than VSWFs will be used. The solutions of Mie's theory are general for any kind of dielectric material with the spherical shape. The concept of the scattering of light by a dielectric spherical particle is illustrated in Fig. 1-11. The amplitude of the real part of the incident light traveling in the nonabsorbing dielectric medium is illustrated in Fig 1-11(a). When the finite volume of the spherical particle is put at the center of Fig 1-11(a), it will be excited by the plane wave to radiate the scattered wave propagating out from the particle. The amplitude of the total electric field in the scattering process is shown in Fig 1-11(b). It can be seen that the total electric field near the particle is spherical wave due to the superposition of the incident light and the spherically scattered wave. In Fig 1-11(c), the spherically scattered electric field is shown without the incident electric field.

Experimentally, the absorption spectra is measured in far-field region. The absorption spectra calculated from so called quasi-static approximation gives good agreement with the experiment of a single gold nanoparticle with diameter 17.6 nm, which is small compared to the wavelength of incident light in visible region [30]. Mie's theory also reproduces experimental absorption spectra of small metallic nanoparticle and larger diameter but finite volume of metallic nanoparticle as shown in Fig 1-12 for single silver nanoparticle with diameter 31 nm [31]. In Fig. 1-12, the extinction cross-section σ_{e} spectrum which is approximately the same as the absorption cross-section σ_{a} spectrum for silver sphere with radius 31 nm deposited on glass substrate embedded in polyvinyl alcohol (PVOH) is shown by solid squares. The dash line is the extinction cross-section calculated from Mie's theory. The open circles are the extinction cross-section of silver sphere on glass substrate without PVOH. The peak position in the absorption spectrum is known as surface plasmon resonance (SPR). The surface plasmon is understood as the collective oscillation of free electrons in metal especially in noble metals (e.g., gold and silver). It can be seen that by changing the dielectric constant, the absorption peak is shifted and the broadening is changed. In this case, the absorption peak of the open circle spectrum is red shifted to the solid square spectrum by increasing dielectric constant of the environment around the single silver sphere. The full width at half maximum (FWHM) of the open circle spectrum is about 65 nm, and the FWHM of the solid square spectrum get sharper about 30 nm. This experiment implies that the near field enhancement and width generated by a metallic sphere are sensitive to the dielectric constant of the medium. The dielectric constants of noble metals are reviewed in next sections.

1.4.7 Optical properties of noble metals

The simplest model describing the response of electrons in solid metals classically is the Drude model or the free electron model. This model treats electrons in solid metal as free electrons gas moving with respect to positively ionic cores. The free electrons scatter with each other after exciting by the external light. This model

Fig. 1-12: fig:/Mie-absorption-spectra.eps

is well suited to describe the optical response of a silver and a gold with external light in visible region. However, when the energy of the external light is increased, the electrons make the interband transition from the valence band to the conduction band at definite wavelength depending on the band structure of each metal. The classical model that can describe the interband transition is the so called Lorentz model. The behavior of electrons in a metal solid is therefore mainly contributed by the free electrons model and the interband transition. The experimental data of the bulk dielectric constant of noble metals is well fitted with the sum of this two contributions.

Drude model

The Drude model assumes that the free electrons have finite value of the average relaxation time τ after the scattering with each other. The equation of this model is written as

$$\frac{\mathrm{d}\boldsymbol{p}(t)}{\mathrm{d}t} + \frac{\boldsymbol{p}(t)}{\tau} = \boldsymbol{f}(t), \tag{1.9}$$

where $\vec{p}(t)$ is the average momentum and $\vec{f}(t)$ is a driving force which can be either static or time-varying. The typical value of the average relaxation time τ of electron can be estimated from the DC resistivity ρ_0 by using the relation $\tau = \frac{m}{ne^2\rho_0}$, where m is electron mass, n is conduction electron density and e is electronic charge [33]. This formula is obtained by giving the driven force $\vec{f}$ in Eq. (1.9) as the static electric field. At T = 373 K the approximated relaxation time τ of Ag and Au are $\tau_{Ag} = 2.8\times10^{-14}$s and $\tau_{Au} = 2.1\times10^{-14}$s, respectively [33]. Now, let's us derive the dielectric constant ε from the Drude model when time-harmonic external light $\boldsymbol{E}_0 e^{-i\omega t}$ is incident on the surface of metal. The electric field inside the metal $\boldsymbol{E}$ is then oscillating with time with the same frequency as the external light, that is, $\boldsymbol{E}(t) = \boldsymbol{E}e^{-i\omega t}$. The driving force $\boldsymbol{f}(t)$ acting upon the electron become $\boldsymbol{f}(t) = -e\boldsymbol{E}e^{-i\omega t}$. Then, Eq. (1.9) becomes

$$m\frac{\mathrm{d}^2\boldsymbol{r}(t)}{\mathrm{d}t^2} + \frac{m}{\tau}\frac{\mathrm{d}\boldsymbol{r}}{\mathrm{d}t} = -e\boldsymbol{E}_0 e^{-i\omega t}, \tag{1.10}$$

where $\boldsymbol{r}(t)$ is the average electronic displacement. Eq. (1.10) can be solved by assuming that the average electronic displacement has the same time-harmonic response as the driving force, that is, $\boldsymbol{r}(t) = \boldsymbol{r}_0 e^{-i\omega t}$. By substituting this assumed time-harmonic average displacement into Eq. (1.10), the amplitude $\boldsymbol{r}_0$ can be found. The displacement of the electron relative to the positive background gives rise to the electronic polarization $\boldsymbol{P}(t)$ defined as number of electric dipole moments $\boldsymbol{\mu}$ per unit volume, that is, $\boldsymbol{P}(t) = n\boldsymbol{\mu}(t) = -ne\boldsymbol{r}_0 e^{-i\omega t}$, where n is electronic density. Then, the electronic polarization can be written in term of the electric field inside the metal $\boldsymbol{E}_0$ as :

$$\boldsymbol{P} = -\frac{(ne^2/m)\boldsymbol{E}_0}{\omega^2 + i\omega/\tau}. \tag{1.11}$$

The polarization of the positive background $\boldsymbol{P}_b$ which is non-resonant may be included in the constitutive relation $\boldsymbol{D} = \varepsilon_0\varepsilon\boldsymbol{E} = \varepsilon_0\boldsymbol{E} + \boldsymbol{P} + \boldsymbol{P}_b$, where $\boldsymbol{E}$ is the local electric field inside the metal. Then, the electronic polarization $\boldsymbol{P}$ is written in term of the local electric field $\boldsymbol{E}$ as $\boldsymbol{P} = \varepsilon_0(\varepsilon - \varepsilon_\infty)\boldsymbol{E}$, where ε_∞ is defined as the dielectric constant of the positive background. By making some algebra, the dielectric constant ε is written as :

$$\tilde{\varepsilon} = \varepsilon_\infty - \frac{\omega_p^2}{\omega^2 + i\omega\Gamma}, \tag{1.12}$$

where the tilde denotes that the dielectric constant is a complex number. Hereafter, the tilde will always be used to denote the complex number. The real part and the imaginary part of $\tilde{\varepsilon}$ as a function of frequency is explicitly written in following equation.

$$\varepsilon_1 = \varepsilon_\infty - \frac{\omega_p^2}{\omega^2 + \Gamma^2} \quad , \quad \varepsilon_2 = \frac{\omega_p^2\Gamma}{\omega(\omega^2 + \Gamma^2)}, \tag{1.13}$$

where $\omega_p = \sqrt{\frac{ne^2}{\varepsilon_0 m}}$ is so called the plasma frequency which corresponds to the oscillation frequency of the free electrons in vacuum and $\Gamma = 1/\tau$ is called the damping constant representing the scattering rate of the free electrons. The plasma frequencies and the damping constants of Ag and Au are shown in table 1.1. It can be seen that the plasma frequencies of gold and silver are very close to each other because number of conduction electrons per unit volume of gold and silver are nearly the same about

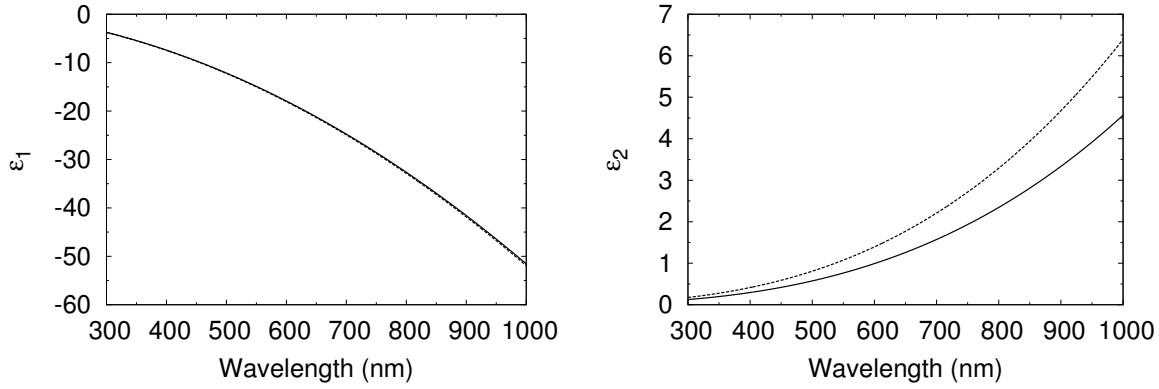

Figure 1-13: **Dielectric constant of Ag and Au from Drude model represented by solid and dashed lines, respectively :** (a) Real part of dielectric constant of Ag and Au using parameters from table 1.1 (b) Imaginary part of dielectric constant of Ag and Au using parameters from table 1.1.

$5.86 \times 10^{28}\,\mathrm{m}^{-3}$ and $5.90 \times 10^{28}\,\mathrm{m}^{-3}$, respectively [33]. The plasma frequencies ω_p of these two metals are in ultraviolet region. The damping constants of both two metals is small compared to the plasma frequency. Using parameters in table 1.1, ε_1 and ε_2

Table 1.1: The approximated relaxation time calculated from the DC resistivity at T = 373 K [33], the plasma frequencies and damping constants of Ag and Au

metal	$\tau(s)$	$\omega_p(eV)$	$\Gamma(eV)$
Ag	2.8×10^{-14}	8.99	0.148
Au	2.1×10^{-14}	9.02	0.197

of Ag and Au from the Drude model calculated by Eq. (1.13) are shown in Fig 1-13. Here we plot the dielectric constants as a function of wavelength which is useful in spectroscopy. The range of the wavelength covers the visible region and extends to lover energy in near infared region and extends to higher energy in near ultraviolet region.

The ε_1 of Ag and Au is negative in visible and infrared regions and negatively decreasing as increasing the wavelength because the energy is more less than the plasma frequency ω_p. If the energy becomes larger than the plasma frequency ω_p as

Fig. 1-13: fig:/eps1Drude.eps

given in table 1.1, the ε_1 becomes positive, and it is zero when the energy of laser light is the same as the plasma frequency. If the energy of laser light is large compared to the plasma frequency ω_p, the ε_1 becomes ε_∞ which corresponds to the dielectric constant of the background. It should be noted that the ε_1 of Ag is nearly the same as Au in infrared region including higher energy regions, and it is also the case for low energy region of wavelength in micron scale. The sign of ε_2 is opposite to the sign of ε_1 ,and it always be positive in the whole spectrum because there is no the negative term in the expression of ε_2. The ε_2 vanishes in the energy region much greater than the plasma frequency ω_p. The absolute value of ε_2 is small compared to the absolute value of ε_1 because the value of ε_2 can be approximately determined by $\varepsilon_2 \approx (\frac{\omega_p^2}{\omega^2})(\frac{\Gamma}{\omega})$ when the damping constant is neglected. If we consider in the visible region in which the energy is less than the plasma frequency, the multiplication of two parentheses of the approximated ε_2 becomes very small compared to the amplitude of ε_1 which can also be approximated as $\varepsilon_1 \approx (\frac{\omega_p^2}{\omega^2}) - 1$ with neglecting the damping constant. These behaviors of the dielectric play a role in the resonance of surface plasmon in metals. However, the Drude model is the classical model describing the free electrons in solid. When the energy of the incident light is increased and the electrons are strongly excited, we expect that the quantum effect contributes to the dielectric constant by the electronic transition of the free electrons from valence band to conduction band so called the interband transition. The interband transition can also be understood by simple model namely Lorentz model described in next the section.

Interband transition and Lorentz model

Electrons in noble metals can make the interband transition from filled valence band (d-band) to empty conduction band (s-band) if the excitation energy of the laser light matches with the energy gap. Therefore, the contribution of interband transition to the dielectric constant depends on the band structure of each metal. The transition edges of Ag calculated from the relativistic augment plane wave method are at 3.98 eV (311.6 nm) and 3.45 eV (359.4 nm) [34] which means that the interband transition does not contribute to the dielectric constant of Ag in visible and lower energy regions.

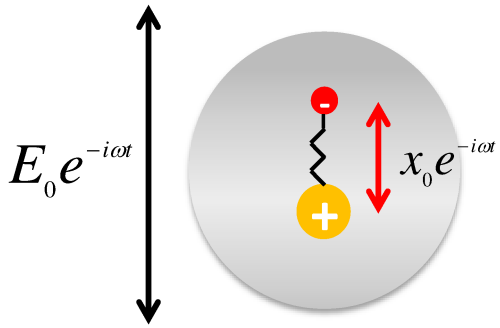

Figure 1-14: The geometry of the Lorentz model. The electron is connected to the nucleus by the spring forming the Lorentz oscillator. The oscillator starts vibration when there is the time-harmonic driving force due to the electric field $E_0 e^{-i\omega t}$ applied to the atom.

However, the absorption edges of Au are at wavelength about 470 nm and 330 nm [38]. Therefore, the effect of the interband transition can not be neglected in visible region for Au.

The Lorentz model is a simple model that can describe the interband transition effect. This model considers that the electron is connected with the nucleus by the spring with the force constant $k = m_e\omega_0^2$ forming the dipole oscillator or the Lorentz oscillator. The dipole oscillates at natural frequency ω_0 and can be damped because the electron has finite life time through the collisional processes. When the laser light with frequency ω hit the atom, the electron is displaced from its equilibrium position by the driving force $-eE(t)$ while the nucleus is considered to be fixed relative to the electron because its mass is much higher than the mass of the electron. The electron then feels the restoring force according to Hook's law $-m_e\Gamma\frac{\mathrm{d}x}{\mathrm{d}t}$ and damping force $-m_e\omega_0^2 x$, and it starts to vibrate at the same frequency as the external light wave. The geometry of the Lorentz model is shown in Fig. 1-14. The equation of motion for the electronic displacement x is expresses as :

$$m_e\frac{\mathrm{d}^2x}{\mathrm{d}t^2} + m_e\Gamma\frac{\mathrm{d}x}{\mathrm{d}t} + m_e\omega_0^2 x = -eE(t), \tag{1.14}$$

Fig. 1-14: fig:/Lorentz-model.eps

where m_e is mass of the electron, Γ is the damping constant, e is the electronic charge and $E(t)$ is time-harmonic electric field. We assume the time-harmonic dependence of the electric field as $e^{-i\omega t}$. Thus, the electric field is $E(t) = E_0 e^{-i\omega t}$. The further assumption is that the electron oscillates at the same frequency as the external light wave, that is, $x(t) = x_0 e^{-i\omega t}$. We can obtain the amplitude x_0 by substituting $x(t)$ and $E(t)$ into the Eq. (1.14) The solution of the displacement is then obtained as :

$$x(t) = \frac{-e/m_e}{\omega_0^2 - \omega^2 - i\Gamma\omega} E(t). \tag{1.15}$$

There is the induced electric dipole moment $\mu(t) = -ex(t)$ due to the electronic displacement $x(t)$ written in in Eq. (1.15). Then, the electronic resonant polarization P is obtained as the product of the electronic density n and the electric dipole moment $\mu(t)$: $P = n\mu(t)$. From the constitutive relation, $\vec{D} = \varepsilon_0 \varepsilon \vec{E} = \varepsilon_0 \varepsilon_\infty \vec{E} + \vec{P}_{resonant}$, where we introduce ε_∞ as the dielectric constant of non-resonant background, the complex dielectric constant $\tilde{\varepsilon}$ can be obtained as :

$$\tilde{\varepsilon} = \varepsilon_\infty + \frac{\omega_p^2}{\omega_0^2 - \omega^2 - i\Gamma\omega}, \tag{1.16}$$

where ω_p is the plasma frequency defined as $\omega_p = \sqrt{\frac{ne^2}{\varepsilon_0 m}}$. The real and imaginary parts of $\tilde{\varepsilon}$, that are, ε_1 and ε_2, respectively, are :

$$\varepsilon_1 = \varepsilon_\infty + \frac{\omega_p^2(\omega_0^2 - \omega^2)}{(\omega_0^2 - \omega^2)^2 + (\Gamma\omega)^2} \quad , \quad \varepsilon_2 = \frac{\omega_p^2 \Gamma\omega}{(\omega_0^2 - \omega^2)^2 + (\Gamma\omega)^2}. \tag{1.17}$$

The dielectric constant $\tilde{\varepsilon}$ at low frequency or static dielectric constant denoted by ε_s is obtained by taking the angular frequency ω as zero, and so $\varepsilon_s = \varepsilon_\infty + \omega_p^2/\omega_0^2$. At high frequency, the dielectric constant becomes the dielectric constant of the background ε_∞. Furthermore, it is convenient to express the dielectric constant in terms of wavelength for spectroscopic purpose. The $\varepsilon_1(\lambda)$ and $\varepsilon_2(\lambda)$ can be obtained by recalling the relation $\omega = 2\pi c/\lambda$. We also introduce two new parameters:(i) wavelength of the plasma frequency, $\omega_p = 2\pi c/\lambda_p$, and (ii) the damping constant in dimension of wavelength whose will be called the damping length in this thesis, $\omega_\Gamma = 2\pi c/\lambda_\Gamma$.

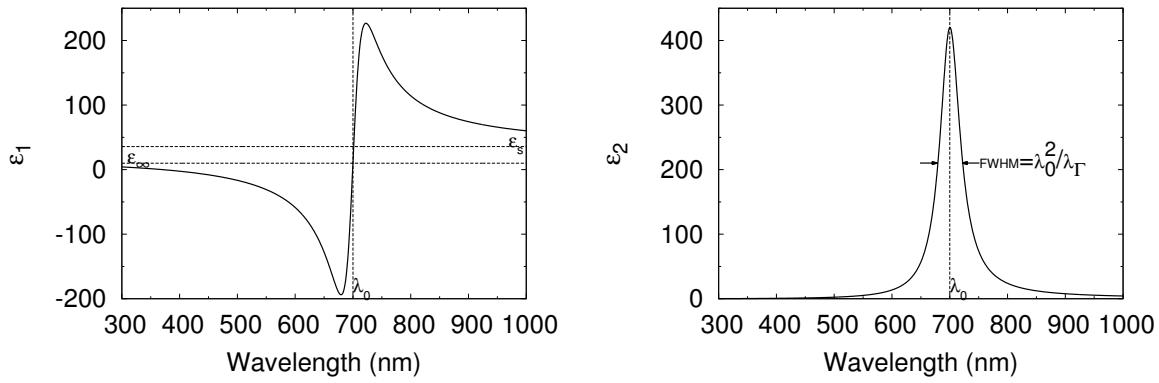

Figure 1-15: **Dielectric constant from Lorentz model** (a) Real part of the dielectric constant ε_1 as a function of wavelength from Lorentz model (b) Imaginary part of the dielectric constant ε_2 as a function of wavelength from Lorentz model

Then, ε_1 and ε_2 as a function of wavelength are expressed as

$$\varepsilon_1(\lambda) = \varepsilon_\infty + \frac{(1/\lambda_p^2)(1/\lambda_0^2 - 1/\lambda^2)}{(1/\lambda_0^2 - 1/\lambda^2)^2 + (1/\lambda_\Gamma^2)(1/\lambda^2)} \tag{1.18}$$

$$\varepsilon_2(\lambda) = \frac{(1/\lambda_p^2)(1/\lambda_\Gamma)(1/\lambda)}{(1/\lambda_0^2 - 1/\lambda^2)^2 + (1/\lambda_\Gamma^2)(1/\lambda^2)}. \tag{1.19}$$

Fig. 1-15 shows ε_1 and ε_2 from the Lorentz model as a function of wavelength by assuming parameters as: $\lambda_0 = 700$ nm, $\lambda_p = 137.9$ nm and $\lambda_\Gamma = 11.4$ μm. The imaginary part ε_2 get maximum at $\lambda = \lambda_0$, and then sharply decrease to zero with lowering or increasing wavelength away from λ_0. The full width at half maximum FWHM of the broadening can be determined by considering the wavelength near λ_0, so that it can be approximated that $\lambda \approx \lambda_0$ and $1/\lambda_0^2 - 1/\lambda^2 \approx 2(\triangle\lambda)/\lambda_0^3$ where $\triangle\lambda = \lambda - \lambda_0$. Using these approximations, the FWHM can be derived straightforwardly to be $\lambda_0^2/\lambda_\Gamma$ as indicated in Fig. 1-15(b). The behavior of the ε_1 is more complicate. The ε_1 at long wavelength is ε_s. It increases by lowering the wavelength toward λ_0 and finally get maximum at the wavelength $\lambda = \lambda_0 + \frac{\lambda_0^2}{2\lambda_\Gamma}$, and then decreases sharply passing through λ_0 until approaching the negative minimum point at the wavelength

Fig. 1-15: fig:/eps1Lorentz.eps

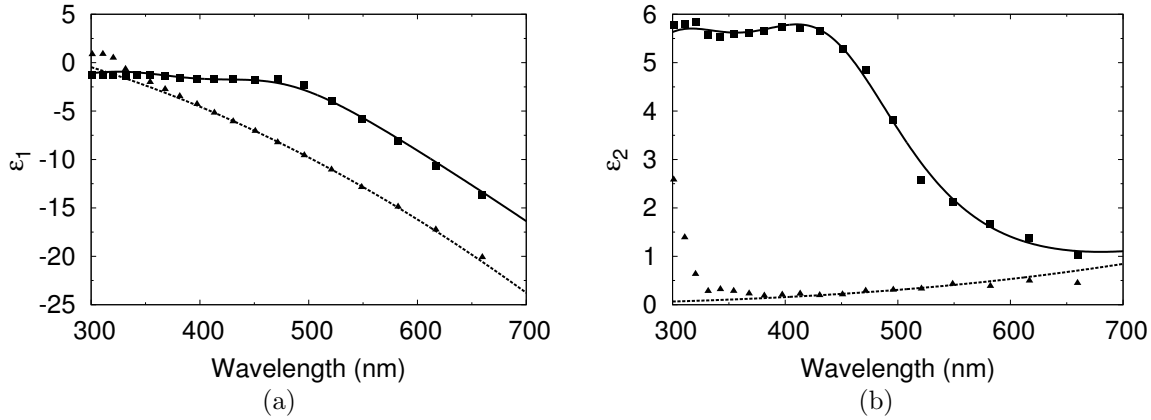

Figure 1-16: **Experimental dielectric constant** (a) The experimental ε_1 of Au and Ag are denoted by the solid rectangle and triangle, respectively. The fitting functions of ε_1 of Au and Ag are plotted as the solid and dashed lines, respectively. (b) The experimental ε_2 of Au and Ag are denoted by the solid rectangle and triangle, respectively. The fitting functions of ε_2 of Au and Ag are plotted as the solid and dashed lines, respectively [36, 37, 38].

$\lambda = \lambda_0 - \frac{\lambda_0^2}{2\lambda_\Gamma}$. By lowering wavelength more from the minimum point, ε_1 becomes increasing again and reaches ε_∞ at very short wavelength.

Experimental dielectric constant of bulk metals

The bulk dielectric constants of Ag and Au in the energy range 0.5 - 6.5 eV at room temperature have been measured by P.B. Johnson and R. W. Christy in 1972 [36]. These bulk dielectric constants are widely used until now. The experiment employed by Johnson and Christy is the measuring of the reflectance R and the transmittance T of a metallic thin film. The R is measured from the reflection at normal incident. Simultaneously, the T is measured from the transmission at normal incident and at angle of 60°. Then, these two quantities are converted into the complex refractive index $\tilde{n}$ of the metal by comparing with the theoretical expressions of R and T. Theoretically, the reflectance and transmittance are a function of $\tilde{n}$, the refractive index of the surrounding dielectric mediums, the angle of the incidence

Fig. 1-16: fig:/expeps1.eps

and the thickness of the metallic film [35]. Unfortunately, there are no analytical formulae of the conversion from R and T to $\tilde{n}$. The solutions of $\tilde{n}$ are thus obtained numerically by graphical method. After obtaining the complex refractive indices, the complex dielectric constants $\tilde{\varepsilon}$ are obtained by recalling the relation $\tilde{n} = \sqrt{\tilde{\varepsilon}}$ from the electromagnetic theory. The experimental ε_1 and ε_2 of Ag and Au are shown in Fig. 1-16 as a function of wavelength in the range 350-700 nm together with the fitting functions. The fitting function of the dielectric constant of Au has been given by P. G. Etchegoin et al [38], is expressed as follows

$$\begin{aligned} \tilde{\varepsilon}_{\mathrm{Au}} &= \varepsilon_\infty - \frac{1}{\lambda_p^2\,(1/\lambda^2 + i/\gamma_p\lambda)} + \\ &\sum_{i=1,2} \frac{A_i}{\lambda_i}\left[\frac{e^{i\phi_i}}{1/\lambda_i - 1/\lambda - i/\gamma_i} + \frac{e^{-i\phi_i}}{1/\lambda_i + 1/\lambda + i/\gamma_i}\right], \end{aligned} \tag{1.20}$$

where $\varepsilon_\infty = 1.54$, $\lambda_p = 143$ nm, $\gamma_p = 14500$ nm, $A_1 = 1.27$, $\phi_1 = -\pi/4$ radian, $\lambda_1 = 470$ nm, $\gamma_1 = 1900$ nm, $A_2 = 1.1$, $\phi_2 = -\pi/4$ radian, $\lambda_2 = 325$ nm, and $\gamma_2 = 1060$ nm. The fitting function of gold takes two contributions into account: (i) the Drude model, and (ii) the interband transition. However, the fitting function of silver given by S. Foteinopoulou et al. [37] has only the Drude term because there is no interband transition for Ag excited by the incident light in the visible region. The Drude fitting function of the dielectric constant of silver as a function of frequency is expressed as follows

$$\tilde{\varepsilon}(\omega) = \varepsilon_\infty - \frac{\omega_p^2}{\omega(\omega + i\Gamma_D)}, \tag{1.21}$$

where $\varepsilon_\infty = 4.785$, $\omega_p = 14.385 \times 10^{15}$ rad/s, and $\Gamma_D = 7.95 \times 10^{13}$ rad/s.

The different behavior of the dielectric constants of Ag and Au can be obviously seen by considering the ε_2 of these two materials shown in Fig. 1-16(b). The ε_2 of the Ag behaves as free electrons described by the Drude model in near infrared region and in the whole visible region because it decreases as lowering wavelength corresponding the ε_2 in Drude model. However, The ε_2 of the Ag becomes increasing at the wavelength around 368 nm due to the interband transition effect at $\lambda \approx 359$ nm as already mentioned in the section of Lorentz model. The ε_2 of Au increases

by lowering the wavelength in the visible region due to the effect of the interband transition at $\lambda \approx 470$ nm. The bulk dielectric constants of silver are valid for the silver films with the thicknesses $d \geq 30.4$ nm. This is called the critical thickness. For gold, the critical thickness is 25 nm which is smaller than the critical thickness of silver. When the thickness is smaller than this critical point, the dielectric constant is dependent on the thickness [36].

Chapter 2

Calculation method

This chapter mainly shows how to solve for the electromagnetic field scattered by a metallic sphere. Once a metallic tip is modeled as the metallic sphere with the same radius as the apex of the metallic tip, the problem can be solved analytically and classically based on Maxwell equations. The solutions of this problem are called Mie's theory. The electric field enhancement from Mie's theory is given as a function of wavelength of laser light and radius of the metallic sphere using dielectric constant in Fig. 1-16. In order to understand physics of the calculated electric field enhancement from Mie's theory, the quasi-static approximation and the dipole radiation are reviewed in section 2.1 and section 2.2, respectively, before Mie's theory given in section 2.3. Finally, the exciton theory in carbon nanotube is reviewed in section 2.4 because the interaction between the near field and carbon nanotube can be explained in term of the exciton theory.

2.1 Quasi-static approximation

Quasi-static approximation is applied to the metallic sphere which is much smaller than the wavelength of the incident light, and the incident electric field is constant over the volume of the metallic sphere. Then, the electric field is considered to be static, but temporally it oscillates with time harmonic $e^{-i\omega t}$ [39]. The scattered electric field $\boldsymbol{E}^{\mathrm{s}}$ outside the metallic sphere and the internal electric field inside the metallic sphere

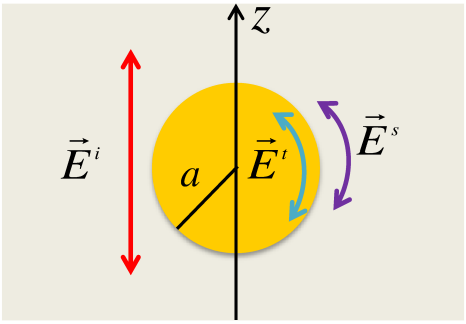

Figure 2-1: **Geometry of the quasi-static approximation.** The incident electric field $\boldsymbol{E}^{\mathrm{i}}$ indicated by the red arrow is constant over the volume of the metallic sphere with radius a. The arrow indicates that $\boldsymbol{E}^{\mathrm{i}}$ is oscillating with time harmonic $e^{-i\omega t}$. The internal electric field $\boldsymbol{E}^{\mathrm{t}}$ is represented by the blue arrow, and the scattered electric field $\boldsymbol{E}^{\mathrm{s}}$ is indicated by the purple arrow. The total electric field outside the metallic sphere is the sum of $\boldsymbol{E}^{\mathrm{i}}$ and $\boldsymbol{E}^{\mathrm{s}}$ while the total electric field inside the metallic sphere is $\boldsymbol{E}^{\mathrm{t}}$.

$\boldsymbol{E}^{\mathrm{t}}$ are obtained by the scalar potential Φ using the relation $\boldsymbol{E} = -\nabla\Phi$. The scalar potential inside and outside the metallic sphere is obtained by solving the Laplace's equation, $\nabla^2\Phi = 0$, in the spherical coordinate, which is written as :

$$\frac{1}{r}\frac{\partial^2}{\partial r^2}(r\Phi) + \frac{1}{r^2\sin\theta}\frac{\partial}{\partial\theta}(\sin\theta\frac{\partial\Phi}{\partial\theta}) + \frac{1}{r^2\sin^2\theta}\frac{\partial^2\Phi}{\partial\phi^2} = 0. \tag{2.1}$$

The separation of variable is applied to solve Eq. (2.1) by writing the scalar potential as $\Phi = R(r)P(\theta)Q(\phi)$. Then, three ordinary differential equations of each variable are obtained :

$$\frac{1}{Q(\phi)}\frac{\mathrm{d}^2Q(\phi)}{\mathrm{d}\phi^2} + m^2Q(\phi) = 0, \tag{2.2}$$

$$\frac{1}{\sin\theta}\frac{\mathrm{d}}{\mathrm{d}\theta}(\sin\theta\frac{\mathrm{d}P(\theta)}{\mathrm{d}\theta}) + [l(l+1) - \frac{m^2}{\sin^2\theta}]P(\theta) = 0, \tag{2.3}$$

$$r^2\frac{\mathrm{d}^2}{\mathrm{d}r^2}(rR(r)) = l(l+1)(rR(r)). \tag{2.4}$$

Fig. 2-1: fig:/fig:quasi-static-geo.eps

Therefore, the general solution of the potential Φ is written as :

$$\Phi(r,\theta,\phi) = \sum_{l=0}^{\infty}\sum_{m=0}^{l}\left(a_{lm}r^l + \frac{b_{lm}}{r^{l+1}}\right)P_l^m(\cos\theta)e^{im\phi}, \tag{2.5}$$

where $P_l^m(\cos\theta)$ are the associated Legendre polynomial. The internal potential Φ^{t} must be finite at the origin, thus $b_{lm} = 0$ for the potential inside the metallic sphere. In the region outside the metallic sphere, the scattered potential Φ^{s} should be zero at infinity, thus a_{lm} must be zero for the potential outside the metallic sphere. The incident electric field $\boldsymbol{E}^{\mathrm{i}}$ is assumed to be polarized along the z axis, that is, $\boldsymbol{E}^{\mathrm{i}} = E_0\hat{e}_z$, then the potential of the incident electric field is written as $\Phi^{\mathrm{i}} = -E_0 z = -E_0 r P_1(\cos\theta)$. The total potential outside the metallic sphere is the sum between the potentials of the incident light and the scattered field $\Phi^{\mathrm{out}} = \Phi^{\mathrm{i}} + \Phi^{\mathrm{s}}$, and the total potential inside the metallic sphere is the internal potential $\Phi^{\mathrm{in}} = \Phi^{\mathrm{t}}$. The geometry of the quasi-static approximation is shown in Fig. 2-1. The coefficients a_{lm} of the internal field and b_{lm} of the scattered field are then obtained using the continuity of the tangential component of the electric field and the continuity of the radial component of the electric displacement at the surface of the metallic ball ($r = a$) :

$$\frac{\partial\Phi^{\mathrm{out}}}{\partial\theta}\Big|_{r=a} = \frac{\partial\Phi^{\mathrm{in}}}{\partial\theta}\Big|_{r=a}, \tag{2.6}$$

$$\varepsilon_m\frac{\partial\Phi^{\mathrm{out}}}{\partial r}\Big|_{r=a} = \tilde{\varepsilon}\frac{\Phi^{\mathrm{in}}}{\partial r}\Big|_{r=a}, \tag{2.7}$$

where a is the radius of the metallic sphere, ε_m is the dielectric constant of the dielectric medium and $\tilde{\varepsilon}$ is the complex dielectric constant of the metallic sphere which depends on the frequency (wavelength) of the incident light. The relation between the Legendre polynomial and the associated Legendre polynomial, that is, $\frac{\mathrm{d}P_l(\cos\theta)}{\mathrm{d}\theta} = -P_l^1(\cos\theta)$ is required for Eq. (2.6). It can be seen that $m = 0$ for the scattered and internal fields because the incident light is polarized along z axis, and

if the incident light is polarized along x axis, $m = 1$. Then Eq.(2.6) becomes

$$E_0 a P_1^1(\cos\theta) - \sum_{l=1}^{\infty} \frac{b_{l0}}{a^{l+1}} P_l^1(\cos\theta) = -\sum_{l=1}^{\infty} a_{l0} a^l P_l^1(\cos\theta). \tag{2.8}$$

Recalling the orthogonality of the associated Legendre polynomial, the first linear equation of the coefficients can be written as :

$$a^l a_{l0} - \frac{1}{a^{l+1}} b_{l0} = -a E_0 \delta_{l1}. \tag{2.9}$$

The second linear equation is obtained from Eq. (2.7) using the orthogonality of the Legendre polynomial, and it is written as :

$$\tilde{\varepsilon} l a^{l-1} a_{l0} + \varepsilon_m \frac{l+1}{a^{l+2}} b_{l0} = -\varepsilon_m E_0 \delta_{l1}. \tag{2.10}$$

By solving Eq. (2.9) and Eq. (2.10), the coefficients a_{l0} and b_{l0} are obtained :

$$a_{10} = -\Big(\frac{3\varepsilon_m}{\tilde{\varepsilon} + 2\varepsilon_m}\Big) E_0 \qquad , \qquad b_{10} = \Big(\frac{\tilde{\varepsilon} - \varepsilon_m}{\tilde{\varepsilon} + 2\varepsilon_m}\Big) a^3 E_0, \tag{2.11}$$

$a_{l0} = 0$ and $b_{l0} = 0$ if $l \neq 1$. Therefore, the electric field has only the dipole term which get resonance when $\tilde{\varepsilon} = -2\varepsilon_m$. The dipole resonance condition can be satisfied for the Ag sphere embedded in the vacuum at the wavelength about 350 nm where the real part has a value about -2.0 and the imaginary part is relatively small as shown in Fig. 1-16. The scattered electric field $\boldsymbol{E}^{\mathrm{s}}$ and the internal field $\boldsymbol{E}^{\mathrm{t}}$ obtained from the gradient of the scattered potential Φ^{s} and the internal potential Φ^{t}, respectively, are then expressed as [39] :

$$\boldsymbol{E}^{\mathrm{s}} = E_0 \Big(\frac{\tilde{\tilde{\varepsilon}} - \varepsilon_m}{\tilde{\tilde{\varepsilon}} + 2\varepsilon_m}\Big) \Big(\frac{a}{r}\Big)^3 (2\cos\theta \hat{e}_r + \sin\theta \hat{e}_\theta), \tag{2.12}$$

$$\boldsymbol{E}^{\mathrm{t}} = 3E_0 \Big(\frac{\varepsilon_m}{\tilde{\tilde{\varepsilon}} + 2\varepsilon_m}\Big) \hat{e}_z. \tag{2.13}$$

For a perfect conductor, the amplitude of the imaginary part of $\tilde{\varepsilon}$ is much larger

Fig. 2-2: fig:/fig:staticEFE.eps

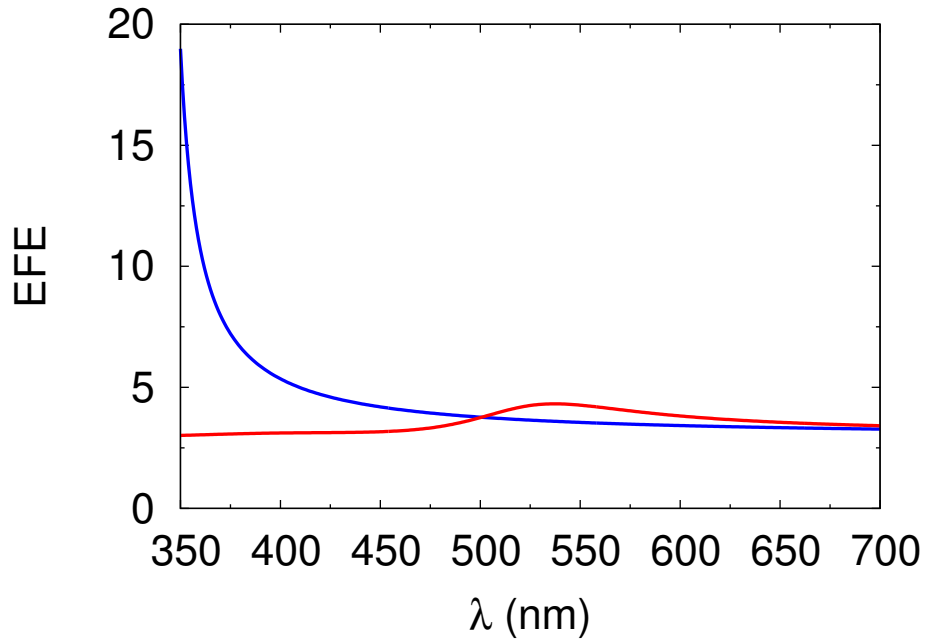

Figure 2-2: **The electric field enhancement EFE of Ag and Au spheres from the quasi-static approximation.** The blue line represents the EFE of the small Ag sphere and the red line represents the EFE of the small Au sphere. The dielectric constants of Ag and Au are obtained from fitting functions [37, 38].

than ε_m, then the internal field $\boldsymbol{E}^{\mathrm{t}}$ becomes almost zero . Furthermore, the scattered electric field $\boldsymbol{E}^{\mathrm{s}}$ expressed in Eq. (2.12) is identical to the electric field due to the static dipole moment $p = \varepsilon_m \alpha E_0$ where α is the polarizability written as $\alpha = 4\pi a^3 \left(\frac{\tilde{\varepsilon} - \varepsilon_m}{\tilde{\varepsilon} + 2\varepsilon_m} \right)$, placed at the center of the sphere. The electric field due to the oscillating electric dipole moment will be given in the next section. We are interested in the electric field enhancement EFE which is defined as the ratio between the maximum of the total electric field outside the metallic sphere and the amplitude of the incident electric field. The maximum of the total electric field $\boldsymbol{E}^{\mathrm{out}}$ always occurs at the surface of the metallic sphere and on the polarization axis. The scattered electric field at the maximum point is then $E^{\mathrm{s}}_{\mathrm{max}} = 2E_0 \left(\frac{\tilde{\varepsilon} - \varepsilon_m}{\tilde{\varepsilon} + 2\varepsilon_m} \right)$, and the maximum of the total electric field becomes $E^{\mathrm{out}}_{\mathrm{max}} = E^{\mathrm{s}}_{\mathrm{max}} + E_0 = \left(\frac{3\tilde{\varepsilon}}{\tilde{\varepsilon} + 2\varepsilon_m} \right) E_0$. Therefore, the electric field enhancement can be written explicitly as :

$$EFE = 3 \left| \frac{\tilde{\varepsilon}}{\tilde{\varepsilon} + 2\varepsilon_m} \right| . \tag{2.14}$$

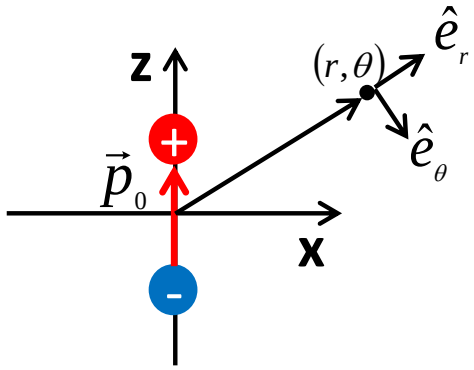

Figure 2-3: The electric dipole moment $\vec{p}_0$ polarized along z-axis placed at the origin, $\vec{p} = \vec{p}_0 e^{-i\omega t}$, where $\hat{e}_z$ is the unit vector in the direction of z. $\hat{e}_r$ and $\hat{e}_\theta$ are unit vectors in the spherical coordinate in the direction of r and θ, respectively.

The electric field enhancement EFE depends only on the wavelength of the incident light and the dielectric constant of the medium. It does not depend on the radius of the metallic sphere, which does not work for the large metallic sphere comparing with the wavelength of the incident light in which the retardation effect due to the size of the metallic sphere is important [32]. The retardation effect is included in the Mie's theory which is fully described later in section 2.3.

Here, the electric field enhancement EFE as a function of wavelength of the small Ag and Au spheres embedded in vacuum is shown in Fig. 2-2. The dielectric constant of Ag and Au are taken from the fitting functions as shown in Fig. 1-16 [37, 38]. High EFE has been found for the small Ag sphere in the region of blue light. The EFE of the small Au sphere in this region is low compared to the Ag. At wavelength 350 nm corresponding to the dielectric constants $\varepsilon_{Ag} = -2.36 + 0.11i$ and $\varepsilon_{Au} = -1.08 + 5.63i$ [37, 38] , the EFE of the small Ag and Au spheres are 19.0 and 3.0, respectively. The high electric field enhancement of the small Ag sphere at the wavelength 350 nm is a result of the dipole resonance.

Fig. 2-3: fig:/fig:dipole.eps

2.2 Dipole radiation and dynamic depolarization

This section reviews the dynamic depolarization effect due to the electric dipole moments in the metallic sphere as proposed by M. Meier and A. Wokaun [41]. The dynamic depolarization results in the appearance of the enhancement maximum at a small but finite volume of the metallic sphere in Mie's theory. It is also responsible for the shift of the resonance at larger volume.

2.2.1 Dipole radiation

Most materials can be polarized by an electric field. The polarization is defined as numbers of electric dipole moments $\boldsymbol{p}$ per unit volume. If the electric field is oscillating with time harmonic $e^{-i\omega t}$ where ω is angular frequency, the dipoles will oscillate with time at the same frequency as the electric field resulting in the radiation. The electric field of the oscillating dipole $\boldsymbol{p} = \boldsymbol{p}_0 e^{-i\omega t}$ at the distance $\boldsymbol{r}$ from the dipole in the vacuum is expressed as :

$$\boldsymbol{E}(\boldsymbol{r}) = \frac{ck\omega\mu_0}{4\pi}\frac{e^{ikr}}{r}\hat{\boldsymbol{e}}_r \times (\boldsymbol{p}_0 \times \hat{\boldsymbol{e}}_r) + \frac{1}{4\pi\varepsilon_0}\Big(\frac{1}{r^3} - \frac{ik}{r^2}\Big)e^{ikr}[3(\hat{\boldsymbol{e}}_r \cdot \boldsymbol{p}_0)\hat{\boldsymbol{e}}_r - \boldsymbol{p}_0], \quad (2.15)$$

where c is the velocity of light in vacuum, k is wave number of light in vacuum, μ_0 is the permeability of vacuum, ε_0 is the permittivity of vacuum [40]. Here, the dipole is oriented along z-axis, that is, $\boldsymbol{p}_0 = p_0\hat{\boldsymbol{e}}_z$, as shown in Figure (2-3) where the azimuthal symmetry is assumed. Unit vectors $\hat{\boldsymbol{e}}_r$ and $\hat{\boldsymbol{e}}_\theta$ in the spherical coordinate can be written in term of $\hat{\boldsymbol{e}}_z$ and $\hat{\boldsymbol{e}}_x$ in direction parallel and perpendicular to the dipole, respectively, as $\hat{\boldsymbol{e}}_r = \sin\theta\hat{e}_x + \cos\theta\hat{\boldsymbol{e}}_z$, $\hat{\boldsymbol{e}}_\theta = \cos\theta\hat{\boldsymbol{e}}_x - \sin\theta\hat{\boldsymbol{e}}_z$. Then, the vector product of the first term of Eq. (2.15) becomes $\hat{\boldsymbol{e}}_r \times (\boldsymbol{p}_0 \times \hat{\boldsymbol{e}}_r) = -p_0 \sin\theta\hat{\boldsymbol{e}}_\theta$, and the dot product of the second term of Eq. (2.15) becomes $3(\hat{\boldsymbol{e}}_r \cdot \boldsymbol{p}_0)\hat{\boldsymbol{e}}_r - \boldsymbol{p}_0 = 2p_0\cos\theta\hat{\boldsymbol{e}}_r + p_0\sin\theta\hat{\boldsymbol{e}}_\theta$. The electric field is then written in the spherical coordinate as :

$$\begin{aligned}\boldsymbol{E}(\boldsymbol{r}) \;=\; & \frac{1}{2\pi\varepsilon_0}\Big(\frac{1}{r^3} - \frac{ik}{r^2}\Big)(p_0 e^{ikr})\cos\theta\hat{\boldsymbol{e}}_r + \\ & \frac{1}{4\pi\varepsilon_0}\Big(\frac{1}{r^3} - \frac{ik}{r^2} - \frac{k^2}{r}\Big)(p_0 e^{ikr})\sin\theta\hat{\boldsymbol{e}}_\theta\end{aligned}$$

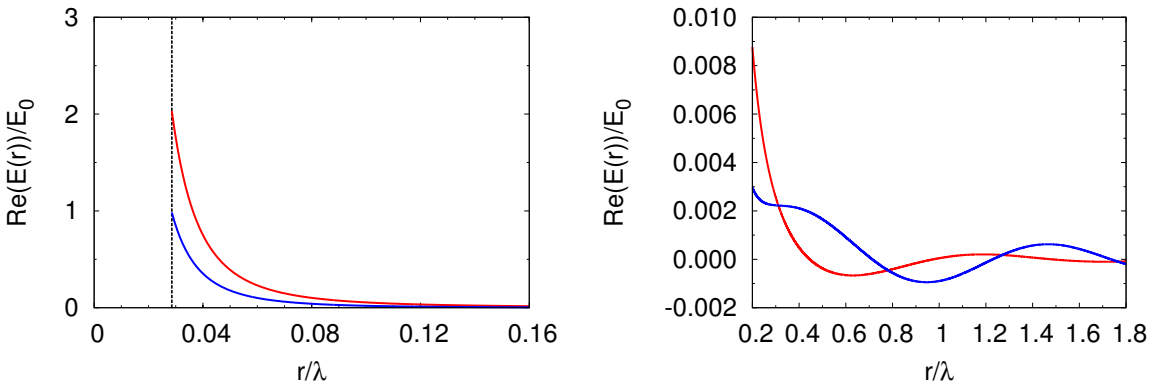

Figure 2-4: **Re$(E(r))/E_0$ as a function of radial distance r:** The dipole electric field $E(r)$ is generated by the electric dipole moment $p_0 = 4\pi\varepsilon_0\left(\frac{\tilde{\varepsilon}-\varepsilon_0}{\tilde{\varepsilon}+2\varepsilon_0}\right)a^3E_0$ where $\tilde{\varepsilon}$ and a are the dielectric constant and radius of the metallic sphere, respectively. a is defined as 10 nm. The wavelength of the incident light is 350 nm, and the corresponding bulk dielectric constant of the Ag is $\tilde{\varepsilon}_{\rm Ag} = -2.36 + 0.11i$ [37]. (a) $\mathrm{Re}(E(r))/E_0$ as a function of r when $\theta = 0$ represented by the red curve and $\theta = \pi/2$ represented by the blue curve in the near field region $r \ll 0.16\lambda$. The dashed black line denote $r = 10$ nm corresponding to the radius of the Ag sphere. (b) $\mathrm{Re}(E(r))/E_0$ as a function of r when $\theta = 0$ represented by the red curve and $\theta = \pi/2$ represented by the blue curve in the far field region $r \gg 0.16\lambda$.

$$= \quad E_r\hat{\boldsymbol{e}}_r + E_\theta\hat{\boldsymbol{e}}_\theta. \tag{2.16}$$

p_0e^{ikr} is known as the retarded dipole, and it may be simply written as $[p] = p_0e^{ikr}$. Here, the retarded dipole means that it starts to radiate the electromagnetic wave at time $t - r/c$ where r is the distance between the observer and the radiating dipole. In the near field region ($kr << 1$) (or in the very close region to the electric dipole), the dominant term is proportional to $1/r^3$. The electric field in the near field region $\boldsymbol{E}^{\rm nf}$ is then written as :

$$\boldsymbol{E}^{\rm nf} = \frac{1}{4\pi\varepsilon_0}\left(\frac{p_0}{r^3}\right)(2\cos\theta\hat{\boldsymbol{e}}_r + \sin\theta\hat{\boldsymbol{e}}_\theta). \tag{2.17}$$

Therefore, the scattered electric field $\vec{E}^{\rm s}$ obtained from the quasi-static approximation

Fig. 2-4(a): fig:/fig:Edipole-nf.eps
Fig. 2-4(b): fig:/fig:Edipole-ff.eps

in Eq. (2.12) is recovered if the electric dipole moment in the vacuum is equal to $p_0 = 4\pi\varepsilon_0\left(\frac{\tilde{\varepsilon}-\varepsilon_0}{\tilde{\varepsilon}+2\varepsilon_0}\right)a^3E_0$.

In Fig. 2-4, we plot $\mathrm{Re}(E(r))/E_0$ as a function of r for $\theta = 0$ and $\theta = \pi/2$, where $E(r)$ is the dipole electric field as expressed in Eq. (2.16). The electric dipole moment $p_0 = 4\pi\varepsilon_0\left(\frac{\tilde{\varepsilon}-\varepsilon_0}{\tilde{\varepsilon}+2\varepsilon_0}\right)a^3E_0$ is in the small Ag sphere with radius a and the dielectric constant $\tilde{\varepsilon}_{\mathrm{Ag}}$. The radius a is defined as 10 nm. The wavelength of the incident light is 350 nm, and the dielectric constant of Ag at this wavelength is approximated to be $\tilde{\varepsilon}_{\mathrm{Ag}} = -2.36 + 0.11i$ [37] which corresponds to the bulk dielectric constant of Ag. We divide the radial distance into the near field region where $kr \ll 1$ or $r \ll 0.16\lambda$ is satisfied and the far field region where $kr \gg 1$ or $r \gg 0.16\lambda$ is satisfied. Firstly, in both two regions, there is only the radial part of the electric field $E_r(r)$ along the line $\theta = 0$ which is parallel to the polarization axis, and there is only the polar part of the electric field $E_\theta(r)$ along the line $\theta = \pi/2$ which is perpendicular to the polarization axis, as seen in Eq. (2.16) and Fig. 2-3. In near field region as shown in Fig. 2-4(a), the electric field strongly decays by increasing r due to the near field term proportional to $1/r^3$. The maximum of the dipole electric field is about twice of the incident electric field which occurs at the surface of the Ag sphere with $\theta = 0$. In the far field region as shown in Fig. 2-4(b), the amplitude of the dipole electric field is very small compared to the amplitude of the incident electric field. The dominant term of the dipole electric field in this region is proportional to $1/r$ which only appears in the polar part of the dipole electric field, E_θ. E_r of the dipole electric field is very small compared to E_θ in the far field region. Therefore, the dipole electric field in the far field region is an outgoing wave which travels out from the source and has only a polar component.

2.2.2 Dynamic depolarization

The electric field generated by polarized oscillating dipoles in the metallic sphere causes the depolarization electric field $\boldsymbol{E}_{\mathrm{dep}}$. Therefore, the polarization $\boldsymbol{P}$ of the

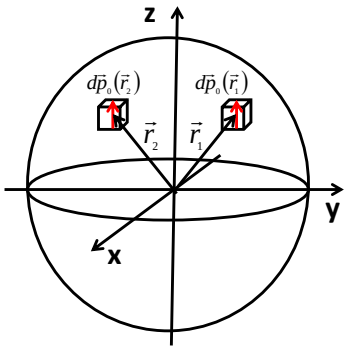

Figure 2-5: The small polarized dipole $\mathrm{d}\boldsymbol{p}(\boldsymbol{r})$ placed at the center of the small volume $\mathrm{d}V(r,\theta,\phi)$ inside the metallic sphere. The corresponding depolarization electric field of the dipole $\mathrm{d}\boldsymbol{p}(\boldsymbol{r})$ is $\mathrm{d}\boldsymbol{E}_{\mathrm{dep}}(\boldsymbol{r})$

metallic sphere embedded in the vacuum is expressed as (SI) :

$$\boldsymbol{P} = \varepsilon_0(\tilde{\varepsilon} - 1)(\boldsymbol{E}_0 + \boldsymbol{E}_{\mathrm{dep}}), \tag{2.18}$$

where $\boldsymbol{E}_0$ is an external electric field.

The depolarization electric field $\boldsymbol{E}_{\mathrm{dep}}$ can be obtained by considering the metallic sphere as the collection of small polarized oscillating dipoles $\mathrm{d}\boldsymbol{p}(\boldsymbol{r})$ placed at the center of the volume element $\mathrm{d}V(r,\theta,\phi)$ of metallic sphere as shown in Figure (2-5). The corresponding depolarization electric field $\mathrm{d}\boldsymbol{E}_{\mathrm{dep}}(\boldsymbol{r})$ due to the oscillating dipole is expressed in Eq. (2.16). $\boldsymbol{E}_{\mathrm{dep}}$ is then obtained by integrating $\mathrm{d}\boldsymbol{E}_{dep}(\boldsymbol{r})$ over the volume of metallic sphere with the radius a. As the components perpendicular to $\boldsymbol{E}_0$ cancel on the integration, only the parallel component $\mathrm{d}E_{\mathrm{dep},z}$ must be considered.

By expanding the exponential e^{ikr} of the depolarization electric field written in Eq. (2.16) as $e^{ikr} \approx 1 + ikr - \frac{k^2r^2}{2} - \frac{ik^3r^3}{6}$ and then retaining only the terms up to order k^3, the depolarization electric field $\mathrm{d}\boldsymbol{E}_{\mathrm{dep}}$ is then written as :

$$\begin{aligned}
\mathrm{d}\boldsymbol{E}_{\mathrm{dep}} &= \frac{1}{2\pi\varepsilon_0}\Big(\frac{1}{r^3} + \frac{k^2}{2r} + \frac{ik^3}{3}\Big)(\mathrm{d}p_0\cos\theta)\hat{\boldsymbol{e}}_r + \\
&\quad \frac{1}{4\pi\varepsilon_0}\Big(\frac{1}{r^3} - \frac{k^2}{2r} - \frac{2ik^3}{3}\Big)(\mathrm{d}p_0\sin\theta)\hat{\boldsymbol{e}}_\theta \\
&= \mathrm{d}E_{\mathrm{dep},r}\hat{\boldsymbol{e}}_r + \mathrm{d}E_{\mathrm{dep},\theta}\hat{\boldsymbol{e}}_\theta.
\end{aligned} \tag{2.19}$$

Fig. 2-5: fig:/fig:depolarization.eps

By converting the unit vectors $\hat{\boldsymbol{e}}_r$ and $\hat{\boldsymbol{e}}_\theta$ into $\hat{\boldsymbol{e}}_x$ and $\hat{\boldsymbol{e}}_z$, the parallel component of the depolarization electric field $\mathrm{d}E_{\mathrm{dep},z}$ can be written as :

$$\begin{aligned} \mathrm{d}E_{\mathrm{dep},z} &= \mathrm{d}E_{\mathrm{dep},r}\cos\theta - \mathrm{d}E_{\mathrm{dep},\theta}\sin\theta \\ &= \frac{\mathrm{d}p_0}{4\pi\varepsilon_0}\Big[\frac{1}{r^3}(3\cos^3\theta - 1) + \frac{k^2}{2r}(\cos^2\theta + 1) + \frac{2ik^3}{3}\Big]. \end{aligned} \tag{2.20}$$

By integrating Eq. (2.20) over the volume of the metallic sphere with radius a, the total depolarization electric field $\boldsymbol{E}_{dep}$ is then written as follows [41] :

$$\boldsymbol{E}_{\mathrm{dep}} = \frac{1}{\varepsilon_0}\Big(-\frac{1}{3} + \frac{1}{3}x^2 + \frac{2i}{9}x^3\Big)\boldsymbol{P}, \tag{2.21}$$

where $x = ka$. The constant term $-\frac{\boldsymbol{P}}{3\varepsilon_0}$ is included to account for the depolarization electric field of a small metallic sphere. If the polarization $\boldsymbol{P} = p_0/V = 3\varepsilon_0\Big(\frac{\tilde{\varepsilon}-\varepsilon_0}{\tilde{\varepsilon}+2\varepsilon_0}\Big)E_0$, the summation $E_{\mathrm{dep}} + E_0$ is the same as the internal field written in Eq. (2.13), obtained from the quasi-static approximation. By substituting the depolarization electric field in Eq. (2.21) into Eq. (2.18) and then solving for the polarization $\boldsymbol{P}$, then $\boldsymbol{P}$ is obtained as :

$$\boldsymbol{P} = \frac{3\varepsilon_0(\tilde{\varepsilon}-1)\boldsymbol{E}_0}{(\tilde{\varepsilon}+2) - (\tilde{\varepsilon}-1)x^2 - (2i/3)(\tilde{\varepsilon}-1)x^3} = \varepsilon_0\alpha E_0, \tag{2.22}$$

and the polarizability α per unit volume is written as :

$$\alpha = \frac{3(\tilde{\varepsilon}-1)}{(\tilde{\varepsilon}+2) - (\tilde{\varepsilon}-1)x^2 - (2i/3)(\tilde{\varepsilon}-1)x^3}. \tag{2.23}$$

The amplitude of the polarizability α per unit volume as expressed in Eq. (2.23) of the Ag-sphere as a function of $x = ka$ by defining the wavelength of the external light as $\lambda = 500$ nm with the corresponding wave number $k = 0.01256$ 1/nm is shown in Figure (2-6). The bulk dielectric constant of Ag at wavelength 500 nm obtained from the fitting function is $\tilde{\varepsilon}_{Ag} = -9.8 + 0.31i$ [37].

According to Fig. 2-6, the magnitude of the polarizability per unit volume is the maximum about 9.2 at $x \approx 0.73$. The radius of the silver sphere at this maximum

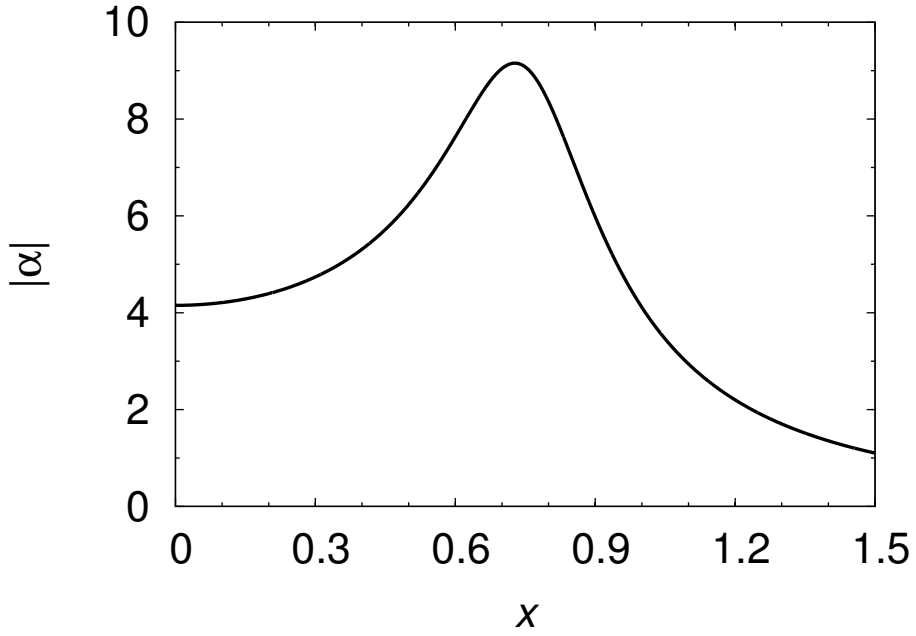

Figure 2-6: Amplitude of the polarizability $|\alpha|$ of the depolarized $\vec{P}$ of the Ag spheres as a function of $x = ka$. The wavelength of the external light is $\lambda = 500$ nm with the corresponding wave number $k = 0.012591/\text{nm}$ ($k = 2\pi/\lambda$). The bulk dielectric constant of Ag is taken from the fitting function [37].

point is $a \approx 0.73/k = 58$ nm. The polarizability decreases from the maximum point by increasing the radius larger than 58 nm. This phenomena can be explained as follows; for a small volume sphere, the term $(2i/3)(\tilde{\varepsilon} - 1)x^3$ is small compared to the term $(\tilde{\varepsilon} - 1)x^2$, then the polarizability is approximated as $\alpha = \frac{3(\tilde{\varepsilon}-1)}{(\tilde{\varepsilon}+2)-(\tilde{\varepsilon}-1)x^2}$. By increasing x (increasing radius), α increases and becomes maximum at the finite volume due to the term $(\tilde{\varepsilon} - 1)x^2$. This term is declared as the "dynamic depolarization", after M. Meier and A. Wokaun [41]. For larger metallic sphere, the term $(2i/3)(\tilde{\varepsilon} - 1)x^3$ cannot be neglected. It accounts for the damping of the dipole by radiative losses, and also results in broadening and a strongly decreased amplitude of the α. This similar phenomena also occurs in Mie's theory in which the maximum of the electric field enhancement (EFE) occurs at the small but finite volume, and drastically decreases and broadens upon increasing the volume of the metallic sphere from the maximum point. Mie's theory will be fully explained in the next section.

Fig. 2-6: fig:/fig:alpha-dep.eps

2.3 Mie's theory

A metal is an absorbing material because the dielectric constant has an imaginary part. When, an external light (laser light) is incident on a metallic sphere, then the electric current flows resulting in the absorption of the electromagnetic field. The electromagnetic field inside the metallic sphere is called the internal field. Furthermore, the oscillating of charges and current in the metallic sphere radiates the secondary electromagnetic field called the scattered wave outward from the metallic sphere. The space is then divided into two regions: (i) outside the metallic sphere and (ii) inside the metallic sphere. It is assumed that the metallic sphere is embedded within the non-absorbing dielectric with dielectric constant ε where the incident light and the scattered wave are travelling. Firstly, we look for the solutions of the scattered wave travelling outward from the metallic sphere. Secondly, the solutions of the internal fields can be solved by similar way as the scattered wave. Lastly, the coefficients of the scattered wave and the internal field are calculated using the boundary conditions.

Hereafter, the time-harmonic dependence of the electric and magnetic fields is assumed to be $e^{-i\omega t}$ where ω is frequency of the incident light.

2.3.1 Solution of the scattered wave

The Maxwell's equations of the electromagnetic wave travelling in the non-absorbing dielectric with dielectric constant ε are:

$$\nabla \cdot \boldsymbol{E} = 0, \tag{2.24}$$

$$\nabla \cdot \boldsymbol{B} = 0, \tag{2.25}$$

$$\nabla \times \boldsymbol{E} = i\omega \boldsymbol{B}, \tag{2.26}$$

$$\nabla \times \boldsymbol{B} = -i\varepsilon \frac{k_0}{c} \boldsymbol{E}, \tag{2.27}$$

where $\boldsymbol{E}$ is the electric field, $\boldsymbol{B}$ is the magnetic field, k_0 is wavenumber in vacuum and c is velocity of light in vacuum. The wave equations of $\boldsymbol{E}$ and $\boldsymbol{B}$ are obtained by taking curl to Eq. (2.26) and Eq. (2.27), respectively. Using the vector identity

$\nabla \times \nabla \times \boldsymbol{E} = \nabla(\nabla \cdot \boldsymbol{E}) - \nabla^2 \boldsymbol{E}$ and Gauss's laws, the wave equations are obtained:

$$(\nabla^2 + k^2)\boldsymbol{E} = 0 \quad , \quad (\nabla^2 + k^2)\boldsymbol{B} = 0 \tag{2.28}$$

where $k = \sqrt{\varepsilon} k_0$ is the wavenumber of the incident light and the scattered wave in the dielectric medium. Eq. (2.28) are known as the vector Helmholtz equations. Each component (r, θ, ϕ) of the vector Laplacians $\nabla^2 \boldsymbol{E}$ in spherical coordinate are given in Appendix $(A.1.2)$. Only the radial component of the electric field $E_r(B_r)$ is separable from another components. Therefore, $E_r(B_r)$ can be solved directly from the vector Helmholtz equations. In order to solve for the other components of the electric field (E_θ, E_ϕ) and those of the magnetic field (B_θ, B_ϕ), we must separate the general solutions of the electromagnetic field into two modes, that is, (i) transverse magnetic mode or TM mode and (ii) transverse electric mode or TE mode. As indicated by their names, TM mode has no radial component of the magnetic field or $B_r = 0$ but $E_r \neq 0$, and TE mode has no radial component of the electric field or $E_r = 0$ but $B_r \neq 0$. TM mode corresponds to the electric vibration where as the TE mode is related to the magnetic vibration in the metallic sphere. Importantly, the general solution of the electromagnetic wave is the sum of TM and TE modes.

TM mode of the scattered wave

Let's us firstly find the solutions of E_r in TM mode. The differential equation of E_r in spherical coordinate is expressed as :

$$\frac{1}{r^2}\frac{\partial^2}{\partial r^2}(r^2 E_r) + \frac{1}{r^2 \sin\theta}\frac{\partial}{\partial \theta}\left(\sin\theta \frac{\partial E_r}{\partial \theta}\right) + \frac{1}{r^2 \sin^2\theta}\frac{\partial^2 E_r}{\partial \phi^2} + k^2 E_r = 0 \tag{2.29}$$

The separation of variable technique is employed to solve Eq. (2.29) by writing the solution of E_r as $E_r = \frac{R(r)}{r} P(\theta) Q(\phi)$. By substituting the separable E_r into Eq. (2.29), the three ordinarily differential equations of each function, $R(r), P(\theta)$ and $Q(\phi)$ are obtained :

$$\frac{\mathrm{d}^2}{\mathrm{d}r^2}(rR(r)) + [k^2 - \frac{l(l+1)}{r^2}](rR(r)) \;\; = \;\; 0, \tag{2.30}$$

$$\frac{1}{\sin\theta}\frac{\mathrm{d}}{\mathrm{d}\theta}(\sin\theta\frac{\mathrm{d}P(\theta)}{\mathrm{d}\theta}) + [l(l+1) - \frac{m^2}{\sin^2\theta}]P(\theta) = 0, \quad (2.31)$$

$$\frac{\mathrm{d}^2Q(\phi)}{\mathrm{d}\phi^2} + m^2Q(\phi) = 0. \quad (2.32)$$

The solution of the azimuthal part $Q(\phi)$ could be either $\sin(m\phi)$ or $\cos(m\phi)$, where m are integers. Then we may write $Q(\phi)$ as a linear combination of these two solutions, that is:

$$Q(\phi) = A\cos(m\phi) + B\cos(m\phi) \qquad m = 0, \pm1, \pm2, \pm3, \ldots. \quad (2.33)$$

The solutions of Eq. (2.31) for a given m are the associated Lengendre polynomial, $P_l^m(\cos\theta)$, where $l = 0, 1, 2, 3, \ldots$. The important properties of $P_l^m(\cos\theta)$ are given in the Appendix $(A.3)$. For the radial part, the Eq. (2.30) is known as the spherical Bessel function. The solutions of Eq. (2.30) is the spherical Hankel function of the first kind, $h_l^{(1)}$:

$$R(r) = h_l^{(1)}(kr), \quad (2.34)$$

which behaves as the outgoing wave in asymptotic form, $h_l^{(1)}$ can be expanded as $h_l^{(1)}(kr) \approx (-1)^{l+1}\frac{e^{ikr}}{kr}$.

Now, the full solution of E_r has been derived and can be written as a linear combination of all l and m. Here we have introduced the complex scattering coefficient $\tilde{a}_{lm}$:

$$E_r(r,\theta,\phi) = \sum_{l,m}\tilde{a}_{lm}\frac{h_l^{(1)}(kr)}{r}P_l^m(\cos\theta)Q_m(\phi). \quad (2.35)$$

The remaining components of the electric and magnetic fields in TM mode are derived from the differential equations obtained by equating components of unit vectors in the LHS and the RHS of Eq. (2.26) and Eq. (2.27) from Maxwell equations so that six equations are formulated. Then, the differential equation of each remaining component can be written in term of the known E_r by normal elimination method given in the Appendix $(A.2)$. These differential equations for E_θ, E_ϕ, B_θ and B_ϕ are given by:

$$\frac{\partial^2}{\partial r^2}(rE_\theta) + k^2(rE_\theta) = \frac{\partial^2 E_r}{\partial r\partial\theta}, \quad (2.36)$$

$$\frac{\partial^2}{\partial r^2}(rE_\phi) + k^2(rE_\phi) = \frac{1}{\sin\theta}\frac{\partial^2 E_r}{\partial r \partial \phi}, \tag{2.37}$$

$$\frac{\partial^2}{\partial r^2}(rB_\theta) + k^2(rB_\theta) = -\frac{i\varepsilon k_0}{c}\frac{1}{\sin\theta}\frac{\partial E_r}{\partial \phi}, \tag{2.38}$$

$$\frac{\partial^2}{\partial r^2}(rB_\phi) + k^2(rB_\phi) = \frac{i\varepsilon k_0}{c}\frac{\partial E_r}{\partial \theta}. \tag{2.39}$$

The Eqs. (2.36)-(2.39) have the same functional form in the LHS but different functions in the RHS. Next, the solution of E_θ for each l and m will be shown as an example because solutions of another components are obtained by similar way.

The solution of E_θ in TM mode is obtained by substituting the E_r for each l and m from Eq. (2.29) into Eq. (2.36), then we have that :

$$\frac{\partial^2}{\partial r^2}(rE_\theta) + k^2(rE_\theta) = \tilde{a}_{lm}\frac{\mathrm{d}}{\mathrm{d}r}\Big[\frac{h_l^{(1)}(kr)}{r}\Big]\frac{\mathrm{d}P_l^m(\cos\theta)}{\mathrm{d}\theta}Q_m(\phi). \tag{2.40}$$

Eq. (2.40) shows that E_θ has the angular part proportional to $\frac{\mathrm{d}P_l^m(\cos\theta)}{\mathrm{d}\theta}Q_m(\phi)$, and the radial part is in term of $h_l^{(1)}(kr)$. This means that it is also separable, thus we may assume that $E_\theta = \frac{1}{r}\frac{\mathrm{d}}{\mathrm{d}r}[rK_l(r)]\frac{\mathrm{d}P_l^m(\cos\theta)}{\mathrm{d}\theta}Q_m(\phi)$ where $K_l(r)$ is a radial function to be determined. By substituting this assumed solution of E_θ into Eq. (2.40) and employing the linearly independent property of $P_l^m(\cos\theta)$, the differential equation of $K_l(r)$ can be obtained as :

$$\frac{\mathrm{d}^2}{\mathrm{d}r^2}[rK_l(r)] + rK_l(r) = \tilde{a}_{lm}\frac{h_l^{(1)}(kr)}{r}. \tag{2.41}$$

Since $h_l^{(1)}(kr)$ is in Eq. (2.30), the $\frac{h_l^{(1)}(kr)}{r}$ satisfies :

$$\frac{h_l^{(1)}(kr)}{r} = \frac{1}{l(l+1)}\frac{\mathrm{d}^2}{\mathrm{d}r^2}[rh_l^{(1)}(kr)] + \frac{k^2}{l(l+1)}rh_l^{(1)}(kr). \tag{2.42}$$

By substituting Eq. (2.42) to Eq. (2.41) and comparing two sides of the equation, the solution of $K_l(r)$ is expressed by :

$$rK_l(r) = \frac{\tilde{a}_{lm}}{l(l+1)}rh_l^{(1)}(kr). \tag{2.43}$$

The solution of E_θ is written as a linear combination of all l and m :

$$E_\theta = \sum_{l,m} \frac{\tilde{a}_{lm}}{l(l+1)} \frac{1}{r} \frac{\mathrm{d}}{\mathrm{d}r}[r h_l^{(1)}(kr)] \frac{\mathrm{d}P_l^m(\cos\theta)}{\mathrm{d}\theta} Q_m(\phi) \ , \ (l = 0, 1, 2, ..., |m| \leq l) \, . \quad (2.44)$$

For convenience, we define a new radial function namely $\zeta_l(kr)$ as $\zeta_l(kr) = kr h_l^{(1)}(kr)$, and $\zeta_l^{'}(kr)$ as the derivative with respect to its argument. Finally, the solution of E_θ becomes

$$E_\theta = \sum_{l,m} \frac{\tilde{a}_{lm}}{l(l+1)} \frac{\zeta_l^{'}(kr)}{r} \frac{\mathrm{d}P_l^m(\cos\theta)}{\mathrm{d}\theta} Q_m(\phi). \quad (2.45)$$

The solutions of E_ϕ , B_θ and B_ϕ in TM mode are obtained by the similar way as E_θ by solving Eq. (2.37), Eq. (2.38) and Eq. (2.39), respectively. These solutions are summarized as follows :

$$E_\phi = \sum_{l,m} \frac{\tilde{a}_{lm}}{l(l+1)} \frac{\zeta_l^{'}(kr)}{r} \frac{P_l^m(\cos\theta)}{\sin\theta} \frac{\mathrm{d}Q_m(\phi)}{\mathrm{d}\phi}, \quad (2.46)$$

$$B_\theta = -\frac{ik^2}{\omega} \sum_{l,m} \frac{\tilde{a}_{lm}}{l(l+1)} h_l^{(1)}(kr) \frac{P_l^m(\cos\theta)}{\sin\theta} \frac{\mathrm{d}Q_m(\phi)}{\mathrm{d}\phi}, \quad (2.47)$$

$$B_\phi = \frac{ik^2}{\omega} \sum_{l,m} \frac{\tilde{a}_{lm}}{l(l+1)} h_l^{(1)}(kr) \frac{\mathrm{d}P_l^m(\cos\theta)}{\mathrm{d}\theta} Q_m(\phi). \quad (2.48)$$

TE mode of the scattered wave

The electric and magnetic field in TE mode in the region outside the metallic sphere are obtained in the similar way as TM mode by starting from the derivation of the radial part of the magnetic field B_r. The remaining components of the magnetic field, B_θ and B_ϕ, and the electric field are obtained by solving the differential equations whose are written in term of known B_r. These differential equations are obtained from the Maxwell equations with the requirement that $E_r = 0$ in TE mode. The differential equation of B_r is acquired from the vector Helmholtz equation in Eq. (2.28), thus it takes the same from as E_r written in Eq. (2.29). B_r must also behave as an outgoing wave at asymptotic as required for the radiation wave. Therefore, the solution of B_r has the same angular and radial parts as E_r but with different amplitude. Here,

we define the complex amplitude of B_r in TE mode for each l as $\tilde{b}_{lm}$. Then, B_r is expressed as :

$$B_r(r,\theta,\phi) = \sum_{l,m} \tilde{b}_{lm} \frac{h_l^{(1)}(kr)}{r} P_l^m(\cos\theta) Q_m(\phi). \tag{2.49}$$

Next, the differential equations of B_θ, B_ϕ, E_θ and E_ϕ written in term of B_r are acquired by the simple elimination method of six equations obtained from Eq. (2.26) and Eq. (2.27) using the linearly independent property of the unit vectors in the spherical coordinate. The differential equation of B_θ in TE mode has exactly the same form as that of E_θ in TM mode, and the differential equation of B_ϕ in TE mode has exactly the same form as that of E_ϕ in TM mode. Therefore, the solutions of B_θ and B_ϕ in TE mode have the same form as Eq. (2.45) and Eq. (2.48), respectively, but with the amplitude $\tilde{b}_{lm}$:

$$B_\theta = \sum_{l,m} \frac{\tilde{b}_{lm}}{l(l+1)} \frac{\zeta_l'(kr)}{r} \frac{\mathrm{d}P_l^m(\cos\theta)}{\mathrm{d}\theta} Q_m(\phi), \tag{2.50}$$

$$B_\phi = \sum_{l,m} \frac{\tilde{b}_{lm}}{l(l+1)} \frac{\zeta_l'(kr)}{r} \frac{P_l^m(\cos\theta)}{\sin\theta} \frac{\mathrm{d}Q_m(\phi)}{\mathrm{d}\phi}. \tag{2.51}$$

However, the RHS of the differential equations of E_θ and E_ϕ in TE mode are different with those of B_θ and B_ϕ in TM mode, respectively. The steps of deriving these two solutions in TE mode are the same as those of E_θ in TM mode as shown as an example, which are : (1) substituting the solution of B_r in Eq. (2.49) to the differential equations of E_θ and E_ϕ, (2) writing E_θ and E_ϕ as separable solutions with the same angular part but different radial part as the RHS of the differential equations, (3) recalling the linearly independent of $P_l^m(\cos\theta)$ and the spherical Bessel equation and finally (4) comparing two sides of the equations to determine the radial part. By following these steps, the solutions of E_θ and E_ϕ in TE mode can be written as follow :

$$E_\theta = i\omega \sum_{l,m} \frac{\tilde{b}_{lm}}{l(l+1)} h_l^{(1)}(kr) \frac{P_l^m(\cos\theta)}{\sin\theta} \frac{\mathrm{d}Q_m(\phi)}{\mathrm{d}\phi}, \tag{2.52}$$

$$E_\phi = -i\omega \sum_{l,m} \frac{\tilde{b}_{lm}}{l(l+1)} h_l^{(1)}(kr) \frac{\mathrm{d}P_l^m(\cos\theta)}{\mathrm{d}\theta} Q_m(\phi). \tag{2.53}$$

Finally, we have derived the general solutions of the electric and magnetic field which are the sum of TM and TE modes in the region outside the metallic sphere. However, the complex coefficients $\tilde{a}_l$ and $\tilde{b}_l$ whose are defined as the coefficients of TM and TE modes have not been known yet. The boundary conditions at the surface of the metallic sphere must be used to find these coefficients. Therefore, we need to know the electromagnetic field inside the metallic sphere called the internal field at the surface. The solution of the internal field is explained in the next section.

2.3.2 Solution of the internal field

The first three equations of Maxwell's equations inside the metallic sphere are the same as Eqs. (2.24)-(2.26). However, the Ampere and Maxwell's law must include the current density $\boldsymbol{J}$ flowing inside the metallic sphere. Thus, the fourth equation of the Maxwell's equations now becomes

$$\nabla \times \boldsymbol{B} = \mu_0 \boldsymbol{J} - i\varepsilon \frac{k_0}{c} \boldsymbol{E}, \tag{2.54}$$

where μ_0 is the permeability of free space, ε is real dielectric constant, k_0 is wavenumber in free space and c is the speed of light in free space. We assume that the metallic sphere is the Ohmic material, that is, $\boldsymbol{J} = \sigma \boldsymbol{E}$ where σ is the conductivity. Therefore, two terms in the RHS of Eq. (2.54) can be grouped together. Then, Eq. (2.54) becomes

$$\nabla \times \boldsymbol{B} = -\frac{ik_0}{c}(\varepsilon + \frac{i\sigma}{\varepsilon_0 \omega}) \boldsymbol{E}. \tag{2.55}$$

The term $\varepsilon + \frac{i\sigma}{\varepsilon_0 \omega}$ is replaced by the complex dielectric constant $\tilde{\varepsilon}$ to make Eq. (2.55) to have the same from as Eq. (2.27). This approach is commonly found in solid state physics as is known as optical conductivity. The metallic sphere becomes dispersive due to the complex dielectric constant $\tilde{\varepsilon}$. Finally, the Ampere and Maxwell's law of

the internal field is obtained as :

$$\nabla \times \boldsymbol{B} = -\frac{ik_0}{c}\tilde{\varepsilon}\boldsymbol{E}. \tag{2.56}$$

From Eq. (2.24)-Eq. (2.26) and Eq. (2.56), the vector Helmholtz equations of the electric and magnetic fields can be obtained, and the complex wavenumber $\tilde{k}$ is defined as $\tilde{k} = k_0\sqrt{\varepsilon}$:

$$(\nabla^2 + \tilde{k}^2)\boldsymbol{E} = 0 \quad , \quad (\nabla^2 + \tilde{k}^2)\boldsymbol{B} = 0. \tag{2.57}$$

Obviously, the vector equations of the internal field have the same from as the scattered wave. The difference between Eq. (2.28) and Eq. (2.57) is only the wavenumber. The solution of the internal field is divided into TM mode in which $E_r \neq 0$ but $B_r = 0$, and TE mode in which $B_r \neq 0$ but $E_r = 0$, as the same as the scattered wave. The general solution of the internal field is the sum of these two modes.

TM mode of the internal field

In TM mode ($E_r \neq 0, B_r = 0$), we firstly find the solution of the radial part of the electric field E_r. The remaining components of the electric field and other components of the magnetic field can be derived from E_r. The differential equation of the internal E_r is in the same form as Eq. (2.29) except for the wavenumber which becomes complex for the internal field. Using the separation of variable, the function of the angular part becomes the product of the associated Legendre polynomial $P_l^m(\cos\theta)$ and $Q_m(\phi)$ as expressed in Eq. (2.33). The solution of the radial function $R(r)$ is obtained from the spherical Bessel function :

$$\frac{\mathrm{d}^2}{\mathrm{d}r^2}(rR(r)) + [\tilde{k}^2 - \frac{l(l+1)}{r^2}](rR(r)) = 0. \tag{2.58}$$

The requirement for the internal field is that it must be finite at the center of the metallic sphere which is defined as the origin of the system. Thus, only the spherical Bessel function $j_l(\tilde{k}r)$ satisfy this condition because the approximation from of $j_l(\tilde{k}r)$ with small argument is that $j_l(\tilde{k}r) \approx \frac{(\tilde{k}r)^l}{1\cdot 3\cdot 5\cdots(2l+1)}$ which is finite at the origin. Therefore,

the solution of E_r has been found, and the complex amplitude of the internal field in TM mode is defined as $\tilde{d}_{lm}$:

$$E_r(r,\theta,\phi) = \sum_{l,m} \tilde{d}_{lm} \frac{j_l(\tilde{k}r)}{r} P_l^m(\cos\theta) Q_m(\phi). \tag{2.59}$$

It can be seen that the differences between E_r of the scattered wave in Eq. (2.35) and E_r of the internal field in Eq. (2.59) are merely the complex coefficient and the radial function. Therefore, the remaining components of the electric field, E_θ and E_ϕ, and the magnetic field, B_θ and B_ϕ, of the internal field are obtained by replacing the complex coefficient $\tilde{a}_{lm}$ of the scattered wave by $\tilde{d}_{lm}$, and the spherical Hankel function $h_l^{(1)}(kr)$ of the scattered wave by the spherical Bessel function $j_l(\tilde{k}r)$, because the differential equations of the remaining components of the internal field are the same as those of the scattered wave. We define a new radial function namely $\psi_l(\tilde{k}r) = kr j_l(\tilde{k}r)$, and $\psi_l'(\tilde{k}r)$ is the derivative of $\psi_l(\tilde{k}r)$ with respect to its argument. Therefore, these remaining solutions of the internal electric and magnetic field are expressed as

$$E_\theta = \sum_{l,m} \frac{\tilde{d}_{lm}}{l(l+1)} \frac{\psi_l{}'(\tilde{k}r)}{r} \frac{\mathrm{d}P_l^m(\cos\theta)}{\mathrm{d}\theta} Q_m(\phi), \tag{2.60}$$

$$E_\phi = \sum_{l,m} \frac{\tilde{d}_{lm}}{l(l+1)} \frac{\psi_l{}'(\tilde{k}r)}{r} \frac{P_l^m(\cos\theta)}{\sin\theta} \frac{\mathrm{d}Q_m(\phi)}{\mathrm{d}\phi}, \tag{2.61}$$

$$B_\theta = -\frac{i\tilde{k}^2}{\omega} \sum_{l,m} \frac{\tilde{d}_{lm}}{l(l+1)} j_l(\tilde{k}r) \frac{P_l^m(\cos\theta)}{\sin\theta} \frac{\mathrm{d}Q_m(\phi)}{\mathrm{d}\phi}, \tag{2.62}$$

$$B_\phi = \frac{i\tilde{k}^2}{\omega} \sum_{l,m} \frac{\tilde{d}_{lm}}{l(l+1)} j_l'(\tilde{k}r) \frac{\mathrm{d}P_l^m(\cos\theta)}{\mathrm{d}\theta} Q_m(\phi). \tag{2.63}$$

These solutions will be used when we consider the boundary condition to find the complex coefficients of the scattered wave and also the internal field.

TE mode of the internal field

In TE mode ($B_r \neq 0, E_r = 0$), we firstly find the solution of the radial part of the internal magnetic field B_r. From this solution, we can obtain the remaining components of the internal magnetic field and also the solution of the internal electric field. The differential equation of the internal B_r is in the same form as that of the internal E_r in TM mode. Therefore, the solution of the internal B_r has the same radial and angular functional forms as the internal E_r but with different complex coefficient. Here, we define the complex coefficient of the internal field in TE mode as $\tilde{c}_{lm}$. Thus, the solution of internal B_r is expressed as :

$$B_r(r,\theta,\phi) = \sum_{l,m} \tilde{c}_{lm} \frac{j_l(\tilde{k}r)}{r} P_l^m(\cos\theta) Q_m(\phi). \tag{2.64}$$

The remaining components of the internal magnetic field and the internal electric field in TE mode are obtained by replacing the coefficient b_{lm}, $h_l^{(1)}(kr)$, $\zeta_l(kr)$ and $\zeta_l^{'}(kr)$ of the scattered wave in TE mode by c_{lm}, $j_l(\tilde{k}r)$, $\psi_l(\tilde{k}r)$ and $\psi_l^{'}(\tilde{k}r)$, respectively. Then, these solutions are expressed as :

$$B_\theta = \sum_{l,m} \frac{\tilde{c}_{lm}}{l(l+1)} \frac{\psi_l^{'}(\tilde{k}r)}{r} \frac{\mathrm{d}P_l^m(\cos\theta)}{\mathrm{d}\theta} Q_m(\phi), \tag{2.65}$$

$$B_\phi = \sum_{l,m} \frac{\tilde{c}_{lm}}{l(l+1)} \frac{\psi_l^{'}(\tilde{k}r)}{r} \frac{P_l^m(\cos\theta)}{\sin\theta} \frac{\mathrm{d}Q_m(\phi)}{\mathrm{d}\phi}, \tag{2.66}$$

$$E_\theta = i\omega \sum_{l,m} \frac{\tilde{c}_{lm}}{l(l+1)} j_l(\tilde{k}r) \frac{P_l^m(\cos\theta)}{\sin\theta} \frac{\mathrm{d}Q_m(\phi)}{\mathrm{d}\phi}, \tag{2.67}$$

$$E_\phi = -i\omega \sum_{l,m} \frac{\tilde{c}_{lm}}{l(l+1)} j_l(\tilde{k}r) \frac{\mathrm{d}P_l^m(\cos\theta)}{\mathrm{d}\theta} Q_m(\phi). \tag{2.68}$$

In the next section will give the formulae of all defined complex coefficients using the boundary condition of the electromagnetic field at the surface of the metallic sphere.

2.3.3 Coefficients of the scattered wave and the internal field

In this section, we show the derivation of the coefficients of the scattered wave and the internal field from the boundary conditions for electric and magnetic fields at the surface of the metallic sphere.

Expansion of the incident light

In spectroscopy measurement, laser light is utilized as an excitation source. Hereafter, laser light is called an incident light. We consider the incident light propagating in form of plane wave. The direction of propagation is defined as z-axis, and the incident electric field is polarized along x-axis, in the cartesian coordinate. Thus, the electric and magnetic fields propagating in the non-absorbing dielectric with the dieletric constant ε can be expressed as follow where the right superscript "i" is used to label the incident light :

$$\boldsymbol{E}^{\mathrm{i}} = E_0 \hat{\boldsymbol{e}}_x e^{ikz} \quad , \quad \boldsymbol{B}^{\mathrm{i}} = \frac{k}{\omega} E_0 \hat{\boldsymbol{e}}_y e^{ikz}, \tag{2.69}$$

where k is the wavenumber of the incident light in the dielectric medium, ω is the angular frequency of the incident light, and E_0 is the amplitude of the incident electric field which is related to the intensity of the incident light I as $E_0 = \sqrt{\frac{I}{\varepsilon_0 c}}$, where ε_0 is the permittivity of the free space and c is the velocity of light in free space. $\boldsymbol{E}^{\mathrm{i}}$ and $\boldsymbol{B}^{\mathrm{i}}$ can be expanded in term of the spherical wave. The concept of TM mode and TE mode is also applied to the incident light as it is applied to the scattered wave in the region outside of the metallic sphere. Thus, once E_r^{i} has been expanded, the remaining components of the electric and magnetic fields are obtained simply by comparing the E_r^{i} with E_r^{s} for the scattered wave in both TM and TE modes.

Let's us firstly try to expand E_r^{i} to find the expansion of the incident light in TM mode ($E_r^{\mathrm{i}} \neq 0, B_r^{\mathrm{i}} = 0$). E_r^{i} can be written in the spherical coordinate as :

$$E_r^{\mathrm{i}} = E_0 \sin\theta \cos\phi e^{ikr\cos\theta} = -\frac{E_0}{ikr} \cos\phi \frac{\partial}{\partial\theta}\Big(e^{ikr\cos\theta}\Big). \tag{2.70}$$

It can be seen that the azimuthal part has only one component that is $m = 1$, and it

is cosine function, that is, $Q_1(\phi) = \cos\phi$. The exponential term can be expanded in term of the spherical Bessel function $j_l(kr)$ and the Legendre polynomial $P_l(\cos\theta)$ as :

$$e^{ikr\cos\theta} = \sum_l (2l+1) i^l j_l(kr) P_l(\cos\theta). \tag{2.71}$$

By substituting Eq. (2.71) into Eq. (2.70) and recalling the relation of the Legendre polynomial and the associated Legendre polynomial, $\frac{\mathrm{d}P_l}{\mathrm{d}\theta} = -P_l^1(\cos\theta)$, the expanded E_r^{i} becomes :

$$E_r^{\mathrm{i}} = E_0 \sum_l (2l+1) i^{l-1} \frac{j_l(kr)}{kr} P_l^1(\cos\theta)\cos\phi. \tag{2.72}$$

By comparing Eq. (2.72) with Eq. (2.35), the remaining components of the electric and magnetic fields in TM mode are acquired from those of the scattered wave in TM mode simply by replacing the complex coefficients $\tilde{a}_{lm}$ by $E_0(2l+1)i^{l-1}$, replacing the radial spherical Hankel function of the first kind $h_l^{(1)}(kr)/r$ by the spherical Bessel function $j_l(kr)/kr$, and replacing $Q_m(\phi)$ by $\cos\phi$. Then, these expanded remaining components of the incident electric and magnetic fields in TM mode are expressed as :

$$E_\theta^{\mathrm{i}} = E_0 \sum_l \frac{(2l+1)i^{l-1}}{l(l+1)} \frac{\psi_l'(kr)}{kr} \frac{\mathrm{d}P_l^1(\cos\theta)}{\mathrm{d}\theta} \cos\phi, \tag{2.73}$$

$$E_\phi^{\mathrm{i}} = -E_0 \sum_l \frac{(2l+1)i^{l-1}}{l(l+1)} \frac{\psi_l'(kr)}{kr} \frac{P_l^1(\cos\theta)}{\sin\theta} \sin\phi, \tag{2.74}$$

$$B_\theta^{\mathrm{i}} = E_0 \frac{k}{\omega} \sum_l \frac{(2l+1)i^l}{l(l+1)} j_l(kr) \frac{P_l^m(\cos\theta)}{\sin\theta} \sin\phi, \tag{2.75}$$

$$B_\phi^{\mathrm{i}} = E_0 \frac{k}{\omega} \sum_l \frac{(2l+1)i^l}{l(l+1)} j_l(kr) \frac{\mathrm{d}P_l^m(\cos\theta)}{\mathrm{d}\theta} \cos\phi. \tag{2.76}$$

where a is defined as the radius of the metallic sphere.

Next, we show the expansion of the incident light in TE mode ($B_r^{\mathrm{i}} \neq 0, E_r^{\mathrm{i}} = 0$). We want to expand B_r^{i} in the spherical coordinate. Then, B_r^{i} obtained from Eq. (2.69) is expressed as :

$$B_r^{\mathrm{i}} = E_0 \frac{k}{\omega} \sin\theta \sin\phi e^{ikr\cos\theta} = E_0 \frac{k}{\omega} \Big(-\frac{1}{ikr} \Big) \sin\theta \frac{\partial}{\partial\theta} \Big(e^{ikr\cos\theta} \Big). \tag{2.77}$$

By substituting Eq. (2.71) into Eq. (2.77) and recalling the identity $\frac{\mathrm{d}P_l}{\mathrm{d}\theta} = -P_l^1(\cos\theta)$, the expanded B_r^{i} can be written as :

$$B_r^{\mathrm{i}} = E_0 \frac{k}{\omega} \sum_l (2l+1) i^{l-1} \frac{j_l(kr)}{kr} P_l^1(\cos\theta) \sin\phi.. \tag{2.78}$$

It can be seen that the azimuthal part is sine function with $m = 1$, that is, $Q_1(\phi) = \sin\phi$. Therefore, phase difference in the azimuthal part of the incident electric and magnetic fields is $\pi/2$. By comparing Eq. (2.78) with Eq. (2.49), the remaining components of the magnetic and electric fields in TE mode are acquired from those of the scattered wave in TE mode simply by replacing the complex coefficients $\tilde{b}_{lm}$ by $E_0 \frac{k}{\omega}(2l+1)i^{l-1}$, replacing the radial function $h_l^{(1)}(kr)/r$ by the spherical Bessel function $j_l(kr)/kr$, and replacing $Q_m(\phi)$ by $\sin\phi$. Then, these expanded remaining components of the incident magnetic and electric fields are expressed as :

$$B_\theta^{\mathrm{i}} = E_0 \frac{k}{\omega} \sum_l \frac{(2l+1)i^{l-1}}{l(l+1)} \frac{\psi_l'(kr)}{kr} \frac{\mathrm{d}P_l^m(\cos\theta)}{\mathrm{d}\theta} \sin\phi, \tag{2.79}$$

$$B_\phi^{\mathrm{i}} = E_0 \frac{k}{\omega} \sum_l \frac{(2l+1)i^{l-1}}{l(l+1)} \frac{\psi_l'(kr)}{kr} \frac{P_l^m(\cos\theta)}{\sin\theta} \cos\phi, \tag{2.80}$$

$$E_\theta^{\mathrm{i}} = E_0 \sum_l \frac{(2l+1)i^{l}}{l(l+1)} j_l(kr) \frac{P_l^m(\cos\theta)}{\sin\theta} \cos\phi, \tag{2.81}$$

$$E_\phi^{\mathrm{i}} = -E_0 \sum_l \frac{(2l+1)i^{l}}{l(l+1)} j_l(kr) \frac{\mathrm{d}P_l^m(\cos\theta)}{\mathrm{d}\theta} \sin\theta. \tag{2.82}$$

Coefficients of the scattered wave and the internal field

The continuities of the tangential components of the electric and magnetic fields at the surface of the metallic sphere are applied to obtain the coefficients of the scattered wave and the internal field. The electromagnetic field outside the metallic sphere is the sum of the incident light and the scattered wave, while the internal field is inside the metallic sphere. The general solution of the electromagnetic field is the summation of TM mode and TE mode, then these two mode are needed to be marked. The TM mode and TE mode are denoted by the left superscript "tm" and "te", respectively. Thus, the boundary conditions of the tangential component of the

electric and magnetic field at the surface of the metallic sphere are expressed as :

$$({}^{\mathrm{tm}}E_{\theta}^{\mathrm{i}} + {}^{\mathrm{te}}E_{\theta}^{\mathrm{i}})_{(r=a)} + ({}^{\mathrm{tm}}E_{\theta}^{\mathrm{s}} + {}^{\mathrm{te}}E_{\theta}^{\mathrm{s}})_{(r=a)} = ({}^{\mathrm{tm}}E_{\theta}^{\mathrm{t}} + {}^{\mathrm{te}}E_{\theta}^{\mathrm{t}})_{(r=a)} \tag{2.83}$$

$$({}^{\mathrm{tm}}E_{\phi}^{\mathrm{i}} + {}^{\mathrm{te}}E_{\phi}^{\mathrm{i}})_{(r=a)} + ({}^{\mathrm{tm}}E_{\phi}^{\mathrm{s}} + {}^{\mathrm{te}}E_{\phi}^{\mathrm{s}})_{(r=a)} = ({}^{\mathrm{tm}}E_{\phi}^{\mathrm{t}} + {}^{\mathrm{te}}E_{\phi}^{\mathrm{t}})_{(r=a)} \tag{2.84}$$

$$({}^{\mathrm{tm}}B_{\theta}^{\mathrm{i}} + {}^{\mathrm{te}}B_{\theta}^{\mathrm{i}})_{(r=a)} + ({}^{\mathrm{tm}}B_{\theta}^{\mathrm{s}} + {}^{\mathrm{te}}B_{\theta}^{\mathrm{s}})_{(r=a)} = ({}^{\mathrm{tm}}B_{\theta}^{\mathrm{t}} + {}^{\mathrm{te}}B_{\theta}^{\mathrm{t}})_{(r=a)} \tag{2.85}$$

$$({}^{\mathrm{tm}}B_{\phi}^{\mathrm{i}} + {}^{\mathrm{te}}B_{\phi}^{\mathrm{i}})_{(r=a)} + ({}^{\mathrm{tm}}B_{\phi}^{\mathrm{s}} + {}^{\mathrm{te}}B_{\phi}^{\mathrm{s}})_{(r=a)} = ({}^{\mathrm{tm}}B_{\phi}^{\mathrm{t}} + {}^{\mathrm{te}}B_{\phi}^{\mathrm{t}})_{(r=a)} \tag{2.86}$$

The first step is finding the coupled equations of these coefficients from Eq. (2.83) to Eq. (2.86). Two coupled equations are acquired from a pair of boundary conditions for E_θ and E_ϕ, and the other two coupled equations are obtained from a pair of boundary conditions for B_θ and B_ϕ. Then, the four coupled equations are sufficient to be solved for the coefficients of the scattered wave and the internal field in both TM and TE modes. E_θ^{i} in TM mode and TE mode are written in Eqs. (2.73) and (2.81), respectively. The E_θ^{S} in TM mode and TE modes are written in Eqs. (2.45) and (2.52), respectively, and E_θ^{t} in TM mode and TE mode are shown in Eqs. (2.60) and (2.67), respectively. All of these equations are substituted into Eq. (2.87), and then the terms with the same angular dependence are grouped together so that the integral identities of the associated Legendre polynomial in Appendix Eqs. $(A.27) - (A.28)$ can be later applied. After substituting and grouping as mentioned, the Eq. (2.87) becomes :

$$\begin{aligned} 0 \;=\; & \sum_{l=1}^{\infty} \Big[E_0 \frac{(2l+1)i^{l-1}}{l(l+1)} \frac{\psi_l'(x)}{x} + \frac{\tilde{a}_{l1}}{l(l+1)} \frac{\zeta_l'(x)}{a} - \frac{\tilde{d}_{l1}}{l(l+1)} \frac{\psi_l'(mx)}{a} \Big] \frac{\mathrm{d}P_l^1(\cos\theta)}{\mathrm{d}\theta} + \\ & \sum_{l=1}^{\infty} \Big[E_0 \frac{(2l+1)i^{l}}{l(l+1)} j_l(x) + \frac{i\omega\tilde{b}_{l1}}{l(l+1)} h_l^{(1)}(x) - \frac{i\omega\tilde{c}_{l1}}{l(l+1)} j_l(mx) \Big] \frac{P_l^1(\cos\theta)}{\sin\theta}. \end{aligned} \tag{2.87}$$

For the boundary condition of E_ϕ, the expansion of E_ϕ^{i} into TM mode and TE mode written in Eq. (2.74) and Eq. (2.81), respectively, the solutions of E_ϕ^{S} in TM mode and TE mode written in Eq. (2.46) and Eq. (2.53), respectively, and the solutions of E_ϕ^{t} in TM mode and TE mode written in Eq. (2.61) and Eq. (2.68), respectively, are substituted into Eq. (2.84). Then, by grouping the terms with the same

angular function together, Eq. (2.84) becomes :

$$0 = \sum_{l=1}^{\infty}\Big[E_0\frac{(2l+1)i^{l-1}}{l(l+1)}\frac{\psi_l^{'}(x)}{x}+\frac{\tilde{a}_{l1}}{l(l+1)}\frac{\zeta_l^{'}(x)}{a}-\frac{\tilde{d}_{l1}}{l(l+1)}\frac{\psi_l^{'}(mx)}{a}\Big]\frac{P_l^1(\cos\theta)}{\sin\theta}+$$
$$\sum_{l=1}^{\infty}\Big[E_0\frac{(2l+1)i^{l}}{l(l+1)}j_l(x)+\frac{i\omega\tilde{b}_{l1}}{l(l+1)}h_l^{(1)}(x)-\frac{i\omega\tilde{c}_{l1}}{l(l+1)}j_l(mx)\Big]\frac{\mathrm{d}P_l^1(\cos\theta)}{\mathrm{d}\theta}. \quad (2.88)$$

It can be seen that there are two angular functions, $\frac{P_l^1(\cos\theta)}{\sin\theta}$ and $\frac{\mathrm{d}P_l^1(\cos\theta)}{\mathrm{d}\theta}$, appearing in both Eq. (2.87) and Eq. (2.88). Furthermore, the l-dependence coefficient in front of the function $\frac{P_l^1(\cos\theta)}{\sin\theta}$ in Eq. (2.88) is the same as that one in front of the function $\frac{\mathrm{d}P_l^1(\cos\theta)}{\mathrm{d}\theta}$ in Eq. (2.87) and vice versa. By this observation, it allows us to use the integral identities $(A.27)$ and $(A.28)$ of the associated Legendre polynomial to derive two coupled equations of the coefficients of the scattered wave and the internal field. By applying the integral identities of the associated Legendre polynomial to Eqs. (2.87) and (2.88), the two linear coupled equations of the coefficients are obtained as :

$$\zeta_l^{'}(x)\tilde{a}_{l1}-\psi_l^{'}(mx)\tilde{d}_{l1} = -E_0a(2l+1)i^{l-1}\frac{\psi_l^{'}(x)}{x}, \quad (2.89)$$
$$h_l^{(1)}(x)\tilde{b}_{l1}-j_l(mx)\tilde{c}_{l1} = -E_0\frac{(2l+1)i^{l-1}}{\omega}j_l(x). \quad (2.90)$$

Similarly, from Eqs. (2.85) and (2.86), and the integral identities of the associated Legendre polynomial $(A.27)$ and $(A.28)$, the another two coupled equations of the coefficients of the scattered wave and the internal field are obtained as :

$$h_l^{(1)}\tilde{a}_{l1}-m^2j_l(mx)\tilde{d}_{l1} = -E_0\frac{(2l+1)i^{(l-1)}}{k}j_l(x), \quad (2.91)$$
$$\zeta_l^{'}(x)\tilde{b}_{l1}-\psi_l^{'}(mx)\tilde{c}_{l1} = -E_0\frac{(2l+1)i^{(l-1)}}{\omega}\psi_l^{'}(x). \quad (2.92)$$

Then, the coefficients of the scattered wave and the internal field in TM mode, a_{l1} and d_{l1}, respectively, are obtained by solving the linear equations (2.89) and (2.92). The linear Eqs. (2.90) and (2.92) are solved for the coefficients of the scattered wave and the internal field in TE mode, b_{l1} and c_{l1}, respectively. The solutions of all of

these coefficients are given as follows :

$$\tilde{a}_{l1} = -E_0\frac{(2l+1)i^{l-1}}{k}\Big[\frac{m\psi_l(mx)\psi_l^{'}(x)-\psi_l^{'}(mx)\psi_l(x)}{m\psi_l(mx)\zeta_l^{'}(x)-\psi_l^{'}(mx)\zeta_l(x)}\Big], \tag{2.93}$$

$$\tilde{d}_{l1} = E_0\frac{(2l+1)i^{l-1}}{\tilde{k}}\Big[\frac{m\psi_l(x)\zeta_l^{'}(x)-m\psi_l^{'}(x)\zeta_l(x)}{m\psi_l(mx)\zeta_l^{'}(x)-\psi_l^{'}(mx)\zeta_l(x)}\Big], \tag{2.94}$$

$$\tilde{b}_{l1} = -E_0\frac{(2l+1)i^{l-1}}{\omega}\Big[\frac{\psi_l(mx)\psi_l^{'}(x)-m\psi_l^{'}(mx)\psi_l(x)}{\psi_l(mx)\zeta_l^{'}(x)-m\psi_l^{'}(mx)\zeta_l(x)}\Big], \tag{2.95}$$

$$\tilde{c}_{l1} = E_0\frac{(2l+1)i^{l-1}}{\omega}\Big[\frac{m\psi_l(x)\zeta_l^{'}(x)-m\psi_l^{'}(x)\zeta_l(x)}{\psi_l(mx)\zeta_l^{'}(x)-m\psi_l^{'}(mx)\zeta_l(x)}\Big], \tag{2.96}$$

where $x = ka$.

The coefficients of the same mode have the same denominator, but these denominators are different between two modes. The resonance of the electromagnetic field occurs when the denominator becomes zero, thus the resonance conditions for each value of l are different between TM mode and TE mode. For TM mode, the resonance corresponds to the resonance of the electric multipole oscillation while the resonance of TE mode corresponds to the magnetic multipole oscillation.

The scattered electric and magnetic fields which are denoted by the right superscript "s" in TM mode are then obtained by substituting the scattering coefficients $\tilde{a}_{l1}$ written in Eq. (2.93) into Eq. (2.35) , and Eqs. (2.45)-(2.48). These solutions are expressed as follow :

$${}^{\rm tm}E_r^{\rm s} = -E_0\sum_{l=1}^{\infty}(2l+1)i^{l-1}\Big[\frac{m\psi_l(mx)\psi_l^{'}(x)-\psi_l^{'}(mx)\psi_l(x)}{m\psi_l(mx)\zeta_l^{'}(x)-\psi_l^{'}(mx)\zeta_l(x)}\Big]\frac{h_l^{(1)}(kr)}{kr}P_l^1(\cos\theta)\cos\phi, \tag{2.97}$$

$${}^{\rm tm}E_\theta^{\rm s} = -E_0\sum_{l=1}^{\infty}\frac{(2l+1)i^{l-1}}{l(l+1)}\Big[\frac{m\psi_l(mx)\psi_l^{'}(x)-\psi_l^{'}(mx)\psi_l(x)}{m\psi_l(mx)\zeta_l^{'}(x)-\psi_l^{'}(mx)\zeta_l(x)}\Big]\frac{\zeta_l^{'}(kr)}{kr}\frac{{\rm d}P_l^1(\cos\theta)}{{\rm d}\theta}\cos\phi, \tag{2.98}$$

$${}^{\rm tm}E_\phi^{\rm s} = E_0\sum_{l=1}^{\infty}\frac{(2l+1)i^{l-1}}{l(l+1)}\Big[\frac{m\psi_l(mx)\psi_l^{'}(x)-\psi_l^{'}(mx)\psi_l(x)}{m\psi_l(mx)\zeta_l^{'}(x)-\psi_l^{'}(mx)\zeta_l(x)}\Big]\frac{\zeta_l^{'}(kr)}{kr}\frac{P_l^1(\cos\theta)}{\sin\theta}\sin\phi, \tag{2.99}$$

$${}^{\rm tm}B_\theta^{\rm s} = -E_0\frac{k}{\omega}\sum_{l=1}^{\infty}\frac{(2l+1)i^{l}}{l(l+1)}\Big[\frac{m\psi_l(mx)\psi_l^{'}(x)-\psi_l^{'}(mx)\psi_l(x)}{m\psi_l(mx)\zeta_l^{'}(x)-\psi_l^{'}(mx)\zeta_l(x)}\Big]h_l^{(1)}(kr)\frac{P_l^1(\cos\theta)}{\sin\theta}\sin\phi, \tag{2.100}$$

$${}^{\rm tm}B_\phi^{\rm s} = -E_0\frac{k}{\omega}\sum_{l=1}^{\infty}\frac{(2l+1)i^{l}}{l(l+1)}\Big[\frac{m\psi_l(mx)\psi_l^{'}(x)-\psi_l^{'}(mx)\psi_l(x)}{m\psi_l(mx)\zeta_l^{'}(x)-\psi_l^{'}(mx)\zeta_l(x)}\Big]h_l^{(1)}(kr)\frac{{\rm d}P_l^1(\cos\theta)}{{\rm d}\theta}\cos\phi. \tag{2.101}$$

The scattered electric and magnetic fields in TE mode are obtained by substituting the scattering coefficient $\tilde{b}_{l1}$ written in Eq. (2.95) into Eq. (2.49), and Eqs. (2.50)-

(2.53). These solutions are then expressed as :

$$
\begin{aligned}
{}^{\mathrm{te}}B_r^{\mathrm{s}} &= -E_0\frac{k}{\omega}\sum_{l=1}^{\infty}(2l+1)i^{l-1}\left[\frac{\psi_l(mx)\psi_l^{'}(x)-m\psi_l^{'}(mx)\psi_l(x)}{\psi_l(mx)\zeta_l^{'}(x)-m\psi_l^{'}(mx)\zeta_l(x)}\right]\frac{h_l^{(1)}(kr)}{kr}P_l^1(\cos\theta)\sin\phi, && (2.102)\\
{}^{\mathrm{te}}B_\theta^{\mathrm{s}} &= -E_0\frac{k}{\omega}\sum_{l=1}^{\infty}\frac{(2l+1)i^{l-1}}{l(l+1)}\left[\frac{\psi_l(mx)\psi_l^{'}(x)-m\psi_l^{'}(mx)\psi_l(x)}{\psi_l(mx)\zeta_l^{'}(x)-m\psi_l^{'}(mx)\zeta_l(x)}\right]\frac{\zeta_l^{'}(kr)}{kr}\frac{\mathrm{d}P_l^1(\cos\theta)}{\mathrm{d}\theta}\sin\phi, && (2.103)\\
{}^{\mathrm{te}}B_\phi^{\mathrm{s}} &= -E_0\frac{k}{\omega}\sum_{l=1}^{\infty}\frac{(2l+1)i^{l-1}}{l(l+1)}\left[\frac{\psi_l(mx)\psi_l^{'}(x)-m\psi_l^{'}(mx)\psi_l(x)}{\psi_l(mx)\zeta_l^{'}(x)-m\psi_l^{'}(mx)\zeta_l(x)}\right]\frac{\zeta_l^{'}(kr)}{kr}\frac{P_l^1(\cos\theta)}{\sin\theta}\cos\phi, && (2.104)\\
{}^{\mathrm{te}}E_\theta^{\mathrm{s}} &= -E_0\sum_{l=1}^{\infty}\frac{(2l+1)i^{l}}{l(l+1)}\left[\frac{\psi_l(mx)\psi_l^{'}(x)-m\psi_l^{'}(mx)\psi_l(x)}{\psi_l(mx)\zeta_l^{'}(x)-m\psi_l^{'}(mx)\zeta_l(x)}\right]h_l^{(1)}(kr)\frac{P_l^1(\cos\theta)}{\sin\theta}\cos\phi, && (2.105)\\
{}^{\mathrm{te}}E_\phi^{\mathrm{s}} &= E_0\sum_{l=1}^{\infty}\frac{(2l+1)i^{l}}{l(l+1)}\left[\frac{\psi_l(mx)\psi_l^{'}(x)-m\psi_l^{'}(mx)\psi_l(x)}{\psi_l(mx)\zeta_l^{'}(x)-m\psi_l^{'}(mx)\zeta_l(x)}\right]h_l^{(1)}(kr)\frac{\mathrm{d}P_l^1(\cos\theta)}{\mathrm{d}\theta}\sin\phi. && (2.106)
\end{aligned}
$$

The internal electric and magnetic fields which are denoted by the right superscript "t" in TM are obtained by substituting the internal coefficient $\tilde{d}_{l1}$ written in Eq. (2.94) into Eq. (2.59), and Eqs. (2.60)-(2.63). Then, these solutions are expressed as :

$$
\begin{aligned}
{}^{\mathrm{tm}}E_r^{\mathrm{t}} &= E_0\sum_{l=1}^{\infty}(2l+1)i^{l-1}\left[\frac{m\psi_l(x)\zeta_l^{'}(x)-m\psi_l^{'}(x)\zeta_l(x)}{m\psi_l(mx)\zeta_l^{'}(x)-\psi_l^{'}(mx)\zeta_l(x)}\right]\frac{j_l(\tilde{k}r)}{\tilde{k}r}P_l^1(\cos\theta)\cos\phi, && (2.107)\\
{}^{\mathrm{tm}}E_\theta^{\mathrm{t}} &= E_0\sum_{l=1}^{\infty}\frac{(2l+1)i^{l-1}}{l(l+1)}\left[\frac{m\psi_l(x)\zeta_l^{'}(x)-m\psi_l^{'}(x)\zeta_l(x)}{m\psi_l(mx)\zeta_l^{'}(x)-\psi_l^{'}(mx)\zeta_l(x)}\right]\frac{\psi_l^{'}(\tilde{k}r)}{\tilde{k}r}\frac{\mathrm{d}P_l^1(\cos\theta)}{\mathrm{d}\theta}\cos\phi, && (2.108)\\
{}^{\mathrm{tm}}E_\phi^{\mathrm{t}} &= -E_0\sum_{l=1}^{\infty}\frac{(2l+1)i^{l-1}}{l(l+1)}\left[\frac{m\psi_l(x)\zeta_l^{'}(x)-m\psi_l^{'}(x)\zeta_l(x)}{m\psi_l(mx)\zeta_l^{'}(x)-\psi_l^{'}(mx)\zeta_l(x)}\right]\frac{\psi_l^{'}(\tilde{k}r)}{\tilde{k}r}\frac{P_l^1(\cos\theta)}{\sin\theta}\sin\phi, && (2.109)\\
{}^{\mathrm{tm}}B_\theta^{\mathrm{t}} &= E_0\frac{\tilde{k}}{\omega}\sum_{l=1}^{\infty}\frac{(2l+1)i^{l}}{l(l+1)}\left[\frac{m\psi_l(x)\zeta_l^{'}(x)-m\psi_l^{'}(x)\zeta_l(x)}{m\psi_l(mx)\zeta_l^{'}(x)-\psi_l^{'}(mx)\zeta_l(x)}\right]j_l(\tilde{k}r)\frac{P_l^1(\cos\theta)}{\sin\theta}\sin\phi, && (2.110)\\
{}^{\mathrm{tm}}B_\phi^{\mathrm{t}} &= E_0\frac{\tilde{k}}{\omega}\sum_{l=1}^{\infty}\frac{(2l+1)i^{l}}{l(l+1)}\left[\frac{m\psi_l(x)\zeta_l^{'}(x)-m\psi_l^{'}(x)\zeta_l(x)}{m\psi_l(mx)\zeta_l^{'}(x)-\psi_l^{'}(mx)\zeta_l(x)}\right]j_l(\tilde{k}r)\frac{\mathrm{d}P_l^1(\cos\theta)}{\mathrm{d}\theta}\cos\phi. && (2.111)
\end{aligned}
$$

Finally, the internal electric and magnetic fields in TE mode are obtained by substituting the internal coefficient $\tilde{c}_{l1}$ into Eq. (2.64), and Eqs. (2.65)-(2.68). Then, these solutions are expressed as :

$$
\begin{aligned}
{}^{\mathrm{te}}B_r^{\mathrm{t}} &= E_0\frac{\tilde{k}}{\omega}\sum_{l=1}^{\infty}(2l+1)i^{l-1}\left[\frac{m\psi_l(x)\zeta_l^{'}(x)-m\psi_l^{'}(x)\zeta_l(x)}{\psi_l(mx)\zeta_l^{'}(x)-m\psi_l^{'}(mx)\zeta_l(x)}\right]\frac{j_l(\tilde{k}r)}{\tilde{k}r}P_l^1(\cos\theta)\sin\phi, && (2.112)\\
{}^{\mathrm{te}}B_\theta^{\mathrm{t}} &= E_0\frac{\tilde{k}}{\omega}\sum_{l=1}^{\infty}\frac{(2l+1)i^{l-1}}{l(l+1)}\left[\frac{m\psi_l(x)\zeta_l^{'}(x)-m\psi_l^{'}(x)\zeta_l(x)}{\psi_l(mx)\zeta_l^{'}(x)-m\psi_l^{'}(mx)\zeta_l(x)}\right]\frac{\psi_l^{'}(\tilde{k}r)}{\tilde{k}r}\frac{\mathrm{d}P_l^1(\cos\theta)}{\mathrm{d}\theta}\sin\phi, && (2.113)
\end{aligned}
$$

$$
{}^{\mathrm{te}}B_{\phi}^{\mathrm{t}} = E_0 \frac{\tilde{k}}{\omega} \sum_{l=1}^{\infty} \frac{(2l+1)i^{l-1}}{l(l+1)} \left[\frac{m\psi_l(x)\zeta_l^{'}(x) - m\psi_l^{'}(x)\zeta_l(x)}{\psi_l(mx)\zeta_l^{'}(x) - m\psi_l^{'}(mx)\zeta_l(x)} \right] \frac{\psi_l^{'}(\tilde{k}r)}{\tilde{k}r} \frac{P_l^1(\cos\theta)}{\sin\theta} \cos\phi, \tag{2.114}
$$

$$
{}^{\mathrm{te}}E_{\theta}^{\mathrm{t}} = E_0 \sum_{l=1}^{\infty} \frac{(2l+1)i^{l}}{l(l+1)} \left[\frac{m\psi_l(x)\zeta_l^{'}(x) - m\psi_l^{'}(x)\zeta_l(x)}{\psi_l(mx)\zeta_l^{'}(x) - m\psi_l^{'}(mx)\zeta_l(x)} \right] j_l(\tilde{k}r) \frac{P_l^1(\cos\theta)}{\sin\theta} \cos\phi, \tag{2.115}
$$

$$
{}^{\mathrm{te}}E_{\phi}^{\mathrm{t}} = -E_0 \sum_{l=1}^{\infty} \frac{(2l+1)i^{l}}{l(l+1)} \left[\frac{m\psi_l(x)\zeta_l^{'}(x) - m\psi_l^{'}(x)\zeta_l(x)}{\psi_l(mx)\zeta_l^{'}(x) - m\psi_l^{'}(mx)\zeta_l(x)} \right] j_l(\tilde{k}r) \frac{\mathrm{d}P_l^1(\cos\theta)}{\mathrm{d}\theta} \sin\phi. \tag{2.116}
$$

2.4 Theory of Exciton in carbon nanotube

An exciton is a bounded electron-hole pair generated by the Coulomb interaction between photo-excited electron and hole [1]. At room temperature, an exciton in a carbon nanotube can be excited due to its one-dimensional property, but it is impossible for a bulk three-dimensional semiconductor to be excited due to the low binding energy of the exciton, about 10 meV. The exciton wavefunction is localized in real space and k space. In k space, the exciton wavefunction is a linear combination of Bloch wavefunctions so that the exciton has two kinds of wave vectors defined as : (i) the wave vector of the center of mass, $\boldsymbol{K} = (\boldsymbol{k}_c - \boldsymbol{k}_v)/2$ and (ii) the wave vector of the relative coordinate, $\boldsymbol{k} = \boldsymbol{k}_c + \boldsymbol{k}_v$, where $\boldsymbol{k}_c$ and $\boldsymbol{k}_v$ are, respectively, the wave vectors of the electron and hole in a single particle picture. It should be noted that the hole has an opposite sign for its wave vector and effective mass compared to the electron. $\boldsymbol{K}$ is a good quantum number and then the dispersion energy of the exciton is written as a function of $\boldsymbol{K}$ [7]. If we consider the optical transition along the tube axis, the vertical transition, that is, $\boldsymbol{k}_c = \boldsymbol{k}_v$, must be satisfied [3]. Thus, only $\boldsymbol{K} = 0$ exciton can recombine by emitting a photon which is called the "bright exciton", but $\boldsymbol{K} \neq 0$ exciton, the non-vertical transition, cannot recombine directly to emit a photon ,and then it is called "dark exciton" [7]. The spin of the exciton is defined as a total spin S which can be 0 and 1. The exciton spin $S = 0$ is called the "singlet exciton", and the exciton spin $S = 1$ is called the "triplet exciton". The triplet exciton is a dark exciton in term of dipole selection rule.

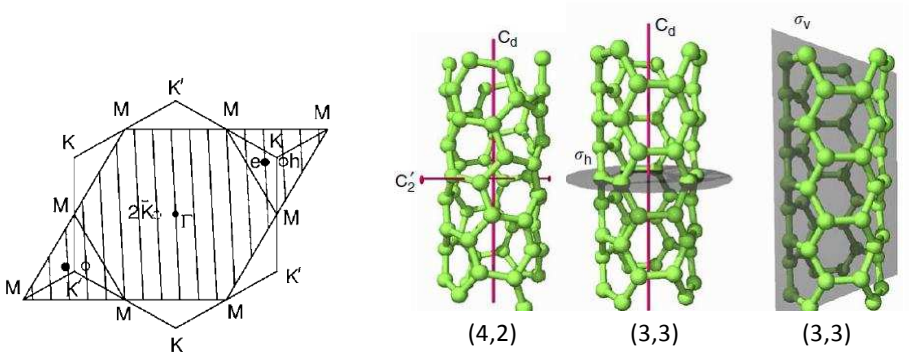

(a) (b)

Figure 2-7: (a) Symmetries of chiral (4,2) SWNT and achiral (3,3) SWNT [5].The tube axis is denoted by C_d, and the axis perpendicular to the tube axis is denoted by $C_2^{'}$. The horizontal and vertical symmetry planes for (3,3) SWNT, σ_h and σ_v, respectively, are shown by gray planes. (b) Electron-hole pairs in three inequivalent regions of the Brillouin zone of graphene for (6,5) SWNT [7]. A excitons correspond to an electron and hole pair in K or $K^{'}$ regions in which $2\boldsymbol{K} = \boldsymbol{k}_c - \boldsymbol{k}_v$ lies in Γ region. E and E^* excitons correspond to an electron from K region and an hole from $K^{'}$ region, and vice versa, in which $2\boldsymbol{K}$ lies in K and $K^{'}$ regions, respectively.

2.4.1 Symmetries of exciton and Dipole selection rules in carbon nanotube

Excitons in a carbon nanotube can be classified by the symmetries of that carbon nanotube [5] and by wave vector of the center of mass [7]. According to both cases, there are four kinds of the excitons: A_1 , A_2 , E and E^* . A_1 and A_2 excitons have $\boldsymbol{K} = 0$ and are called A excitons, but they have different symmetries.E and E^*, called E excitons, are $K \neq 0$ excitons which are all dark. These four excitons in the Brillouin zone of graphene are shown in Fig. 2-7(a). In Fig. 2-7(a), A excitons have $2\boldsymbol{K} = \boldsymbol{k}_c - \boldsymbol{k}_v$ that lies in Γ region because both electron and hole are in the same K or $K^{'}$ region. E and E^* excitons have $2\boldsymbol{K}$ that lies in K and $K^{'}$, respectively, because an electron and hole are in K and $K^{'}$ regions, $K^{'}$ and K regions, respectively. We are interested in the vertical transition in this thesis, thus only the symmetries and the Dipole selection rules of the A excitons will be discussed.

Fig. 2-7(a): fig:/exciton-symmetry-Jiang.eps

A_1 and A_2 are the irreducible representation defined by the character table of the point group D_N for chiral nanotube, where N is a number of hexagons in the nanotube unit cell, and the exciton wavefunction that have these symmetries are called A_1 exciton and A_2 exciton, respectively. The A_1 exciton is symmetric with respect to C_2 rotation (rotation by π) about the axis perpendicular to the tube axis, while the A_2 exciton is anti-symmetric with respect to the C_2 rotation. There are $N/2$ axes, $C_2^{'}$, that go through the center of bonds between two inequivalent carbon atoms as shown in the Fig. 2-7(b), and the other $N/2$ axes, $C_2^{''}$, that can go through the centers of the hexagons. For achiral nanotube, armchair and zigzag, there are additional symmetry operations: inversion, horizontal reflection and vertical reflection. The mirror planes of the horizontal vertical reflections for armchair carbon nanotube are shown in Fig. 2-7(b). Then, the additional symbols, g (gerade : even) and u (ungerade : odd), are added to A_1 and A_2 to be A_{1g}, A_{1u}, A_{2g}, and A_{2u}. These symmetries are in the point group D_{Nh} [1].

According to the dipole selection rules without near field, the transition probability is proportional to $|\hat{\boldsymbol{P}} \cdot \langle\Psi|\nabla|\Psi_0\rangle|^2$ with $|\Psi\rangle$ and $|\Psi_0\rangle$ denoting the excited and ground states, respectively, and $\hat{\boldsymbol{P}}$ denoting the polarization of laser light. The ground state $|\Psi_0\rangle$ is totally symmetric, and the ∇ transforms as the antisymmetric under C_2 rotation. The excited state $|\Psi\rangle$ must be antisymmetric under C_2 rotation to have non-zero transition probability. Therefore, A_2 excitons are bright exciton and A_1 excitons are dark exciton for chiral nanotube. However, it should be noted that in two-photon photoluminescence experiment, the A_1 excitons become optically active and A_2 excitons become dark [12]. For zigzag and armchair carbon nanotubes, the A_{2u} exciton are dipole optically active or bright excitons and the remaining excitons are all dark exciton [5]. However, in two-photon experiment, the A_{1g} exciton are accessed and the remaining excitons become dark [12].

2.4.2 Wavefunctions of exciton in carbon nanotube

The exciton energy Ω^n and the wavefunction Ψ^n are obtained by solving the Bethe-Salpeter equation (BS-equation) by mixing different $\boldsymbol{k}_v$ and $\boldsymbol{k}_c$ wave vectors written

as follows

$$\sum_{\boldsymbol{k}_c\boldsymbol{k}_v} \left\{ [E(\boldsymbol{k}_c) - E(\boldsymbol{k}_v)]\delta_{\boldsymbol{k}'_c\boldsymbol{k}_c}\delta_{\boldsymbol{k}'_v\boldsymbol{k}_v} + K(\boldsymbol{k}'_c\boldsymbol{k}'_v, \boldsymbol{k}_c\boldsymbol{k}_v) \right\} \Psi^n(\boldsymbol{k}_c\boldsymbol{k}_v) = \Omega^n \Psi^n(\boldsymbol{k}'_c\boldsymbol{k}'_v), \quad (2.117)$$

where $E(\boldsymbol{k}_c)$ and $E(\boldsymbol{k}_v)$ are energies of electron and hole in an excited state obtained by adding Coulomb interaction to one-particle energy, $K(\boldsymbol{k}'_c\boldsymbol{k}'_v, \boldsymbol{k}_c\boldsymbol{k}_v)$ is called kernel showing the mixing of wave vectors as expressed by

$$K(\boldsymbol{k}'_c\boldsymbol{k}'_v, \boldsymbol{k}_c\boldsymbol{k}_v) = -K^{\mathrm{d}}(\boldsymbol{k}'_c\boldsymbol{k}'_v, \boldsymbol{k}_c\boldsymbol{k}_v) + 2\delta_S K^{\mathrm{x}}(\boldsymbol{k}'_c\boldsymbol{k}'_v, \boldsymbol{k}_c\boldsymbol{k}_v), \quad (2.118)$$

where K^{d} is direct interaction obtained from screened Coulomb potential, K^{x} is exchange interaction obtained from bare Coulomb potential, δ_S is one and zero for singlet and triplet excitons, respectively, [1]. Wave vectors from one cutting line are sufficient to describe the E_{ii} transition for small-diameter nanotubes (0.5< d_t <2.0 nm) because the Coulomb interaction is larger than the diameter d_t of SWNT [7]. By solving the BS-equation, the exciton energy dispersion becomes the Hydrogen-like that is discrete energy levels. Each energy level is labeled by the integer $\nu = 0, 1, 2, 3, \ldots$. Then, the exciton wavefunction $|\vec{k}, \vec{K}\rangle$ of the vertical transition near K point can be written as :

$$|\boldsymbol{k}, \boldsymbol{K}\rangle = \sum_k Z_k^\nu \Psi_k^c\left(\vec{r}_e\right) \Psi_k^{v*}\left(\vec{r}_h\right). \quad (2.119)$$

where Z_k^ν are obtained by solving the BS-equation. Z_k^ν is called as the envelop-function [6], and ν can be either even and odd numbers depending on the reflection symmetry about the plane perpendicular to the tube axis (horizontal plane). Ψ^c and Ψ^v are the one-particle wavefunctions of the valence band and the conduction band, respectively. The one-particle wavefunctions are written as the linear combination of the Bloch wavefunctions $\Phi_{\mathrm{A}}(\boldsymbol{k}, \boldsymbol{r})$ and $\Phi_{\mathrm{B}}(\boldsymbol{k}, \boldsymbol{r})$ of A and B atoms, respectively, in the graphene lattice :

$$\Psi_k^{v(c)}(\boldsymbol{r}) = c_{\mathrm{A}}^{v(c)}\Phi_{\mathrm{A}}(\boldsymbol{k}, \boldsymbol{r}) + c_{\mathrm{B}}^{v(c)}\Phi_{\mathrm{B}}(\boldsymbol{k}, \boldsymbol{r}), \quad (2.120)$$

where the Bloch wavefunction $\Phi_{\mathrm{A(B)}}(\boldsymbol{k},\boldsymbol{r})$ is expressed as :

$$\Phi_{\mathrm{A(B)}}(\boldsymbol{k},\boldsymbol{r}) = \frac{1}{\sqrt{N}}\sum_{j=1}^{N} e^{i\boldsymbol{k}\cdot\boldsymbol{R}^{j}_{\mathrm{A(B)}}}\varphi\left(\boldsymbol{r}-\boldsymbol{R}^{j}_{\mathrm{A(B)}}\right), \tag{2.121}$$

where $\varphi\left(\boldsymbol{r}-\boldsymbol{R}^{j}_{\mathrm{A(B)}}\right)$ is $2pz$ atomic orbital centered at A(B) atom in the unit cell of the graphene lattice. The A excitons are obtained by mixing the k wave vectors of electron and hole from K and K' points so that the wave vector of the center of mass $\boldsymbol{K}$ of the excitons become zero by means of the vertical transition. $\boldsymbol{k}$ wave vector around K' point has the opposite sign as $\boldsymbol{k}$ from K point, but the $\boldsymbol{K}$ is the same for both K and K' points. The A_1 exciton is symmetric , and the A_2 exciton is antisymmetric under C_2 rotation about the axes perpendicular to the tube axis. Therefore, the linear combination between the excitons from K and K' points of A_1 and A_2 excitons are expressed as follow in order to fulfill the symmetry [7] :

$$A_{2,1} = \frac{1}{\sqrt{2}}\left(|\boldsymbol{k},\boldsymbol{K}\rangle \pm |-\boldsymbol{k},\boldsymbol{K}\rangle\right). \tag{2.122}$$

where $|\boldsymbol{k},\boldsymbol{K}\rangle$ is the exciton wavefunction from K point, and $|-\boldsymbol{k},\boldsymbol{K}\rangle$ is the exciton wave function from K' point, written in Eq. (2.119). It can be seen that the plus sign is for A_2 exciton, and the minus sign is for A_1 exciton. The symmetry of A excitons can be confirmed by making the C_2 rotation on the exciton wavefunctions expressed in Eq. (2.122) and then using the relations: $\hat{C}_2\Psi_v = \Psi^*_v$ and $\hat{C}_2\Psi_c = -\Psi^*_c$. By substituting Eq. (2.119) into Eq. (2.122), the A_2 exciton wavefunction Ψ^{ν}_2 with an electron on the s' atom in the graphene lattice j', and hole on the s atom in the graphene lattice j, can be expressed as [7] :

$$\Psi^{\nu}_2(j's',js) = \sum_{k} Z^{\nu}_k \mathrm{Re}\left[C^{c}_{s'}(\boldsymbol{k})C^{v*}_{s}e^{i\boldsymbol{k}\cdot(\boldsymbol{R}_{j's'}-\boldsymbol{R}_{ju})}\right]. \tag{2.123}$$

Here, Ψ^{ν}_2 for $\nu = 1,2,3$ of E_{22} transition of (8,0) SWNT obtained from STB method is shown in Fig. 2-8. In Fig. 2-8(a) and 2-8(c), we show the exciton wavefunction for the electron and hole on the A atom that is (A,A), because the exciton wavefunction

for (B,B) , (A,B), or (B,A) is similar to (A,A). However, the exciton wavefunction for $\nu = 1$, (A,A) or (B,B) is not allowed. Then, the exciton wavefunction in Fig. 2-8(b) is for (A,B) case [7]. It is noted here that the x-axis in the original paper should be divided by the lattice constant, 2.46 nm, to be consistent with our plot. According to Fig. 2-8, three excitonic states are orthogonal. Then, the nodes appear on the tube axis according to the value of ν. The A_2^0 is well localized with the full width at half maximum about 2 nm. The exciton becomes delocalize by increasing energy and tube diameter. Ψ_2^0 and Ψ_2^2 are symmetric, and Ψ_2^1 is anti-symmetric with respect to the reflection about the plane perpendicular to the tube axis. Therefore, Ψ_2^0 and Ψ_2^2 are denoted by A_{2g}, and Ψ_2^1 is denoted by A_{2u}, for excitons in armchair and zigzag SWNTs.

The exciton wavefunctions of A excitons can also be written in term of the second quantization where the electron creation $\hat{c}^\dagger$ and the electron annihilation $\hat{c}$ are introduced. The wavefunction of the conduction band is obtained by operating the creation operator to the ground state $|0\rangle$, and the wavefunction of the valence band is obtained by operating the annihilation operator to the ground state. Then, the A excitons becomes :

$$\Psi\left(A_2^\nu\right) = \frac{1}{\sqrt{2}} \sum_k Z_k^\nu \left(\hat{c}_k^\dagger \hat{c}_k + \hat{c}_{-k}^\dagger \hat{c}_{-k}\right) |0\rangle, \tag{2.124}$$

$$\Psi\left(A_1^\nu\right) = \frac{1}{\sqrt{2}} \sum_k Z_k^\nu \left(\hat{c}_k^\dagger \hat{c}_k - \hat{c}_{-k}^\dagger \hat{c}_{-k}\right) |0\rangle. \tag{2.125}$$

where subscript k and $-k$ of the creation and annihilation operators, respectively, denote wave vectors from K and K' point. The Eq. (2.125) and Eq. (2.125) are very useful in constructing the exciton-photon matrix element of dipole approximation and also the exciton-near field matrix element.

After solving the BS-equation for particular transition energy E_{ii}, the envelop function Z_k^ν is obtained. If only one-particle wavefunctions of π electron are used, the method is called simple tight binding approximation (STB). In STB approximation, the curvature of SWNT is neglected so that there is no mixing of π electron and

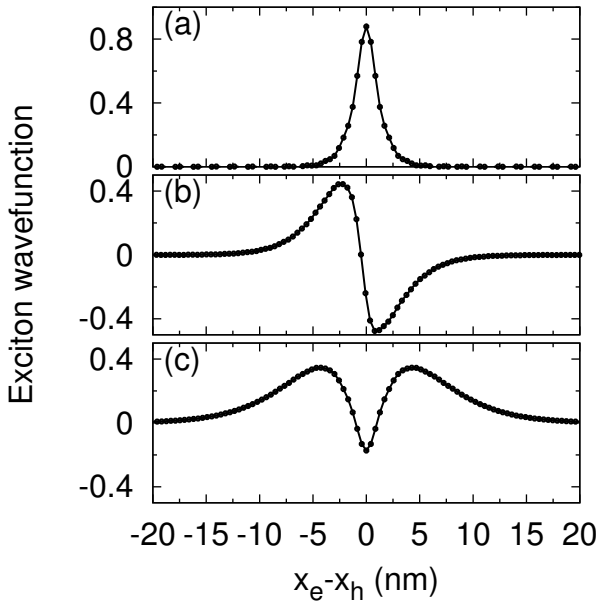

Figure 2-8: **Amplitude of A_2 exciton wavefunction for E_{22} transition as a function of relative distance along tube axis of** $(8,0)$ **SWNT.** (a) Amplitude of the A_2 exciton wavefunction of the first excitonic state ($\nu = 0$). (b) Amplitude of the A_2 exciton wavefunction of the second excitonic state ($\nu = 1$). (c) Amplitude of the A_2 exciton wavefunction of the third excitonic state ($\nu = 3$).

s electron. If the curvature effect of SWNT is taken into account, the mixing of p orbitals and s orbitals can not be neglected, and the method is called extended tight binding approximation (ETB).

2.4.3 Exciton-photon matrix element

In this section, the formulation of the exciton-photon matrix element in the Dipole approximation is given. This work has been done by J. Jiang et al. [8] based on the second quantization. However, in this thesis, the electromagnetic field will not be quantized which means that the classical vector potential is used in the formulation. This approach has been used by A. Grünei et al. [3] to calculate the optical absorption of graphene and SWNT.

Fig. 2-8: fig:/exwf-swnt0800-e22go.eps

The Hamiltonian of an electron in the electromagnetic field can be written as :

$$\hat{H} = \frac{[\boldsymbol{p} - e\boldsymbol{A}(\boldsymbol{r}, t)]^2}{2m} + V(\boldsymbol{r}), \tag{2.126}$$

where $\boldsymbol{p}$ is linear momentum of the electron, $\boldsymbol{A}$ is the classical vector potential of the electromagnetic field, e is the electronic charge, m is mass of the electron and $V(\boldsymbol{r})$ is the electronic potential of the electron. The linear term $\propto \boldsymbol{A}$ of the squared conjugated momentum is retained and the squared term $\propto \boldsymbol{A}^2$ will be neglected because the latter is much smaller than the former for the power of light. The nonlinear effect can not be neglected for high energy electromagnetic field. By applying the Coulomb gauge, that is, $\nabla \cdot \boldsymbol{A} = 0$, the linear momentum become commute with the vector potential, then the one-particle Hamiltonian is simply written as :

$$H = \left[\frac{\boldsymbol{p}^2}{2m} + V(\boldsymbol{r})\right] - \frac{e}{m}\boldsymbol{A}(\boldsymbol{r}, t) \cdot \boldsymbol{p} = H_0 + H^{'}(t), \tag{2.127}$$

where H_0 is defined as the unperturbed Hamiltonian, and $H^{'}(t)$ is defined as the time-dependent perturbed Hamiltonian. In Coulomb gauge, the classical vector potential is related to the classical electric field by $\boldsymbol{E} = -\frac{\partial \boldsymbol{A}}{\partial t}$, and then $\boldsymbol{A} = -\frac{i}{\omega}\boldsymbol{E}$ by assuming the time-harmonic dependence $e^{-i\omega t}$. Therefore, the time-dependent perturbed Hamiltonian of one particle can be written in term of the classical electric field as :

$$H^{'}(t) = \frac{e\hbar}{m\omega}\boldsymbol{E}(t) \cdot \nabla. \tag{2.128}$$

In the second quantization, wavefunction of many-particles system is reinterpreted as an operator written as the linear combination of the one-particle wavefunctions which form the complete set :

$$\hat{\Psi}(\boldsymbol{r}, t) = \sum_k \hat{c}_k(t)\psi_k(\boldsymbol{r}), \tag{2.129}$$

where $\hat{c}_k(t) = e^{-i\varepsilon_k t/\hbar}\hat{c}_k$, ε_k is one-particle energy. $\hat{c}_k$ and $\hat{c}_k^{\dagger}$ satisfy the anticommu-

tation relations :

$$\{\hat{c}_k, \hat{c}_{k'}^\dagger\} = \delta_{kk'}, \qquad \{\hat{c}_k, \hat{c}_{k'}\} = 0, \qquad \{\hat{c}_k^\dagger, \hat{c}_{k'}^\dagger\} = 0, \tag{2.130}$$

where $\delta_{kk'}$ is a Delta function. $\hat{c}_k$ and $\hat{c}_k^\dagger\}$ are called the annihilation and the creation operators, respectively. $\hat{c}_k$ annihilate an electron in the state k, the operation will be zero if it either operates on the ground state or there is no electron in the state k. $\hat{c}_k^\dagger$ creates an electron in state k, the operation will be zero if and only if the state k has been already occupied by the electron. The Hamiltonian of the transition from the initial state to the final state is defined in the second quantization as :

$$\hat{H}_{el-op} = \int \mathrm{d}\boldsymbol{r} \hat{\Psi}_f \hat{H}' \hat{\Psi}_i. \tag{2.131}$$

By substituting the initial and final states written as Eq. (2.129) and the perturbed one-particle Hamiltonian from Eq. (2.128) into Eq. (2.131), the Hamiltonian of the vertical transition $k_c = k_v$ is written as :

$$\hat{H}_{el-op} = \frac{e\hbar}{m\omega} E_x \sum_k D_k \hat{c}_{k_c}^\dagger \hat{c}_{k_v}, \tag{2.132}$$

where E_x is the electric field parallel to the tube axis (x-axis) which is constant along the tube axis because the wavelength of the laser light is much larger than the atomic distance (Dipole approximation), and D_k is the dipole vector defined as follows :

$$D_k = \langle \Psi_k^c | \frac{\partial}{\partial x} | \Psi_k^v \rangle, \tag{2.133}$$

where the subscript c and v, respectively, denote the conduction band and the valence band, and $k_c = k_v$ for the vertical transition.

The exciton-photon matrix elements M_{ex-op} of A_2^ν and A_1^ν excitons from the dipole approximation are obtained by calculating the following integral :

$$M_{ex-op}(A_{2(1)}^\nu) = \langle \Psi(A_{2(1)}^\nu) | \hat{H}_{el-op} | 0 \rangle. \tag{2.134}$$

By substituting the A_2^ν and A_1^ν from Eq. (2.125) and Eq. (2.125),respectively, into Eq. (2.134), the matrix elements of A excitons are written as :

$$M_{ex-op}(A_2^\nu) = \frac{1}{\sqrt{2}}\frac{e\hbar}{m\omega}E_x\sum_k Z_k^{\nu*}\left(D_k + D_{-k}\right), \tag{2.135}$$

$$M_{ex-op}(A_1^\nu) = \frac{1}{\sqrt{2}}\frac{e\hbar}{m\omega}E_x\sum_k Z_k^{\nu*}\left(D_k - D_{-k}\right). \tag{2.136}$$

Because the dipole vector is real, $D_k = D_{-k}$. Therefore, the matrix element of A_1 excitons are always zero for all ν, and the matrix element of A_2^n is exist :

$$M_{ex-op}(A_2^\nu) = \sqrt{2}\frac{e\hbar}{m\omega}E_x\sum_k Z_k^{\nu*}D_k \qquad , \qquad M_{ex-op}(A_1^n) = 0. \tag{2.137}$$

It can be seen that the amplitude of the matrix element is proportional to E_x. If laser light is polarized along the tube axis, $E_x = E_0$ where E_0 is the amplitude if the laser light. If laser light is a plane wave, the amplitude E_0 can be calculated from the intensity using the relation : $E_0 = \sqrt{\frac{I}{\varepsilon_0 c}}$ where ε_0 is the permittivity of vacuum and c is the speed of light in free space. The intensity I can be calculated from the power and area of the focus of laser light.

The dipole vector D_k can be obtained by substituting the one-particle wavefunctions of the valence band and the conduction band from Eq. (2.120) into Eq. (2.133). Then, $M_{ex-op}(A_2^\nu)$ can be expressed as :

$$M_{ex-op}(A_2^\nu) = \sqrt{2}\frac{e\hbar}{m\omega}E_x\sum_k Z_k^{\nu*} \tag{2.138}$$

In addition to Eq. (2.137), $M_{ex-op}(A_2^\nu)$ can be written in terms of the A_2 exciton wavefunction Ψ_2^ν written in Eq. (2.123) by substituting the one-particle wavefunctions of the valence band and the conduction band expressed in Eq. (2.120) into the dipole vector around K and K' points. Then, the $M_{ex-op}(A_2^\nu)$ can be written in terms of Ψ_2^ν as follows :

Chapter 3

Exciton-near field matrix element

This chapter is devoted to the formulation of the exciton-near field matrix element based on the exciton theory of carbon nanotube developed by J. Jiang et al. [7] and classical near field obtained from Mie's theory as described in chapter 2. By using the classical scattered wave radiated from a small metallic sphere which has only the dipole mode ($l = 1$), the near field along the tube axis of SWNT can be simply obtained by the geometry. The exciton-near field matrix element of the vertical transition is then constructed by replacing the incident electric field in the exciton-photon matrix element by the near field along tube axis. The concept of the effective optical matrix element is introduced to be used in the calculation of the effective enhancement factor γ.

3.1 Near field function

The system of a small metallic sphere with radius a placed at distance d above a SWNT is shown in Fig. 3-1. Here, wavevector of the incident light is defined as $\boldsymbol{q}$ to avoid the confusion with wavevectors in the Brillouin zone of SWNT. The incident electric field is polarized along tube axis giving rise to the vertical transition along the tube axis. The scattered electric field $\boldsymbol{E}^{\mathrm{s}}$ of the dipole term ($l = 1$) is taken only from the TM mode which corresponds to the electronic vibration in the metallic sphere. Therefore, the dipole $\boldsymbol{E}^{\mathrm{s}}$ has two components in radial direction (E_r^{s}) and in

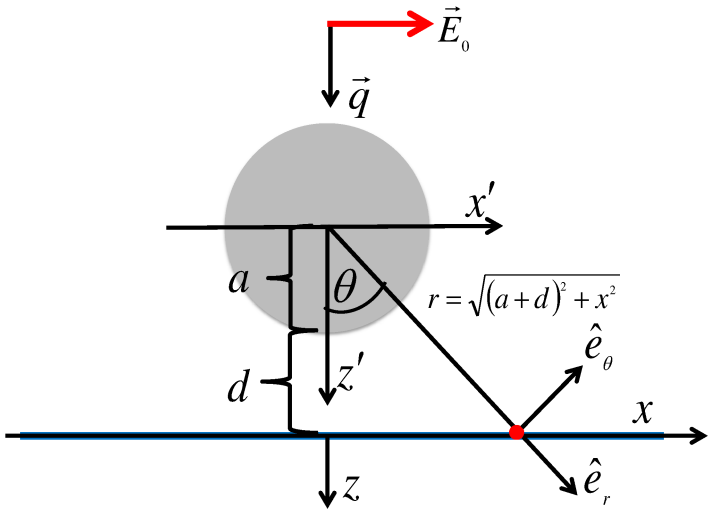

Figure 3-1: **System of a metallic sphere on SWNT.** x-axis is defined as the tube axis, and z-axis is perpendicular to the tube axis. Wave vector of an incident light is denoted as $\boldsymbol{q}$ pointing in z direction meaning that the incident light is traveling to a SWNT from the top. The incident electric field $\boldsymbol{E}_0$ is polarized parallel to the tube axis. Radius a and separation distance d are defined as parameters. The unit vectors of the spherical coordinate in radial and polar directions are defined as $\hat{\boldsymbol{e}}_r$ and $\hat{\boldsymbol{e}}_\theta$, respectively. r is the radial distance from the center of a metallic sphere.

polar direction ($E^{\rm s}_\theta$) written in the spherical coordinate as :

$$\boldsymbol{E}^{\rm s} = E^{\rm s}_r \hat{\boldsymbol{e}}_r + E^{\rm s}_\theta \hat{\boldsymbol{e}}_\theta, \tag{3.1}$$

where

$$E^{\rm s}_r = \tilde{a}_{11}\Big[-\frac{i}{(qr)^3}-\frac{1}{(qr)^2}\Big]e^{iqr}\sin\theta\ ,\ E^{\rm s}_\theta = \frac{\tilde{a}_{11}}{2}\Big[\frac{i}{(qr)^3}+\frac{1}{(qr)^2}-\frac{i}{qr}\Big]e^{iqr}\cos\theta. \tag{3.2}$$

$\tilde{a}_{11}$ is the dipole scattering coefficient of TM mode obtained by assigning $l = 1$ in Eq. 2.93. The unit of $\tilde{a}_{11}$ is the same as the unit of electric field, V/m. By retaining the terms proportional to $1/r^3$ of $E^{\rm s}_r$ and $E^{\rm s}_\theta$ in Eq. (3.2) and using the transformations from the spherical coordinate to the cartesian coordinate, $\hat{\boldsymbol{e}}_r = \sin\theta\hat{\boldsymbol{e}}_x - \cos\theta\hat{\boldsymbol{e}}_z$ and

Fig. 3-1: fig:/exciton-nf-system.eps

$\hat{\boldsymbol{e}}_\theta = \cos\theta\hat{\boldsymbol{e}}_x + \sin\theta\hat{\boldsymbol{e}}_z$, the near field $\boldsymbol{E}^{\rm nf}$ can be written in x- and $z-$ direction as :

$$\begin{aligned}\boldsymbol{E}^{\rm nf} &= \left[-\frac{i\tilde{a}_{11}}{(qr)^3}\sin^2\theta + \frac{i\tilde{a}_{11}}{2(qr)^3}\cos^2\theta\right]\hat{\boldsymbol{e}}_x + \\ &\left[\frac{i\tilde{a}_{11}}{(qr)^3} + \frac{i\tilde{a}_{11}}{2(qr)^3}\right]\sin\theta\cos\theta\hat{\boldsymbol{e}}_z. \end{aligned} \tag{3.3}$$

By substituting $\sin\theta = \frac{x}{r}$ and $\cos\theta = \frac{a+d}{r}$ into the near field in x-direction in Eq. (3.3), the near field along tube axis $E_x^{\rm nf}$ can be written as :

$$E_x^{\rm nf} = \frac{i\tilde{a}_{11}}{2}\frac{1}{[q(a+d)]^3}\left\{\left[\frac{(a+d)^2-2x^2}{r^2}\right]\left(\frac{a+d}{r}\right)^3\right\} = \frac{i\tilde{a}_{11}}{2}\frac{1}{[q(a+d)]^3}f_x^{\rm nf3}(x), \tag{3.4}$$

where $f_x^{\rm nf3}(x)$ is defined as

$$f_x^{\rm nf3}(x) = \left\{\left[\frac{(a+d)^2-2x^2}{r^2}\right]\left(\frac{a+d}{r}\right)^3\right\}. \tag{3.5}$$

$f_x^{\rm nf3}(x)$ is real dimensionless function of a position along the tube axis x which is maximum of 1 at $x = 0$. We will call $f_x^{\rm nf3}(x)$ as near field function originated from terms proportional to $1/r^3$ in this thesis. Because $f_x^{\rm nf3}(x)$ is symmetric along the tube axis, it can be fitted with Gaussian basis function $I_\alpha\exp(-\beta_\alpha x^2)$, where I_α and β_α are Gaussian fitting parameters. The Gaussian fitting function of $f_x^{\rm nf3}(x)$ can be used to calculate the near field matrix element.

If we also retain the terms proportional to $1/r^2$ in Eq. (3.2), near field along the tube axis $E_x^{\rm nf}$ can be written as :

$$E_x^{\rm nf} = \left\{\frac{i\tilde{a}_{11}}{2}\frac{1}{[q(a+d)]^3}\right\}\left\{f_x^{\rm nf3}(x) + if_x^{\rm nf2}(x)\right\} = \left\{\frac{i\tilde{a}_{11}}{2}\frac{1}{[q(a+d)]^3}\right\}f_x^{\rm nf}(x), \tag{3.6}$$

where $f_x^{\rm nf2}(x)$ is defined as :

$$f_x^{\rm nf2}(x) = -\frac{q(a+d)\left[(a+d)^2-2x^2\right]}{r^2}\left(\frac{a+d}{r}\right)^2, \tag{3.7}$$

and $f_x^{\rm nf}(x) = f_x^{\rm nf3}(x) + if_x^{\rm nf2}(x)$. We also call $f_x^{\rm nf2}(x)$ as the near field function origi-

Fig. **??**: fig:/efenf-swnt427-5nm.eps

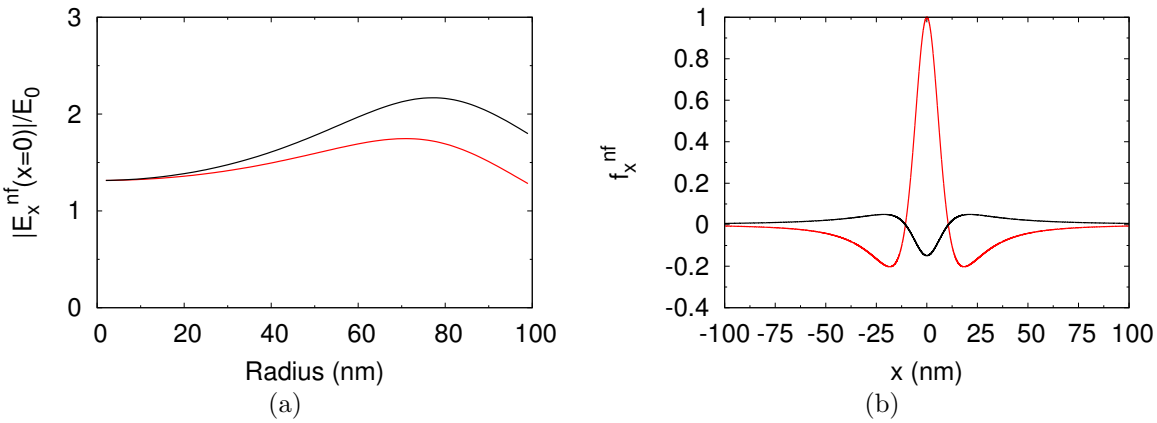

Figure 3-2: **Near field enhancement and near field functions.** (a) Near field enhancement, $|E_x^{\rm nf}(x=0)|/E_0$, with only $f_x^{\rm nf3}$ (red line), or both $f_x^{\rm nf3}$ and $f_x^{\rm nf2}$ (black line), as a function of radius of a gold sphere excited by the He-Ne laser light with the wavelength 633 nm. The separation distance d is zero. (b) Near field functions $f_x^{\rm nf3}$ (red line) and $f_x^{\rm nf2}$ (black line) as a function of distance along the tube axis of SWNT whose length is 200 nm. The separation distance d is zero and radius of a gold sphere a is 15 nm ($a+d=15$ nm).

nated from terms proportional to $1/r^2$. It can be seen that adding terms proportional to $1/r^2$ is equivalent to adding the imaginary part to $f_x^{\rm nf3}(x)$. $f_x^{\rm nf2}(x)$ is also symmetric as shown by the black line in Fig. 3-2(b). At $x=0$, the magnitude of $f_x^{\rm nf2}(x)$ is equal to $-q(a+d)$. Then, we can fit the near field functions $f_x^{\rm nf3}(x)$ and $f_x^{\rm nf2}(x)$ with the Gaussian basis functions as :

$$f_x^{\rm nf3}(x) = \sum_\alpha I_\alpha \exp\left(-\beta_\alpha x^2\right), \tag{3.8}$$

$$f_x^{\rm nf2}(x) = -q(a+d)\sum_{\alpha'} I_{\alpha'} \exp\left(-\beta_{\alpha'} x^2\right),, \tag{3.9}$$

where I_α and β_α are Gaussian fitting parameters.

In Fig. 3-2(a), we show the near field enhancement at $x=0$, $|E_x^{\rm nf}(x=0)|/E_0$ by taking into account only $f_x^{\rm nf3}$ (red line), or both $f_x^{\rm nf3}$ and $f_x^{\rm nf2}$ (black line), as a function of radius. The separation distance is defined to be zero ($d=0$). The metallic sphere is a gold sphere excited by an He-Ne laser light with the wavelength 633 nm. The corresponding bulk dielectric constant of a gold sphere acquired from

the fitting function [38] is about $\tilde{\varepsilon} = -11.425 + 1.186i$. The maximum of the near field enhancement for the black line is about 2.2 at the radius about 80 nm, while the near field enhancement of the red line of the same radius is about 1.7. The near field enhancement of the black line and the red line for a small gold sphere with the radius less than 20 nm is not much different from each other. From this figure we can see that the maximum of the near field enhancement for the gold sphere excited by the He-Ne laser light with the wavelength 633 nm occurs at large sphere about 80 nm, and the near field function $f_x^{\rm nf2}$ can not be negligible for large metallic sphere. In Fig. 3-2(b), we also plot the near field functions $f_x^{\rm nf3}$ (red line) and $f_x^{\rm nf2}$ (black line) with $a = 15$ nm, $d = 0$, and the wavelength 633 nm, as a function of distance along the tube axis of SWNT whose length is 200 nm. $f_x^{\rm nf3}$ is always equal to 1 at $x = 0$, but the magnitude of $f_x^{\rm nf2}$ at $x = 0$ is equal to $-q(a + d)$ according to its definition in Eq. (3.7). Then, $f_x^{\rm nf2}$ is -0.15 at $x = 0$ for $a + d = 15$ nm, and $\lambda = 633$ nm. The full width at half maximum (FWHM) of the near field function $f_x^{\rm nf3}$ (red line) is about 11.5 nm, and the FWHM of the near field function $f_x^{\rm nf2}$ (black line) is about 12.1 nm which is slightly larger than the former. The FWHM of the near field function is a linear function of $a + d$, and for $f_x^{\rm nf3}$, it can be approximated that FWHM $= 0.77(a + d)$ nm. By adding $if_x^{\rm nf2}$ to $f_x^{\rm nf3}$, the FWHM of the near field function becomes a little bit larger than that of the $f_x^{\rm nf3}$. The near field function $f_x^{\rm nf3}$ become negative at $x \approx \pm 10.61$ nm because the amplitude of radial component of the near field whose sign is opposite to the amplitude of polar component becomes larger than the latter.

3.2 Formulation of exciton-near field matrix element

We modify the time-dependent perturbed Hamiltonian of one-particle as written in Eq. (2.128) by adding the scattered electric field $\boldsymbol{E}^{\rm s}$ to the incident electric field $\boldsymbol{E}^{\rm i}$ which becomes the total electric field outside a metallic sphere according to

G. Mie [25]. Then, the one-particle perturbed Hamiltonian of the scattered light is written in the same from as Eq. (2.128) by $H^{'}(t) = \frac{e\hbar}{m\omega}\boldsymbol{E}^{\mathrm{s}}(t)\cdot\nabla$. Unlike the dipole approximation that the incident electric field is treated as constant along the tube axis [3], the scattered electric field $\boldsymbol{E}^{\mathrm{s}}$ is localized near the metallic sphere, and then it can not be taken outside the integration. By following the same steps as section 2.4.3, the exciton-near field matrix elements of A_2 and A_1 excitons for the vertical transition can be expressed as :

$$M_{ex-nf}(A_2^{\nu}) = \sqrt{2}\frac{e\hbar}{m\omega}\frac{1}{2}\Sigma_k Z_k^{\nu *}\{S_k + S_{-k}\}, \tag{3.10}$$

$$M_{ex-nf}(A_1^{\nu}) = \sqrt{2}\frac{e\hbar}{m\omega}\frac{1}{2}\Sigma_k Z_k^{\nu *}\{S_k - S_{-k}\}, \tag{3.11}$$

where S_k is defined as the transition matrix element written as follows :

$$S_k = \langle\Psi_k^c|E_x^{\mathrm{nf}}\frac{\partial}{\partial x}|\Psi_k^v\rangle, \tag{3.12}$$

where Ψ_k^v and Ψ_k^c are one-particle wavefunctions of valence and conduction bands, respectively, written in Eq. (2.120). By substituting the near field along the tube axis E_x^{nf} from Eq. (3.4) into Eq. (3.12), the transition matrix element S_k becomes :

$$S_k = \frac{i\tilde{a}_{11}}{2}\frac{1}{[q(a+d)]^3}\langle\Psi_k^c|f_x^{\mathrm{nf}}\frac{\partial}{\partial x}|\Psi_k^v\rangle = \frac{i\tilde{a}_{11}}{2}\frac{1}{[q(a+d)]^3}D_k^{\mathrm{N}}, \tag{3.13}$$

where D_k^{N} is defined as the near field matrix element expressed as

$$D_k^{\mathrm{N}} = \langle\Psi_k^c|f_x^{\mathrm{nf}}(x)\frac{\partial}{\partial x}|\Psi_k^v\rangle = \langle\Psi_k^c|\left(f_x^{\mathrm{nf3}}(x) + if_x^{\mathrm{nf2}}(x)\right)\frac{\partial}{\partial x}|\Psi_k^v\rangle. \tag{3.14}$$

The near field matrix element D_k^{N} has the same unit as the Dipole vector D_k. It becomes the same as D_k if and only if $f_x^{\mathrm{nf}} = 1$. Next, we show the formulation of the near field matrix element D_k^{N}. By substituting the one-particle wavefunctions of valence and conduction bands in Eq. (2.120) into the expression of D_k^{N}, four integrals

can be obtained as :

$$D_k^{\rm N} = c_{\rm A}^{c*}c_{\rm A}^{v}\langle\Phi_{\rm A}^{c}(\boldsymbol{k},\boldsymbol{r})|f_x^{\rm nf}\frac{\partial}{\partial x}|\Phi_{\rm A}^{v}(\boldsymbol{k},\boldsymbol{r})\rangle + c_{\rm B}^{c*}c_{\rm B}^{v}\langle\Phi_{\rm B}^{c}(\boldsymbol{k},\boldsymbol{r})|f_x^{\rm nf}\frac{\partial}{\partial x}|\Phi_{\rm B}^{v}(\boldsymbol{k},\boldsymbol{r})\rangle + c_{\rm A}^{c*}c_{\rm B}^{v}\langle\Phi_{\rm A}^{c}(\boldsymbol{k},\boldsymbol{r})|f_x^{\rm nf}\frac{\partial}{\partial x}|\Phi_{\rm B}^{v}(\boldsymbol{k},\boldsymbol{r})\rangle + c_{\rm B}^{c*}c_{\rm A}^{v}\langle\Phi_{\rm B}^{c}(\boldsymbol{k},\boldsymbol{r})|f_x^{\rm nf}\frac{\partial}{\partial x}|\Phi_{\rm A}^{v}(\boldsymbol{k},\boldsymbol{r})\rangle. \quad (3.15)$$

By substituting the Bloch wave functions in Eq. (2.121) into Eq. (3.15) and taking into account only the first nearest neighbor interaction for the last two terms and the interaction on the same atomic site for the first two terms of Eq. (3.15), the near field matrix elements Eq. (3.15) are then written as the sum of (A,A), (B,B) on-site matrix elements, and (A,B), (B,A) off-site matrix elements :

$$D_k^{\rm N} = \frac{1}{N}c_{\rm A}^{c*}c_{\rm A}^{v}\sum_{j=1}^{N}n_{\rm AA} + \frac{1}{N}c_{\rm B}^{c*}c_{\rm B}^{v}\sum_{j=1}^{N}n_{\rm BB} + \frac{1}{N}c_{\rm A}^{c*}c_{\rm B}^{v}\sum_{j=1}^{N}\sum_{p=1}^{3}e^{i\boldsymbol{k}\cdot\boldsymbol{r}_{\rm A}^{p}}n_{\rm AB} + \frac{1}{N}c_{\rm B}^{c*}c_{\rm A}^{v}\sum_{j=1}^{N}\sum_{p=1}^{3}e^{-i\boldsymbol{k}\cdot\boldsymbol{r}_{\rm A}^{p}}n_{\rm BA}, \quad (3.16)$$

where $n_{\rm AA}$ and $n_{\rm BB}$ are called the (A,A) and (B,B) on-site matrix elements, respectively, $n_{\rm AB}$ and $n_{\rm BA}$ are called (A,B) and (B,A) off-site matrix elements, respectively, $\boldsymbol{r}_{\rm A}^{p}$ $(p=1,2,3)$ are first nearest neighbor vectors pointing from A atom to B atom.

The (A,A) and (B,B) on-site matrix elements are expressed as :

$$n_{\rm AA} = \langle\varphi(\boldsymbol{r}-\boldsymbol{R}_{\rm A}^{j})|f_x^{\rm nf3} + if_x^{\rm nf2}\frac{\partial}{\partial x}|\varphi(\boldsymbol{r}-\boldsymbol{R}_{\rm A}^{j})\rangle = n_{\rm AA}^{(3)} + in_{\rm AA}^{(2)}, \quad (3.17)$$

$$n_{\rm BB} = \langle\varphi(\boldsymbol{r}-\boldsymbol{R}_{\rm B}^{j})|f_x^{\rm nf3} + if_x^{\rm nf2}\frac{\partial}{\partial x}|\varphi(\boldsymbol{r}-\boldsymbol{R}_{\rm B}^{j})\rangle = n_{\rm BB}^{(3)} + in_{\rm BB}^{(2)}, \quad (3.18)$$

, and the (A,B) and (B,A) off-site matrix elements are expressed as :

$$n_{\rm AB} = \langle\varphi(\boldsymbol{r}-\boldsymbol{R}_{\rm A}^{j})|f_x^{\rm nf3} + if_x^{\rm nf2}\frac{\partial}{\partial x}|\varphi(\boldsymbol{r}-(\boldsymbol{R}_{\rm A}^{j}+\boldsymbol{r}_{\rm A}^{p}))\rangle = n_{\rm AB}^{(3)} + in_{\rm AB}^{(2)}, \quad (3.19)$$

$$n_{\rm BA} = \langle\varphi(\boldsymbol{r}-\boldsymbol{R}_{\rm B}^{j})|f_x^{\rm nf3} + if_x^{\rm nf2}\frac{\partial}{\partial x}|\varphi(\boldsymbol{r}-(\boldsymbol{R}_{\rm B}^{j}+\boldsymbol{r}_{\rm B}^{p}))\rangle = n_{\rm BA}^{(3)} + in_{\rm BA}^{(2)}, \quad (3.20)$$

where $\boldsymbol{R}_{\rm A}^{j}$ and $\boldsymbol{R}_{\rm B}^{j}$ are A and B atomic positions in the unit cell j of graphene lattice. The superscript (3) and (2) denotes the matrix element of the near field function $f_x^{\rm nf3}$

and $f_x^{\rm nf2}$, respectively. The $\boldsymbol{r}_{\rm A}^p$ and $\boldsymbol{r}_{\rm B}^p$, $(p = 1, 2, 3)$, are the first nearest neighbor vectors pointing from A atom and B atom, respectively, with the relation $\boldsymbol{r}_{\rm B}^p = -\boldsymbol{r}_{\rm A}^p$.

Near field on-site matrix element

We show the formulae of (A,A) and (B,B) on-site matrix elements and discuss their behavior in this section. In the Dipole approximation, the on-site matrix elements are disappear due to the symmetry. However, because of the appearance of the near field function $f_x^{\rm nf}$ in the integration, the on-site matrix elements may exit for near field. The (A,A) on-site near field matrix element $n_{\rm AA}^{(3)}$ defined in Eq. (3.17) is expressed as

$$n_{\rm AA}^{(3)} = \langle \varphi(\boldsymbol{r} - \boldsymbol{R}_{\rm A}^j) | f_x^{\rm nf3}(x) \frac{\partial}{\partial x} | \varphi(\boldsymbol{r} - \boldsymbol{R}_{\rm A}^j) \rangle. \tag{3.21}$$

By substituting the Gaussian fitting functions of the $2pz$ atomic orbital and the near field function $f_x^{\rm nf3}$ into Eq. (3.21), the $n_{\rm AA}^{(3)}$ can be expressed as

$$n_{\rm AA}^{(3)} = \frac{1}{n} \sum_{k,l,\alpha} 2\beta_l I_l I_k I_\alpha \{L_x\}\{L_y\}\{L_z\}, \tag{3.22}$$

where the indices k and l are for the $2pz$ atomic orbital, and the index α is for the near field function. The integrals L_x, L_y and L_z are expressed as

$$\begin{aligned} L_x &= -\int_{-\infty}^{\infty} {\rm d}x (x - x_{\rm A}^j) \exp\left[-\gamma_{kl}(x - x_{\rm A}^j)^2 - \beta_\alpha x^2 \right], & (3.23) \\ L_y &= \int_{-\infty}^{\infty} {\rm d}y \exp\left[-\gamma_{kl} \left(y - y_{\rm A}^j \right)^2 \right], & (3.24) \\ L_z &= \int_{-\infty}^{\infty} {\rm d}z z^2 \exp\left(-\gamma_{kl} z^2 \right), & (3.25) \end{aligned}$$

where $\gamma_{kl} = \beta_k + \beta_l$, $x_{\rm A}^j$ and $y_{\rm A}^j$ are the components of A atom in the graphene lattice j on the tube axis and the circumference, respectively. L_y and L_z can be integrated immediately using the Gaussian integral formulae. Then, $L_y = \sqrt{\frac{\pi}{\gamma_{kl}}}$, and $L_z = \sqrt{\frac{\pi}{\gamma_{kl}}} \left(\frac{1}{2\gamma_{kl}} \right)$. L_x is more complicate. However, the steps are straightforward.

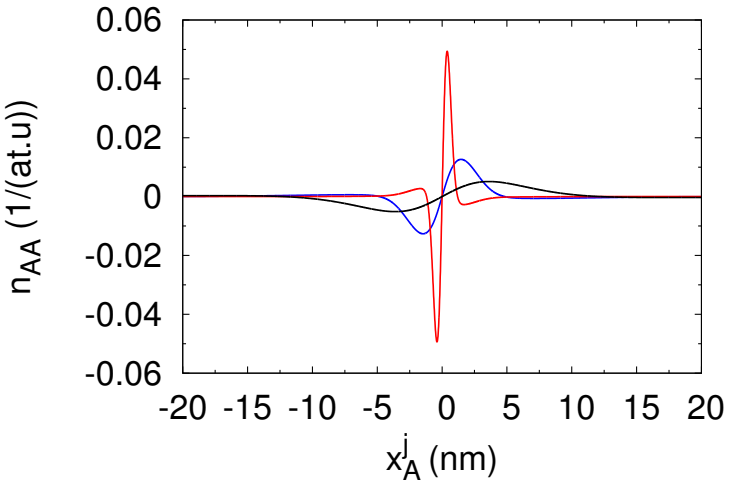

Figure 3-3: **(A,A) on-site matrix element n_{AA} as a function of x_{A}^{j}.** Red line shows n_{AA} of $a+d=1$ nm, blue line shows n_{AA} of $a+d=4$ nm and black line shows n_{AA} of $a+d=10$. The separation distance d is defined as zero ($d=0$).

Firstly, the exponential term of Eq. (3.23) is expanded to be written in following form

$$\exp\left[-\gamma_{kl}(x-x_{\mathrm{A}}^{j})^{2}-\beta_{\alpha}x^{2}\right]=\exp\left[-\frac{\gamma_{kl}\beta_{\alpha}}{\gamma_{kl}+\beta_{\alpha}}\left(x_{\mathrm{A}}^{j}\right)^{2}\right]\exp\left[-\left(\gamma_{kl}+\beta_{\alpha}\right)\left(x-x_{0}\right)^{2}\right], \tag{3.26}$$

where $x_0 = \frac{\gamma_{kl}}{\gamma_{kl}+\beta_{\alpha}}x_{\mathrm{A}}^{j}$. Then L_x can be integrated analytically using the Gaussian integral formulae, and it can be expressed as

$$L_{x}=x_{\mathrm{A}}^{j}\frac{\beta_{\alpha}}{\gamma_{kl}+\beta_{\alpha}}\sqrt{\frac{\pi}{\gamma_{kl}+\beta_{\alpha}}}\exp\Big[-\frac{\gamma_{kl}\beta_{\alpha}}{\gamma_{kl}+\beta_{\alpha}}(x_{\mathrm{A}}^{j})^{2}\Big]. \tag{3.27}$$

By substituting L_x, L_y and L_z into Eq. (3.22), the $n_{\mathrm{AA}}^{(3)}$ can be expressed as

$$n_{\mathrm{AA}}^{(3)}(x_{\mathrm{A}}^{j})=x_{\mathrm{A}}^{j}\frac{1}{n}\sum_{k,l,\alpha}\beta_{\alpha}\beta_{l}I_{l}I_{k}I_{\alpha}\frac{1}{\gamma^{2}}\Big(\frac{\pi}{\gamma_{kl}+\beta_{\alpha}}\Big)^{3/2}\exp\Big[-\frac{\gamma_{kl}\beta_{\alpha}}{\gamma_{kl}+\beta_{\alpha}}(x_{\mathrm{A}}^{j})^{2}\Big]. \tag{3.28}$$

The (B,B) on-site matrix element $n_{\mathrm{BB}}^{(3)}$ can be obtained by simply replacing x_{A}^{j} in Eq. (3.28) by x_{B}^{j}. $n_{\mathrm{AA}}^{(2)}$ and $n_{\mathrm{BB}}^{(2)}$ can be also obtained by the same way. The difference between $n_{\mathrm{BB}}^{(3)}$ and $n_{\mathrm{AA}}^{(2)}$ is only the magnitude. It can be seen that the on-site matrix elements are exponential function of the component of the atom on the tube axis

Fig. 3-3: fig:/naa-ad1-4-10nm.eps

which is originated from the localization of the near field. $n^{(3)}_{\rm AA}(n^{(3)}_{\rm BB})$ is proportional to $x^j_{\rm A}(x^j_{\rm B})$ due to the symmetry. If $x^j_{\rm A}(x^j_{\rm B})$ is equal to zero, the near field on-site matrix element vanishes corresponding to the Dipole approximation. In Fig. **??**, $n^{(3)}_{\rm AA}$ as a function of $x^j_{\rm A}$ has been shown for $a+d=1,4,10$ nm with $d=0$. The red line of $a+d=1$ gives the maximum of $n^{(3)}_{\rm AA}$ about 0.05 1/(at.u) at $x^j_{\rm A} \approx= 0.38$ nm. $n^{(3)}_{\rm AA}$ sharply decrease by increasing the $x^j_{\rm A}$. By increasing $a+d$, the peak of $n^{(3)}_{\rm AA}$ becomes broad and the its amplitude decreases because the FWHM of the near field becomes large resulting in the anti-symmetric of the on-site matrix element.

Near field off-site matrix element

The near field off-site matrix elements $n_{\rm AB}$ and $n_{\rm BA}$ are given in this section. We consider only $n_{\rm AB}$ because $n_{\rm BA}$ can be obtained from the former by replacing $x^j_{\rm A}$ by $x^j_{\rm B}$ and the first nearest neighbor vector $\boldsymbol{r}^p_{\rm A}$ by $\boldsymbol{r}^p_{\rm B}$. According to Eq. (3.19), $n^{(3)}_{\rm AB}$ is expressed as

$$n^{(3)}_{\rm AB} = \langle \varphi(\boldsymbol{r}-\boldsymbol{R}^j_{\rm A}) | f^{\rm nf3}_x(x) \frac{\partial}{\partial x} | \varphi(\boldsymbol{r}-(\boldsymbol{R}^j_{\rm A}+\boldsymbol{r}^p_{\rm A})) \rangle. \tag{3.29}$$

We define the A carbon atom on the unrolled graphene sheet as $\boldsymbol{R}^j_{\rm A} = x^j_{\rm A}\hat{\boldsymbol{e}}_x + y^j_{\rm A}\hat{\boldsymbol{e}}_y$ where $x^j_{\rm A}$ and $y^j_{\rm A}$ are the components of the A atom on tube axis and circumference of SWNT, respectively. Three first nearest neighbor vectors pointing out from $\boldsymbol{R}^j_{\rm A}$ are denoted as $\boldsymbol{r}^p_{\rm A} = x^p_{\rm rA}\hat{\boldsymbol{e}}_x + y^p_{\rm rA}\hat{\boldsymbol{e}}_y$. Then, by substituting the Gaussian basis functions of $2pz$ atomic orbital and the near field function $f^{\rm nf3}_x$ into Eq. (3.29), $n^{(3)}_{\rm AB}$ can be written as

$$n^{(3)}_{\rm AB} = \frac{1}{n}\sum_{k,l,\alpha} 2\beta_l I_l I_k I_\alpha \{L_x\}\{L_y\}\{L_z\}, \tag{3.30}$$

where the indices k and l are for the $2pz$ atomic orbital, and the index α is for the near field function. The integrals L_x, L_y and L_z are expressed as

$$\begin{aligned} L_x &= -\int_{-\infty}^{\infty} {\rm d}x[x-(x^j_{\rm A}+x^p_{\rm rA})] \\ &\quad \exp\,[-\beta_k(x-x^j_{\rm A})^2 - \beta_l\Big(x-(x^j_{\rm A}+x^p_{\rm rA})\Big)^2 - \beta_\alpha x^2], \qquad (3.31) \\ L_y &= \int_{-\infty}^{\infty} {\rm d}y \exp\,[-\beta_k\left(y-y^j_{\rm A}\right)^2 - \beta_l(y-(y^j_{\rm A}+y^p_{\rm rA}))^2], \qquad (3.32) \end{aligned}$$

$$L_z = \int_{-\infty}^{\infty} \mathrm{d}z z^2 \exp(-\gamma_{kl} z^2), \tag{3.33}$$

where $\gamma_{kl} = \beta_k + \beta_l$. The $z-$integral (L_z) is the same as the near field on-site matrix element, $L_z = \sqrt{\frac{\pi}{\gamma_{kl}}}\Big(\frac{1}{2\gamma_{kl}}\Big)$. L_y and L_y are slightly difficult. The starting point of making the integration is expanding the exponential term which can be done by the help of following general Gaussian identity

$$\begin{aligned} &\exp[-\beta_k(x-x_a)^2 - \beta_l(x-x_b)^2 - \beta_\alpha(x-x_c)^2] \\ &\qquad = C_{kl\alpha} \exp[-(\gamma_{kl}+\beta_\alpha)(x-x_0)^2], \end{aligned} \tag{3.34}$$

where $C_{kl\alpha}(x_a, x_b, x_c)$ and x_0 are expressed as :

$$\begin{aligned} C_{kl\alpha} &= \exp\Big[-\frac{\beta_k\beta_l}{\gamma_{kl}+\beta_\alpha}(x_a-x_b)^2 - \frac{\beta_k\beta_\alpha}{\gamma_{kl}+\beta_\alpha}(x_a-x_c)^2 - \\ &\quad \frac{\beta_l\beta_\alpha}{\gamma_{kl}+\beta_\alpha}(x_b-x_c)^2\Big], \end{aligned} \tag{3.35}$$

$$x_0 = \frac{\beta_k x_a + \beta_l x_b + \beta_\alpha x_c}{\gamma_{kl}+\beta_\alpha}. \tag{3.36}$$

Then, by expanding the exponential terms of L_x and L_y using Eqs. (3.35)-(3.36), and using the Gaussian integral formulae, the L_x and L_y are expressed as :

$$L_x(x^j_{\mathrm{A}}, x^p_{\mathrm{rA}}) = C_{kl\alpha}\Big(\frac{1}{\gamma_{kl}+\beta_\alpha}\Big)\sqrt{\frac{\pi}{\gamma_{kl}+\beta_\alpha}}[\beta_\alpha x^j_{\mathrm{A}} + (\beta_k+\beta_\alpha)x^p_{\mathrm{rA}}], \tag{3.37}$$

$$L_y(y^p_{\mathrm{rA}}) = \sqrt{\frac{\pi}{\gamma_{kl}}}\exp[-\frac{\beta_k\beta_l}{\gamma_{kl}}(y^p_{\mathrm{rA}})^2]. \tag{3.38}$$

Then, $n^{(3)}_{\mathrm{AB}}$ is expressed as

$$\begin{aligned} n^{(3)}_{\mathrm{AB}}(x^j_{\mathrm{A}}, x^p_{\mathrm{rA}}) &= \frac{1}{n}\sum_{k,l,\alpha}\beta_l I_l I_k I_\alpha \frac{1}{\gamma^2_{kl}}\Big(\frac{\pi}{\gamma_{kl}+\beta_\alpha}\Big)^{3/2}[\beta_\alpha x^j_{\mathrm{A}} + (\beta_k+\beta_\alpha)x^p_{\mathrm{rA}}] \\ &\quad \exp\Big[-\frac{\beta_k\beta_l}{\gamma_{kl}+\beta_\alpha}(a_{\mathrm{c-c}})^2 - \frac{\beta_k\beta_\alpha}{\gamma_{kl}+\beta_\alpha}(x^j_{\mathrm{A}})^2 \\ &\quad -\frac{\beta_l\beta_\alpha}{\gamma_{kl}+\beta_\alpha}(x^j_{\mathrm{A}} + x^p_{\mathrm{rA}})^2\Big]. \end{aligned} \tag{3.39}$$

Fig. 3-4: fig:/nab3-ad15nm-lam633nm.eps

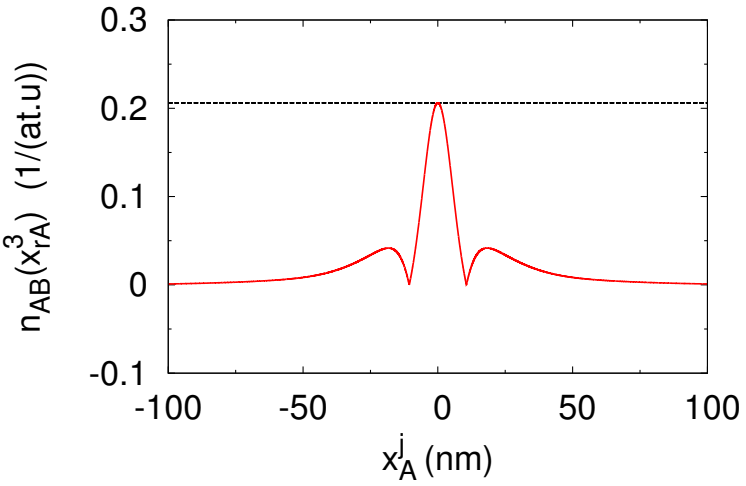

Figure 3-4: **The near field (A,B) off-site matrix element as a function of $x^j_{\rm A}$.** The solid red line is the near field off-site matrix element $n^{(3)}_{\rm AB}$, and the dashed black line represents the off-site matrix element of the Dipole approximation. We define the radius as $a = 15$ nm, and the separation distance as $d = 0$, $a + d = 50$ nm. The wavelength of the laser light is 633 nm. The component of the first nearest neighbor vector on the tube axis is $x^3_{\rm rA} = -a_{\rm c-c}$, where $a_{\rm c-c} = 0.142$ nm, C-C atomic distance.

Similarly, $n^{(2)}_{\rm AB}$ defined in Eq. (3.19) can be expressed as

$$
\begin{aligned}
n^{(2)}_{\rm AB}(x^j_{\rm A}, x^p_{\rm rA}) \;=\; & -q(a+d)\frac{1}{n}\sum_{k,l,\alpha'} \beta_l I_l I_k I_{\alpha'} \frac{1}{\gamma^2_{kl}}\Big(\frac{\pi}{\gamma_{kl}+\beta_{\alpha'}}\Big)^{3/2}[\beta_{\alpha'} x^j_{\rm A} + (\beta_k + \beta_{\alpha'}) x^p_{\rm rA}] \\
& \exp\Big[-\frac{\beta_k \beta_l}{\gamma_{kl}+\beta_{\alpha'}}(a_{\rm c-c})^2 - \frac{\beta_k \beta_{\alpha'}}{\gamma_{kl}+\beta_{\alpha'}}(x^j_{\rm A})^2 \\
& -\frac{\beta_l \beta_{\alpha'}}{\gamma_{kl}+\beta_{\alpha'}}(x^j_{\rm A} + x^p_{\rm rA})^2\Big]. \qquad (3.40)
\end{aligned}
$$

Eq. (3.39) becomes the same as the Dipole approximation when $\beta_\alpha = 0$, $I_\alpha = 1$, and without summation on α, which means that $f^{\rm nf}_x = 1$. The exponential decay of $n_{\rm AB}$ appears because of the localization of the near field. In Fig. 3-4, we show the magnitude of the $n^{(3)}_{\rm AB}$ (solid red line) as a function of $x^j_{\rm A}$ for the first nearest neighbor $\boldsymbol{r}^3_{\rm A}$ of zigzag SWNT whose the component on the tube axis $x^3_{\rm rA}$ is $-a_{\rm c-c}$, where $a_{\rm c-c} = 0.142$ nm, C-C atomic distance. The radius of a gold sphere is $a = 15$ nm, and the separation distance $d = 0$ nm. Then, the FWHM of the near field function $f^{\rm nf3}_x$ is about 11.5 nm. The wavelength of the laser light is 633 nm. It can

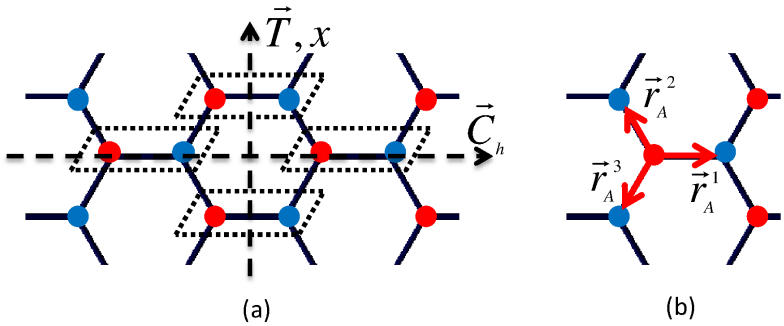

Figure 3-5: **Coordinate and first nearest neighbor vectors in an unrolled graphene lattice of armchair SWNT.** (a) Coordinate of armchair SWNT in which the origin is defined at the center of an hexagon, and tube axis and circumference are in $\boldsymbol{T}$ and $\boldsymbol{C}_h$ directions, respectively. Unit cells of graphene lattice are represented by dotted parallelograms. Two inequivalent carbon atoms A and B in graphene unit cell are denoted by red and blue circles, respectively. (b) Three first nearest neighbor vectors : $\boldsymbol{r}_{\rm A}^1 = \left(\frac{a_0}{C_h}\right)\boldsymbol{C}_h$, $\boldsymbol{r}_{\rm A}^2 = -\left(\frac{a_0/2}{C_h}\right)\boldsymbol{C}_h + \left(\frac{\sqrt{3}a_0/2}{T}\boldsymbol{T}\right)$, $\boldsymbol{r}_{\rm A}^3 = -\left(\frac{a_0/2}{C_h}\right)\boldsymbol{C}_h - \left(\frac{\sqrt{3}a_0/2}{T}\boldsymbol{T}\right)$, where $a_0 = 0.142$ nm is C-C distance.

be seen that the FWHM of the $n_{\rm AB}^{(3)}$ is the same as that of the near field function $f_x^{\rm nf3}$. Therefore, the enhancement of near field matrix element is only inside the region enclosed by the FWHM of near field function. The magnitude of near field matrix element becomes much smaller than that of the far field matrix element outside this region. The magnitude of the $n_{\rm AB}^{(3)}$ doesn't have much difference as the $n_{\rm AB}$ by including the $n_{\rm AB}^{(2)}$.Note that the relation $n_{\rm AB}(x_{\rm A}^j, -x_{\rm rA}^p) = -n_{\rm AB}(x_{\rm A}^j, x_{\rm rA}^p)$ is always satisfied.

3.3 Exciton-Near field matrix element of achiral SWNTs

This section gives the explicit formulae of the near field matrix elements of armchair and zigzag SWNTs.

3.3.1 Near field matrix element of armchair SWNTs

Fig. 3-5: fig:/armchair-swnt.eps

The origin in the unrolled graphene sheet of an armchair SWNT is defined at the intersection point between the z'-axis or $\theta = 0$ axis of the metallic sphere in Fig. 3-1 and the centre of an hexagon of the unrolled graphene sheet as shown in Fig. 3-5(a). The graphene lattice unit cell is denoted by an dotted parallelograms in Fig. 3-5(a). It can be seen that $x_{\rm A}^j = x_{\rm B}^j$ in the graphene unit cell j. The first nearest neighbor vectors of an armchair SWNT are also shown in Fig. 3-5(b). They can be written in terms of vectors $\boldsymbol{T}$ and $\boldsymbol{C}_h$ of the unrolled carbon nanotube unit cell as $\boldsymbol{r}_{\rm A}^1 = \left(\frac{a_{c-c}}{C_h}\right)\boldsymbol{C}_h$, $\boldsymbol{r}_{\rm A}^2 = -\left(\frac{a_{c-c}/2}{C_h}\right)\boldsymbol{C}_h + \left(\frac{\sqrt{3}a_{c-c}/2}{T}\boldsymbol{T}\right)$, $\boldsymbol{r}_{\rm A}^3 = -\left(\frac{a_{c-c}/2}{C_h}\right)\boldsymbol{C}_h - \left(\frac{\sqrt{3}a_{c-c}/2}{T}\boldsymbol{T}\right)$, where $a_{c-c} = 0.142$ nm is the C-C atomic distance. Because D_k^N in Eq. (3.13) is a real function in the reciprocal space of Armchair SWNTs, that is, $D_k^N = D_{-k}^N$. Then, the exciton-near field matrix element of A_1 excitons are zero for all ν. The exciton-near field matrix element of the A_2 excitons can be obtained by substituting S_k in Eq. (3.13) to $M_{\rm ex-nf}(A_2^\nu)$ in Eq. (3.10), then $M_{\rm ex-nf}(A_2^\nu)$ can be written as

$$M_{\rm ex-nf}(A_2^\nu) = \sqrt{2}\frac{e\hbar}{m\omega}\left\{\frac{i\tilde{a}_{11}}{2}\frac{1}{[q(a+d)]^3}\right\}\sum_k Z_k^{\nu *} D_k^N. \tag{3.41}$$

Next, we will consider the summation $\sum_k Z_k^{\nu *} D_k^N$ in Eq. (3.41) for armchair SWNTs. Let's us consider D_k^N in Eq. (3.15) for an armchair SWNTs. The coefficients of the one-particle wavefunctions of the valence band and the conduction band for A and B atoms obtained from the STB method can be expressed as [3]

$$c_{\rm A}^v(\boldsymbol{k}) = \frac{1}{\sqrt{2\left(1+sw(\boldsymbol{k})\right)}}\sqrt{\frac{f(\boldsymbol{k})}{w(\boldsymbol{k})}}, \quad c_{\rm B}^v(\boldsymbol{k}) = \frac{1}{\sqrt{2\left(1+sw(\boldsymbol{k})\right)}}\sqrt{\frac{f^*(\boldsymbol{k})}{w(\boldsymbol{k})}}, \tag{3.42}$$

$$c_{\rm A}^c(\boldsymbol{k}) = \frac{1}{\sqrt{2\left(1-sw(\boldsymbol{k})\right)}}\sqrt{\frac{f(\boldsymbol{k})}{w(\boldsymbol{k})}}, \quad c_{\rm B}^c(\boldsymbol{k}) = -\frac{1}{\sqrt{2\left(1-sw(\boldsymbol{k})\right)}}\sqrt{\frac{f^*(\boldsymbol{k})}{w(\boldsymbol{k})}} \tag{3.43}$$

where s is the overlap integral, $f(\boldsymbol{k}) = \sum_{p=1}^3 \exp\left(i\boldsymbol{k}\cdot\boldsymbol{r}_{\rm A}^p\right)$, and $w(\boldsymbol{k}) = |f(\boldsymbol{k})|$. For the valence band, the coefficient becomes complex conjugate by changing atomic sites from A atom to B atom and vice versa. The coefficient of the conduction band becomes minus complex conjugate by changing the atomic sites. The products of the coefficients for the near field (A,A) and (B,B) on-site matrix elements satisfy

the relation $c_{\rm A}^{c*}(\boldsymbol{k})c_{\rm A}^{v}(\boldsymbol{k}) = -c_{\rm B}^{c*}(\boldsymbol{k})c_{\rm B}^{v}(\boldsymbol{k})$. Furthermore, we also have that $n_{\rm AA} = n_{\rm BB}$, because $x_{\rm A}^{j} = x_{\rm B}^{j}$. Therefore, the contribution of the near field on-site matrix elements of the armchair SWNTs is always zero. Then, D_k^N for armchair can be written as

$$\begin{aligned} D_k^{\rm N} &= \frac{1}{N} c_{\rm A}^{c*}(\boldsymbol{k}) c_{\rm B}^{v}(\boldsymbol{k}) \sum_{j=1}^{N} \sum_{p=1}^{3} e^{i\boldsymbol{k}\cdot\boldsymbol{r}_{\rm A}^{p}} n_{\rm AB}\left(x_{\rm A}^{j}, x_{\rm rA}^{p}\right) + \\ &\quad \frac{1}{N} c_{\rm B}^{c*}(\boldsymbol{k}) c_{\rm A}^{v}(\boldsymbol{k}) \sum_{j=1}^{N} \sum_{p=1}^{3} e^{-i\boldsymbol{k}\cdot\boldsymbol{r}_{\rm A}^{p}} n_{\rm AB}\left(x_{\rm A}^{j}, -x_{\rm rA}^{p}\right). \end{aligned} \tag{3.44}$$

By using the relation $n_{\rm AB}\left(x_{\rm A}^{j}, -x_{\rm rA}^{p}\right) = -n_{\rm AB}\left(x_{\rm A}^{j}, x_{\rm rA}^{p}\right)$ and neglecting $n_{\rm AB}\left(x_{\rm A}^{j}, x_{\rm rA}^{1}\right)$ because of small value compared with other two nearest neighbor vectors, D_k^N can be expanded by summing on p. Then, D_k^N can be written in term of the summation of $n_{\rm AB}\left(x_{\rm A}^{j}, x_{\rm rA}^{2}\right)$ on j multiplied by k-dependence function as

$$D_k^{\rm N} = \frac{1}{N} \left\{ \sum_{j=1}^{N} n_{\rm AB}(x_{\rm A}^{j}, x_{\rm rA}^{2}) \right\} \left\{ c_{\rm A}^{c*}(\boldsymbol{k}) c_{\rm B}^{v}(\boldsymbol{k}) \phi(\boldsymbol{k}) - c_{\rm B}^{c*}(\boldsymbol{k}) c_{\rm A}^{v}(\boldsymbol{k}) \phi^{*}(\boldsymbol{k}) \right\}, \tag{3.45}$$

where $\phi(\boldsymbol{k}) = \exp(i\boldsymbol{k}\cdot\boldsymbol{r}_{\rm rA}^{2}) - \exp(i\boldsymbol{k}\cdot\boldsymbol{r}_{\rm rA}^{3})$. By substituting $\boldsymbol{r}_{\rm rA}^{2}$ and $\boldsymbol{r}_{\rm rA}^{3}$ as shown in Fig. 3-5 to $\phi(\boldsymbol{k})$, the phase factor $\phi(\boldsymbol{k})$ can be written as :

$$\phi(\boldsymbol{k}) = 2i \sin\left(\frac{ka}{2}\right) \exp\left(-i\frac{\mu\pi a}{C_h\sqrt{3}}\right), \tag{3.46}$$

where k is the wavenumber along the tube axis, μ is the cutting index, $a = \sqrt{3}a_{c-c} =$ 0.246 nm is graphene lattice constant, and C_h is the circumference of SWNT. Then, the summation $\sum_k Z_k^{\nu*} D_k^N$ can be written explicitly as

$$\begin{aligned} \sum_k Z_k^{\nu*} D_k^N &= \frac{1}{N} \left\{ \sum_{j=1}^{N} n_{\rm AB}(x_{\rm A}^{j}, x_{\rm rA}^{2}) \right\} \\ &\quad \left\{ \sum_k Z_k^{\nu*} \left[c_{\rm A}^{c*}(\boldsymbol{k}) c_{\rm B}^{v}(\boldsymbol{k}) \phi(\boldsymbol{k}) - c_{\rm B}^{c*}(\boldsymbol{k}) c_{\rm A}^{v}(\boldsymbol{k}) \phi^{*}(\boldsymbol{k}) \right] \right\}. \end{aligned} \tag{3.47}$$

The normalization constant $1/N$, where N is the total number of graphene lattices in SWNTs, appears in Eq. (3.47) because $n_{\rm AB}$ is not a constant of $x_{\rm A}^{j}$, instead it

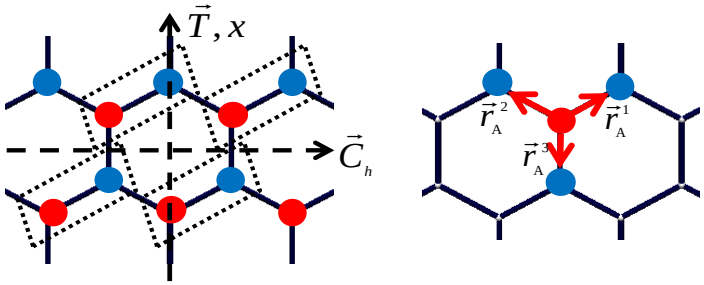

Figure 3-6: **Coordinate and first nearest neighbor vectors in an unrolled graphene lattice of zigzag SWNT.** (a) Coordinate of zigzag SWNT in which the origin is defined at the center of an hexagon, and tube axis and circumference are in $\vec{T}$ and $\vec{C}_h$ directions, respectively. Unit cells of graphene lattice are represented by dotted parallelograms. Two inequivalent carbon atoms A and B in graphene unit cell are denoted by red and blue circles, respectively. (b) Three first nearest neighbor vectors of zigzag SWNT : $\boldsymbol{r}_{\rm A}^1 = \sqrt{3}a_0/2\left(\frac{\boldsymbol{C}_h}{C_h}\right) + a_0/2\left(\frac{\boldsymbol{T}}{T}\right)$, $\boldsymbol{r}_{\rm A}^2 = -\sqrt{3}a_0/2\left(\frac{\boldsymbol{C}_h}{C_h}\right) + a_0/2\left(\frac{\boldsymbol{T}}{T}\right)$, $\boldsymbol{r}_{\rm A}^3 = -a_0\left(\frac{\boldsymbol{T}}{T}\right)$, where $a_0 = 0.142$ nm is C-C distance.

exponentially decays by increasing $x_{\rm A}^j$ as shown in Fig. 3-4. By increasing the number of graphene unit cells N in a SWNT, the number of wavenumber k along the tube axis increases. The increasing of the number of k raises the term summation on k in Eq. (3.47). However, the factor $1/N$ strongly reduces $\sum_{j=1}^{N} n_{\rm AB}(x_{\rm A}^j, x_{\rm rA}^2)$. Then, $\sum_k Z_k^{\nu *} D_k^N$ decreases by increasing N. Therefore, the exciton-near field matrix element would vanish by increasing length of a SWNT, if all $x_{\rm A}^j$ were taken into account.

3.3.2 Near field matrix element of zigzag SWNTs

The coordinate of a zigzag SWNT is shown in Fig. 3-6(a) together with the first nearest neighbor vectors in Fig. 3-6(b) . The origin is defined at the center of the hexagon where a line perpendicular to the tube axis passes through the origin of the metallic sphere. A and B carbon atoms in a graphene unit cell are denoted by red and blue color, respectively. According to the coordinate of the zigzag SWNT, A and B atoms in graphene unit cell j have different position on the tube axis, that

Fig. 3-6: fig:/zigzag-swnt.eps

is, $x_{\rm A}^j \neq x_{\rm B}^j$. Then, unlike the armchair SWNT, the summation $\sum_k Z_k^{\nu *} D_k^N$ can not be further simplified. Therefore, we may write the summation on k for A_2 exciton explicitly as

$$\begin{aligned}\sum_k Z_k^{\nu *} D_k^N &= \frac{1}{N} \sum_{j=1}^{N} \sum_k \sum_{p=1}^{3} Z_k^{\nu *} [c_{\rm A}^{c*}(\boldsymbol{k}) c_{\rm B}^{v}(\boldsymbol{k}) e^{i\boldsymbol{k}\cdot\boldsymbol{r}_{\rm A}^p} n_{\rm AB}(x_{\rm A}^j, x_{\rm A}^p) + \\ & \quad c_{\rm B}^{c*}(\boldsymbol{k}) c_{\rm A}^{v}(\boldsymbol{k}) e^{-i\boldsymbol{k}\cdot\boldsymbol{r}_{\rm A}^p} n_{\rm BA}(x_{\rm B}^j, -x_{\rm A}^p)],\end{aligned} \tag{3.48}$$

where the exponential phase factor of the first nearest neighbors are $\exp(i\boldsymbol{k}\cdot\boldsymbol{r}_{\rm A}^1) = \exp\left[i\frac{a}{2}\frac{\mu}{d_t/2} + \frac{ika}{2\sqrt{3}}\right]$, $\exp(i\boldsymbol{k}\cdot\boldsymbol{r}_{\rm A}^2) = \exp\left[-i\frac{a}{2}\frac{\mu}{d_t/2} + \frac{ika}{2\sqrt{3}}\right]$, and $\exp(i\boldsymbol{k}\cdot\boldsymbol{r}_{\rm A}^3) = \exp[-\frac{ika}{\sqrt{3}}]$. We also see that the exciton-near field matrix element has smaller value than the exciton-far field matrix element if all graphene lattices in the unrolled carbon nanotube are taken into account.

3.4 Effective enhancement factor of the optical matrix element

So far, we neglect the near field region, and the exciton-near field matrix element includes all atoms in SWNTs. In facts, the near field strongly interacts with atoms only within the near field region defined in the chapter 1. Because the Raman intensity is proportional to the fourth order of the optical matrix element, then we define the effective enhancement factor for the optical matrix element γ_M as follows

$$\gamma_M = (\gamma)^{\frac{1}{4}}, \tag{3.49}$$

where γ is the effective enhancement introduced in the chapter 1. If we define the number of graphene lattice in the near field and far field region as $N_{\rm nf}$ and $N_{\rm ff}$, respectively, the ratio $N_{\rm nf}/N_{\rm ff}$ is approximately the same as the ratio $A_{\rm nf}/A_{\rm ff}$ which

appears in the definition γ. Then, the γ_M can be obtained by following equation

$$\gamma_{\mathrm{M}} = \frac{M_{\mathrm{ex-nf}}/M_{\mathrm{ex-ff}}}{(N_{\mathrm{nf}}/N_{\mathrm{ff}})^{1/4}}, \tag{3.50}$$

where $M_{\mathrm{ex-nf}}$ and $M_{\mathrm{ex-ff}}$ are the exciton-near field matrix element, and the exciton-far field matrix element, respectively. N_{nf} can be obtained by the near field area A_{nf} and the area of graphene lattice as

$$N_{\mathrm{nf}} = \mathrm{int}\left(\frac{A_{\mathrm{nf}}}{|\boldsymbol{a}_1 \times \boldsymbol{a}_2|}\right), \tag{3.51}$$

where $\boldsymbol{a}_1$ and $\boldsymbol{a}_2$ are lattice unit vectors of the graphene lattice. A_{nf} is obtained by the product of FWHM of near field and the circumference of a SWNT. N_{ff} is the total number of graphene lattice in a SWNT, N.

We will show the effective enhancement of the optical matrix element in the next chapter. The validity of our theory will be compared with the experimental relative intensity between the near field Raman intensity and the far field Raman intensity as a function of the separation distance between the tip and the SWNTs which has been reported by L. G. Cancado et al. [14].

Chapter 4

Results and Discussions

In this chapter, we discuss the electric field enhancement (EFE) obtained from the Mie's theory as described in the chapter 2. We show the exciton-near field matrix element, and we discuss the tip-sample distance dependence of the Raman intensity approximated by the theory developed in the chapter 3.

4.1 Electric field enhancement (EFE)

The electric field enhancement (EFE) is defined as the ratio between the amplitude of the maximum of the total electric field outside the metallic sphere and the amplitude of the incident electric field. This point is at the surface of the metallic sphere along the polarization axis as denoted by the red point in Fig. 4-1. The solution of the total electric field is the summation of the incident electric field E^{i}, and the scattered electric field E^{s} which is written as the multipole expansion. Here, we show the EFE obtained by the different number of order l from $l = 1$ to $l = 5$ as a function of the diameter of the gold sphere embedded in the vacuum and excited by the He-Ne laser light with the wavelength 633 nm in Fig. 4-1. The dielectric constant of gold at the wavelength 633 nm is about $-11.4 + 1.2i$ approximated by the fitting function in Eq. (1.21) [38].Note that the amplitude of the scattered electric field in TE mode is small compared to the TM mode, because the TE mode is associated with the magnetic vibration which is typically weak in gold and silver. Then, only

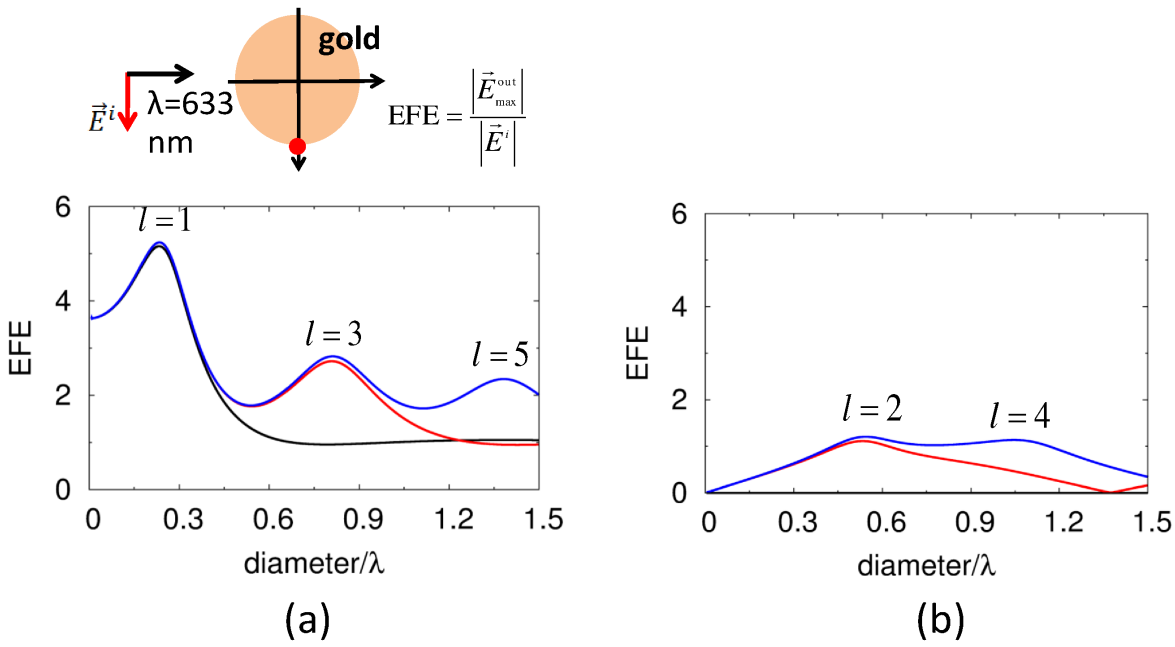

Figure 4-1: **The EFE as a function of diameter of a gold sphere excited by the He-Ne laser light** (a) The EFE as a function of diameter in which only the radial part of the scattered electric field E_r^s is taken into account. The black line includes only the dipole term ($l = 1$), the red line includes $l = 1$ up to $l = 3$, and the blue line takes the terms $l = 1$ up to $l = 5$ into account. Each peak corresponds to the electric resonance for odd l. (b) The EFE as a function of the diameter in which only the polar part of the scattered electric field E_θ^s is taken into account. The black line is zero, and the broad peaks of the red and blue lines correspond to the electric resonance for even l.

the scattered electric field in TM mode is taken into account. In Fig. 4-1(a), only the radial part of the scattered electric field E_r^s is taken into account. Because E_r^s is proportional to $P_l^1(\cos\theta)$, there is no contribution of the even order l to the E_r^s at $\theta = \pi/2$. Then, we can identify each peak in the Fig. 4-1(a) to $l = 1$, $l = 3$, and $l = 5$. In Fig. 4-1(b), only the polar part of the scattered electric field E_θ^s is taken into account. The E_θ^s is proportional to $\frac{dP_l^1(\cos\theta)}{d\theta}$, then there is no contribution of the odd order l to the E_θ^s at $\theta = \pi/2$. The dipole term is always zero in the Fig. 4-1(b), and each broad peak corresponds to the electric resonance of the even l as labelled in this figure. Importantly, the high EFE is due to the dipole resonance $l = 1$, and only the dipole term is sufficient for a small metallic sphere as shown in Fig. 4-1(a).

Fig. 4-1: fig:/EFE1.eps

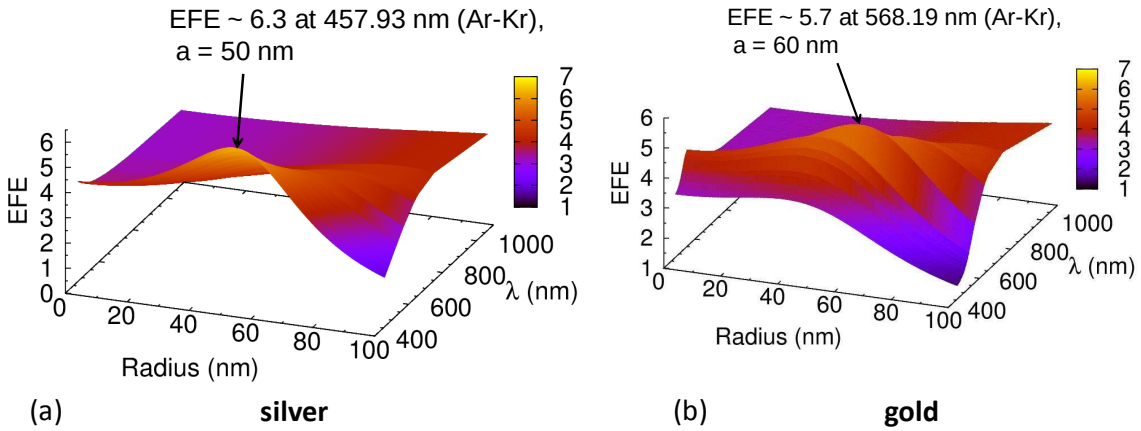

Figure 4-2: **The EFE as a function of wavelength of the available laser light and the radius of small silver and gold spheres.** The contour color denotes the value of the EFE varying from 1 to 7. The bulk dielectric constants of silver and gold as a function of wavelength are obtained from the fitting functions [37, 38]. (a) EFE as a function of wavelength and radius of small silver spheres. (b) EFE as a function of wavelength and radius of small gold spheres.

Hereafter, we will consider only the small metallic sphere compared to the wavelength of the laser light.

In Fig. (4-2)(a) and (4-2)(b), we show the electric field enhancement (EFE) as a function of the available wavelength of the laser light used in spectroscopy and the radius of the silver sphere and the gold sphere, respectively. The maximum of the EFE about 6.3 and 5.7 are obtained for the silver sphere with the radius 50 nm excited by the Ar-Kr laser with the wavelength 457.93 nm, and the gold sphere with the radius 60 nm excited by the Ar-Kr laser with the wavelength 568.19 nm, respectively. By increasing the wavelength from 457.93 nm, the lower and broader peak of the EFE for the silver sphere is shifted to the larger volume as shown in Fig. (4-2)(a). From this calculation, we can see that the maximum of the EFE occurs at the small but finite volume of the metallic sphere.

Let's us consider the EFE as a function of the radius of the silver and gold spheres at the wavelength 350 nm as shown in Fig 4-3(a) and 4-3(b), respectively. The dashed lines in both figures represent the EFE obtained from the quasi-static approximation

Fig. 4-2: fig:/efe-lambda-a.eps
Fig. 4-3: fig:/EFE2.eps

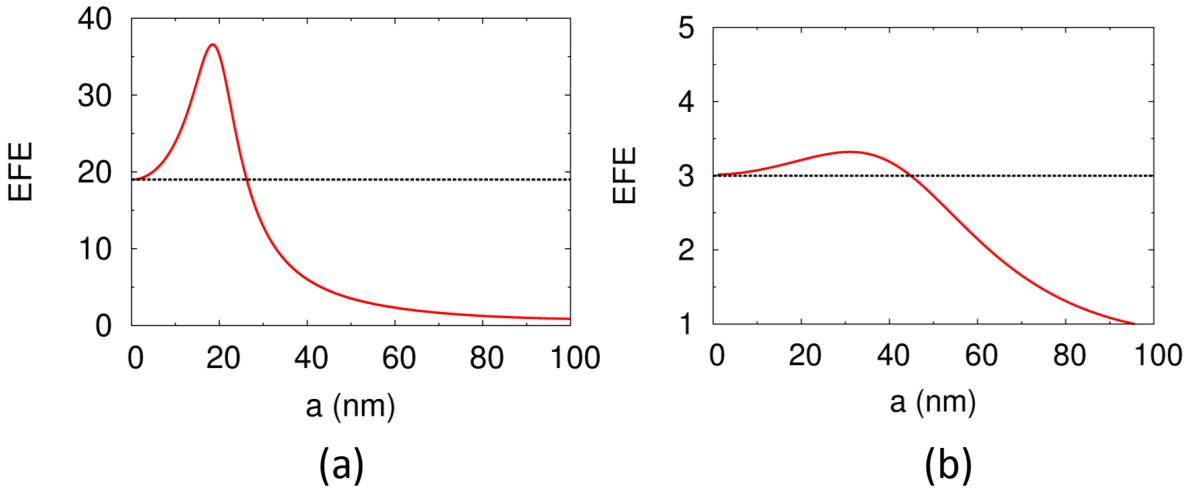

Figure 4-3: **The EFE as a function of radius of small silver and gold spheres at the wavelength 350 nm** (a) The EFE as a function of the radius of the small silver sphere excited by the laser light with the wavelenght 350 nm. The dielectric constant of the silver is approximated by the fitting function in Eq. (1.21) as $-2.36 + 0.11i$ [37]. The red solid line is the EFE obtained from the Mie's theory, and the black dashed line is the EFE obtained from the quasi-static approximation. (b) The EFE as a function of the radius of the small gold sphere excited by the laser light with the wavelength 350 nm. The dielectric constant of the gold is approximated by the fitting function in Eq. (1.21) as $-1.08 + 5.6i$ [38]. The red solid line is the EFE obtained from the Mie's theory, and the black dashed line is the EFE obtained from the quasi-static approximation.

expressed in Eq. (2.14). We can see that the EFE of the silver and gold spheres with the radius less than 5 nm follows the quasi-static approximation. The peak of the EFE in Fig 4-3(a) for the silver sphere is about 36.6 at the radius about 18.5 nm, while the broad peak in Fig 4-3(b) for the gold sphere is about 3.3 at the radius about 30.0 nm which is much smaller than the silver sphere. The large EFE of the 20 nm silver sphere at the wavelength 350 nm is due to the dipole resonance, $\tilde{\varepsilon} = -2\varepsilon_m$, where $\tilde{\varepsilon}$ is the dielectric constant of the metallic sphere and ε_m is the dielectric constant of the medium which is defined as the vacuum ($\varepsilon_m = 1$). The dipole resonance condition appears in Eq. (2.14) of the quasi-static approximation, and it can also be obtained from the Mie's theory by approximating the spherical Bessel function $j_l(z)$ and the spherical Hankel function of the first kind $h_l^{(1)}(z)$ for a small metallic sphere ($x = ka \ll 1$) as $j_l(z) = \frac{2^l l!}{(2l+1)!} z^l$ and $h_l^{(1)} = -\frac{i(2l-1)!}{2^{l-1}(l-1)!} \frac{1}{z^{l+1}}$, respectively [**?**].

Then, by taking the denominator of dipole term $l = 1$ of the scattered electric field as zero, the dipole resonance condition $\tilde{\varepsilon} = -2\varepsilon$ can be obtained. The appearance of the peak of EFE for the silver sphere at the radius 20 nm results from the dynamic depolarization by the dipoles in the sphere [41], which can be explained as follows ; for a small metallic sphere, the polarizability α increases by increasing the factor ka, where k in the wavenumber of light and a is the radius, until the α reaches the maximum, leading to the maximum of the EFE. The decreasing and the broadening of the EFE for larger metallic sphere results from the decreasing and the broadening of the α due to the damping of the dipole. The detail of the dynamic depolarization has been already described in the chapter 2.

In next section, we will show the exciton-near field matrix element as developed in the chapter 3.

4.2 Exciton-near field matrix element

In this section, we show the enhancement of the exciton-near field matrix element. We model the gold tip excited by the He-Ne laser light with the wavelength 633 nm (1.96 eV) as employed by L. G. Cancado *et al.* [14]. The laser light energy is in resonance with the E_{22} transition of the A_2^0 exciton of the (8,0) SWNT [44]. In Fig. 4-4, we show the ratio between the amplitude of the exciton-near field matrix element $M_{\mathrm{ex-nf}}$ and the amplitude of the exciton-far field matrix element $M_{\mathrm{ex-ff}}$ as a function of the component of the A atom in the graphene lattice j on the tube axis (x_{A}^j) of the (8,0) SWNT. The tip-SWNT distance is defined as zero ($d = 0$). We consider the very sharp tip with the tip radius 2 nm (red line), the sharp tip with the tip radius 10 nm which is the typical value of the tip radius used in TERS experiment (blue line), and the slightly larger tip radius 20 nm (black line). The near field along the tube axis E_x^{nf} includes both f_x^{nf3} and f_x^{nf2} terms. For x_{A}^j close to zero, the $|M_{\mathrm{ex-nf}}^j|/|M_{\mathrm{ex-ff}}^j|$ is approximately the same as the near field enhancement $|E_x^{\mathrm{nf}}(x = 0)|/E_0$ as shown in Fig. 3-2. Therefore, the exciton-near field matrix element $M_{\mathrm{ex-nf}}^j$ increases by

Fig. 4-4: fig:/mxexnf-xaj-swnt0800-e22.eps

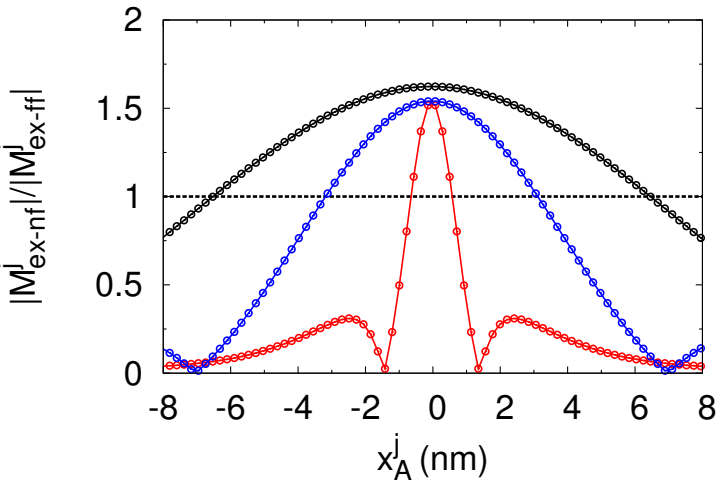

Figure 4-4: **The ratio between the exciton-near field matrix element and the exciton-far field matrix element of the $E_{22}(A_2^0)$ exciton as a function of $x^j_{\rm A}$.** The red line is the gold sphere with the radius 2 nm, the blue line is the gold sphere with the radius 10 nm and the black line is the gold sphere with the radius 20 nm. The tip-SWNT distance is defined as zero.

increasing the radius from 2 nm to 20 nm for $x^j_{\rm A}$ near zero. The amplitude of the $M^j_{\rm ex-nf}$ exponentially decreases by increasing $x^j_{\rm A}$. Then, the amplitude of the $M^j_{\rm ex-nf}$ is greater than that of the $M^j_{\rm ex-ff}$ only within the small region which is smaller than the FWHM of the near field function. For example, the FWHM of the radius 10 nm ($d = 0$) denoted by the blue line is about 7.7 nm, while the enhancement region of the $M^j_{\rm ex-nf}$ is about 6.2 nm. The enhancement region increases by increasing the radius of the gold sphere. In Fig. 4-5, we show the corresponding effective enhancement factors of the exciton-near field matrix elements ($\gamma_{\rm M}$) as defined in Eq. (3.50), taking into account only the matrix elements within the near field area, as a function of small radius a of the gold sphere (red line) compared with the silver sphere (black line). We can clearly see that the small gold sphere gives higher value of the $\gamma_{\rm M}$ than that given by the small silver sphere, because the near field generated by the gold sphere is larger than the near field produced by the silver sphere at the wavelength 633 nm. Therefore, the sharp gold tip will give higher resolution of the TERS Raman image of the SWNT than that obtained by the sharp silver tip if the excitation source is

Fig. 4-5: fig:/gamM-silver-gold-633nm-swnt0800.eps

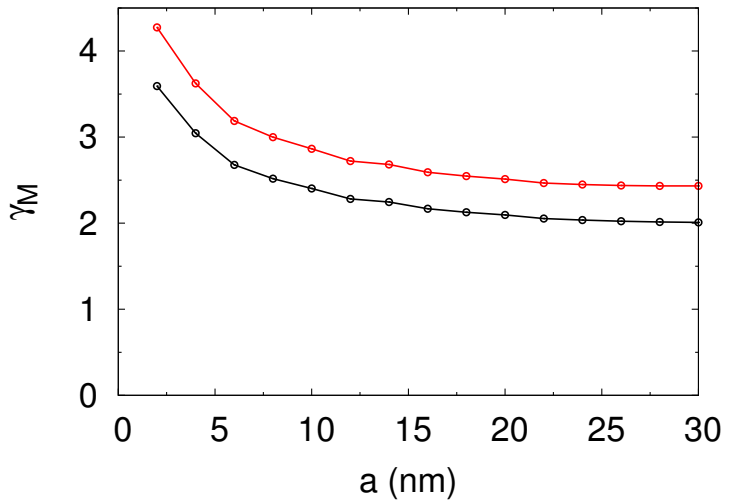

Figure 4-5: γ_{M} **of the** $E_{22}(A_2^0)$ **exciton of (8,0) SWNT as a function of the radius of small gold and silver spheres excited by the He-Ne laser light with the wavelength 633 nm.** The red line is the γ_{M} of the gold sphere, and the black line is the γ_{M} of the silver sphere. The separation distance between the metallic sphere and the SWNT is defined as zero.

the He-Ne laser light with the wavelength 633 nm. Furthermore, the maxima of the γ_{M} for both materials occur at the smallest radius $a = 2$ nm, because of the smallest FWHM along the tube axis, about 1.54 nm. Therefore, the strongly localized near field will give the higher resolution of the TERS Raman image than that obtained by the broadly localized near field. It is noted that the FWHM of the radius $a = 2$ nm is comparable to the FWHM of the A_2^0 exciton wavefunction of the E_{22} transition along the tube axis of the (8,0) SWNT as shown in Fig. 2-8.

In the next section, we consider the enhancement of the Raman intensity approximated by the optical matrix element in the vertical direction by showing the the tip-SWNT distance dependence of the Raman intensity.

4.3 Tip-SWNT distance dependence of the Raman intensity

To calculate the Raman intensity, the exciton-phonon matrix element must be taken into account. The formula of the Raman intensity has been well established [44], and

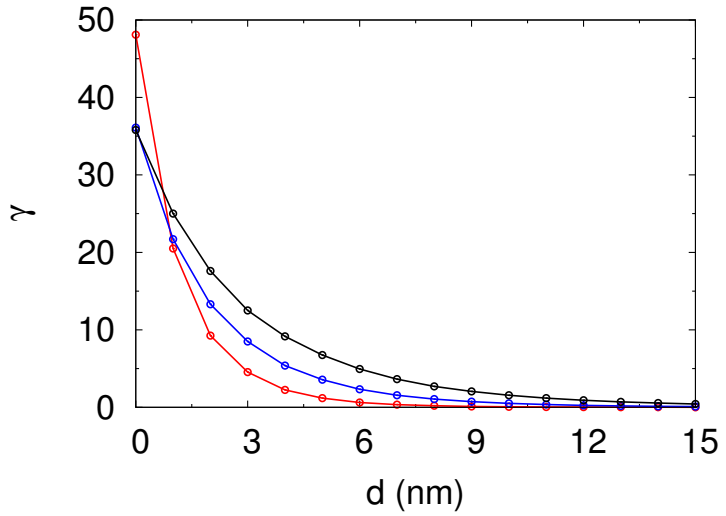

Figure 4-6: **The effective enhancement factor γ as a function of the tip-SWNT distance** The red, blue and black lines are the gold spheres with radius 15 nm, 25 nm and 35 nm, respectively. The He-Ne laser light with the wavelength 633 nm excites the E_{22} transition of the A_2^0 exciton in (8,0) SWNT.

the Raman intensity is proportional to the fourth order of the exciton-optical field matrix element. Therefore, we will approximate the near field and far field Raman intensities as $I_{\rm nf} \propto |M_{\rm ex-nf}|^4$ and $I_{\rm ff} \propto |M_{\rm ex-ff}|^4$, respectively, in this thesis. Then, the effective enhancement factor γ of the Raman intensity can be obtained from $\gamma_{\rm M}$ as $\gamma = \gamma_{\rm M}^4$. In Fig. 4-6, we show the γ as a function of the tip-SWNT distance d for three gold spheres with the radius 15 nm (red line), 25 nm (blue line) and 35 nm (black line) positioned at the distance d above the (8,0) SWNT. Then, The He-Ne laser light with the wavelength 633 nm excites the E_{22} transition of the A_2^0 exciton in (8,0) SWNT. We can see that the maximum of γ is at $d = 0$, and then it decays by increasing d. At $d = 0$, the γ decreases by increasing the radius corresponding to the near field enhancement shown in Fig. 3-2(a). oppositely, at the distance d which is larger than 1 nm, the γ increases by increasing the radius, because the FWHM in the vertical direction increases by increasing the radius leading to the broad decaying of the near field in the vertical direction for the large metallic sphere. The γ sharply decays by increasing d for a small metallic sphere, and the decay length increases by increasing the radius. Therefore, the near field Raman intensity slowly decays by increasing the separation distance d for the large metallic sphere, and it dramatically

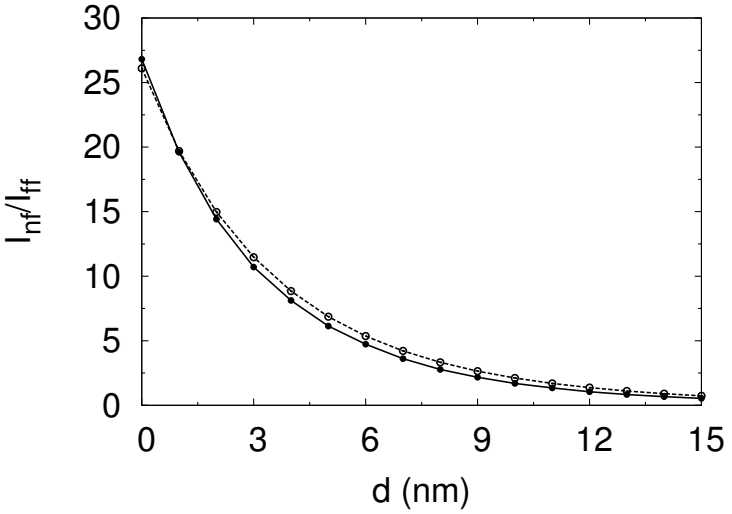

Figure 4-7: **Tip-SWNT distance dependence of** $I_{\rm nf}/I_{\rm ff}$ The dashed line is the $I_{\rm nf}/I_{\rm ff}$ obtained by the fitting function in Eq. (1.8). The solid line is the γ scaled by the factor 0.7. The radius of the gold sphere for the solid line is 40 nm.

decreases by increasing the separation distance d for the very small metallic sphere. Next, let's up compare the tip-SWNT distance dependence of the γ with the fitting function given by L. G. Cancado *et al.* as expressed in Eq. (1.8). In Fig. 4-7, we compare the γ of the 40 nm radius gold sphere denoted by the solid line with the $I_{\rm nf}/I_{\rm ff}$ obtained by the fitting function in Eq. (1.8) denoted by the dashed line. The γ at any distance d is scaled by the factor 0.7. We can see that the decaying trend of the $I_{\rm nf}/I_{\rm ff}$ obtained from the fitting function is close to our model. The fitting function will be more nicely fitted with our model by changing the radius of the gold sphere. The real tip radius used in the TERS experiment obtained by the SEM method is about 15 nm [14] which is much smaller than the radius 40 nm used in our calculation in Fig. 4-7. The reason of this error is because of the FWHM of the near field obtained from the Mie's theory is much smaller than that of the real tip, which results in the fast decay of the near field in the vertical direction.

Chapter 5

Summary

In summary, we have modelled a metallic tip as a metallic sphere with the same radius as the metallic tip in order to obtain the scattered wave radiated from the tip. The solution of the scattered wave is then obtained analytically called Mie's theory. The electric field enhancement EFE at the surface of the metallic sphere is calculated as a function of the wavelength of the laser light and the radius of the metallic sphere. The maximum of the EFE occurs at a small but finite volume sphere due to the dynamic depolarization effect of the dipoles in the metallic sphere. The 18.5 nm radius silver sphere excited by the laser light with the wavelength 350 nm gives the high EFE about 36.6 because of the dipole resonance. We then show the enhancement of the optical transition by formulating the exciton-near field matrix element by taking only the near field along the tube axis into account. The enhancement of the exciton-near field matrix element occurs only within the small region less than the FWHM of the near field. We introduce the effective enhancement factor of the optical matrix element γ_{M} and show that it strongly depends on the radius of the metallic sphere. By using the γ_{M}, we suggest that the gold sphere will give the higher resolution Raman image of the SWNT than that obtained by the silver sphere if the excitation source is the He-Ne laser light with the wavelength 633 nm. Lastly, we show the tip-SWNT distance dependence of the Raman intensity and compare with the experimental fitting function. The decaying trend of the $I_{\mathrm{nf}}/I_{\mathrm{ff}}$ obtained from the experimental fitting function can be reproduced by our model.

Appendix A

In chapter 2, we have seen that solutions of the Maxwell's equations in the spherical coordinate can be solved by the help of the calculus identities listed in the appendix A-1. The differential equations of E_θ, E_ϕ, B_θ and B_ϕ written in term of known E_r in TM mode are derived in the appendix A-2. The associated associated Legendre polynomial and its properties that are used in the boundary conditions to obtain the coefficients of the scattering wave and the internal field in Mie's theory are given in the appendix A-3. The spherical Bessel and the spherical Hankel functions are given in the appendix A-4 to be used in the Mie's theory program.

A.1 Vector calculus in the spherical coordinate

A.1.1 Differential identities in the spherical coordinate

1. Gradient of any scalar ψ in the spherical coordinate is expressed as :

$$\nabla\psi = \hat{e}_r\frac{\partial\psi}{\partial r} + \hat{e}_\theta\frac{1}{r}\frac{\partial\psi}{\partial\theta} + \hat{e}_\phi\frac{1}{r\sin\theta}\frac{\partial\psi}{\partial\phi}. \tag{A.1}$$

2. The scalar Laplacian of any scalar ψ in the spherical coordinate is expressed as :

$$\nabla^2\psi = \frac{1}{r}\frac{\partial^2}{\partial r^2}(r\psi) + \frac{1}{r^2\sin\theta}\frac{\partial}{\partial\theta}(\sin\theta\frac{\partial\psi}{\partial\theta}) + \frac{1}{r^2\sin^2\theta}\frac{\partial^2\psi}{\partial\phi^2}. \tag{A.2}$$

3. The divergence of any vector $\vec{E} = E_r\hat{e}_r + E_\theta\hat{e}_\theta + E_\phi\hat{e}_\phi$ in the spherical coordinate is expressed as :

$$\nabla \cdot \vec{E} = \frac{1}{r^2}\frac{\partial}{\partial r}(r^2 E_r) + \frac{1}{r\sin\theta}\frac{\partial}{\partial\theta}(\sin\theta E_\theta) + \frac{1}{r\sin\theta}\frac{\partial E_\phi}{\partial\phi}. \tag{A.3}$$

4. Curl of any vector $\vec{E} = E_r\hat{e}_r + E_\theta\hat{e}_\theta + E_\phi\hat{e}_\phi$ in the spherical coordinate is expressed as :

$$\nabla \times \vec{E} = \hat{e}_r(\mathrm{curl}\vec{E})_r + \hat{e}_\theta(\mathrm{curl}\vec{E})_\theta + \hat{e}_\phi(\mathrm{curl}\vec{E})_\phi, \tag{A.4}$$

where

$$(\mathrm{curl}\vec{E})_r = \frac{1}{r\sin\theta}\Big[\frac{\partial}{\partial\theta}(\sin\theta E_\phi) - \frac{\partial E_\theta}{\partial\phi}\Big], \tag{A.5}$$

$$(\mathrm{curl}\vec{E})_\theta = \frac{1}{r\sin\theta}\Big[\frac{\partial E_r}{\partial\phi} - \sin\theta\frac{\partial}{\partial r}(rE_\phi)\Big], \tag{A.6}$$

$$(\mathrm{curl}\vec{E})_\phi = \frac{1}{r}\Big[\frac{\partial}{\partial r}(rE_\theta) - \frac{\partial E_r}{\partial\theta}\Big]. \tag{A.7}$$

A.1.2 Vector Laplacian

The vector Laplacian $\nabla^2\vec{E}$ appearing in the vector Helmholtz equation is obtained from the vector identities $\nabla\times(\nabla\times\vec{E}) = \nabla(\nabla\cdot\vec{E}) - \nabla^2\vec{E}$. If $\nabla\cdot\vec{E} = 0$, the vector Laplacian is then calculated from the double curl as $\nabla^2\vec{E} = -\nabla\times(\nabla\times\vec{E})$. The double curl can be expressed as :

$$\nabla\times(\nabla\times\vec{E}) = \hat{e}_r\Big(\mathrm{curl}(\mathrm{curl}\vec{E})\Big)_r + \hat{e}_\theta\Big(\mathrm{curl}(\mathrm{curl}\vec{E})\Big)_\theta + \hat{e}_\phi\Big(\mathrm{curl}(\mathrm{curl}\vec{E})\Big)_\phi, \tag{A.8}$$

where

$$\begin{aligned}\Big(\mathrm{curl}(\mathrm{curl}\vec{E})\Big)_r &= -\frac{1}{r^2}\frac{\partial^2}{\partial r^2}(r^2E_r) - \frac{1}{r^2\sin\theta}\frac{\partial}{\partial\theta}(\sin\theta\frac{\partial E_r}{\partial\theta}) \\ &\quad - \frac{1}{r^2\sin^2\theta}\frac{\partial^2 E_r}{\partial\phi^2},\end{aligned} \tag{A.9}$$

$$\begin{aligned}\Big(\mathrm{curl}(\mathrm{curl}\vec{E})\Big)_\theta &= -\frac{1}{r}\frac{\partial^2}{\partial r^2}(rE_\theta) - \frac{1}{r^2\sin^2\theta}\frac{\partial}{\partial\theta}\Big[\sin\theta\frac{\partial}{\partial\theta}(\sin\theta E_\theta)\Big] \\ &\quad - \frac{1}{r^2\sin^2\theta}\frac{\partial^2 E_\theta}{\partial\phi^2} - \frac{2}{r^2}\frac{\partial E_r}{\partial\theta} - \frac{2}{r^3}\frac{\cos\theta}{\sin\theta}\frac{\partial}{\partial r}(r^2E_r),\end{aligned} \tag{A.10}$$

$$\Big(\text{curl}(\text{curl}\vec{E})\Big)_\phi = -\frac{1}{r}\frac{\partial^2}{\partial r^2}(rE_\phi) - \frac{1}{r^2}\frac{\partial}{\partial\theta}\Big[\frac{1}{\sin\theta}\frac{\partial}{\partial\theta}(\sin\theta E_\phi)\Big] - \frac{1}{r^2\sin^2\theta}\frac{\partial^2 E_\phi}{\partial\phi^2} - \frac{2\cos\theta}{r^2\sin^2\theta}\frac{\partial E_\theta}{\partial\phi} - \frac{2}{r^2\sin\theta}\frac{\partial E_r}{\partial\phi}. \quad \text{(A.11)}$$

It can be seen that only the radial component of $\nabla\times(\nabla\times\vec{E})$ is separable, another two components are coupled with each other and so they are inseparable.

A.2 Differential equations of TM mode

In TM mode, $E_r \neq 0, B_r = 0$. Once E_r has been solved from the vector Helmholtz equation, the differential equations of E_θ, E_ϕ, B_θ and B_ϕ can be written in term of known E_r by considering the Faraday's law and the Maxwell and Ampere's law in Maxwell's equations.

A.2.1 Faraday's law

Faraday's law describes the coupled of the electric and magnetic field, it can be expressed in the spherical coordinate as follow :

$$\begin{aligned} \nabla\times\vec{E} &= i\omega\vec{B}, \\ \hat{e}_r(\text{curl}\vec{E})_r + \hat{e}_\theta(\text{curl}\vec{E})_\theta + \hat{e}_\phi(\text{curl}\vec{E})_\phi &= i\omega(B_\theta\hat{e}_\theta + B_\phi\hat{e}_\phi). \end{aligned} \quad \text{(A.12)}$$

Then, because the unit vectors are linearly independent, three differential equations are obtained by equating two side of Eq. (A.12) :

$$\frac{\partial}{\partial\theta}(\sin\theta E_\phi) - \frac{\partial E_\theta}{\partial\phi} = 0, \quad \text{(A.13)}$$

$$\frac{1}{\sin\theta}\frac{\partial E_r}{\partial\phi} - \frac{\partial}{\partial r}(rE_\phi) = i\omega r B_\theta, \quad \text{(A.14)}$$

$$\frac{\partial}{\partial r}(rE_\theta) - \frac{\partial E_r}{\partial\theta} = i\omega r B_\phi. \quad \text{(A.15)}$$

A.2.2 Ampere and Maxwell law

The Ampere and Maxwell law in the Maxwell equations is expressed in the spherical coordinate as :

$$\begin{aligned} \nabla \times \vec{B} &= -i\varepsilon \frac{k_0}{c} \vec{E}, \\ \hat{e}_r(\mathrm{curl}\vec{B})_r + \hat{e}_\theta(\mathrm{curl}\vec{B})_\theta + \hat{e}_\phi(\mathrm{curl}\vec{B})_\phi &= -i\varepsilon \frac{k_0}{c}(B_r\hat{e}_r + B_\theta\hat{e}_\theta + B_\phi\hat{e}_\phi). \end{aligned} \tag{A.16}$$

Then, using the linearly independent property of the unit vectors, three differential equations are obtained :

$$\frac{1}{\sin\theta}\frac{\partial}{\partial\theta}(\sin\theta B_\phi) - \frac{1}{\sin\theta}\frac{\partial B_\theta}{\partial\phi} = -\frac{ik_0\varepsilon}{c} r E_r, \tag{A.17}$$

$$\frac{\partial}{\partial r}(rB_\phi) = \frac{ik_0\varepsilon}{c} r E_\theta, \tag{A.18}$$

$$\frac{\partial}{\partial r}(rB_\theta) = -\frac{ik_0\varepsilon}{c} r E_\phi. \tag{A.19}$$

A.2.3 Differential equation of E_θ in TM mode

By eliminating B_ϕ from Eq. (A.15) and Eq. (A.18), the differential equation of E_θ in TM mode is obtained as follow :

$$\frac{\partial^2}{\partial r^2}(rE_\theta) + k^2(rE_\theta) = \frac{\partial^2 E_r}{\partial r \partial\theta}. \tag{A.20}$$

A.2.4 Differential equation of E_ϕ in TM mode

By eliminating B_θ from Eq. (A.14) and Eq. (A.19), the differential equation of E_ϕ in TM mode is obtained as follow :

$$\frac{\partial^2}{\partial r^2}(rE_\phi) + k^2(rE_\phi) = \frac{1}{\sin\theta}\frac{\partial^2 E_r}{\partial r \partial\phi}. \tag{A.21}$$

A.2.5 Differential equation of B_θ in TM mode

By eliminating E_ϕ from Eq. (A.14) and Eq. (A.19), the differential equation of B_θ is written as :

$$\frac{\partial^2}{\partial r^2}(rB_\theta) + k^2(rB_\theta) = -\frac{i\varepsilon k_0}{c}\frac{1}{\sin\theta}\frac{\partial E_r}{\partial \phi}. \tag{A.22}$$

A.2.6 Differential equation of B_ϕ in TM mode

By eliminating E_θ from Eq. (A.15) and Eq. (A.18), the differential equation of B_ϕ is then written as :

$$\frac{\partial^2}{\partial r^2}(rB_\phi) + k^2(rB_\phi) = \frac{i\varepsilon k_0}{c}\frac{\partial E_r}{\partial \theta}. \tag{A.23}$$

A.3 The associated Legendre polynomial

In this section, we review the associated Legendre polynomial $P_l^m(x)$ including some important properties used in Mie's theory. $P_l^m(x)$ which are the solutions of the polar part of E_r in TM mode and B_r in TE mode can be obtained from the Legendre polynomial $P_l(x)$ in which m in Eq. (2.31) becomes zero. $P_l(x)$ of each order l can be obtained by the Rodrigues's formula written as

$$P_l(x) = \frac{1}{2^l 2!}\frac{\mathrm{d}^l}{\mathrm{d}x^l}(x^2-1)^l. \tag{A.24}$$

$P_l(x)$ of small order l obtained from Eq. (A.24) are listed below

$$P_0(x) = 1, \tag{A.25}$$

$$P_1(x) = x, \tag{A.26}$$

$$P_2(x) = \frac{1}{2}(3x^2-1), \tag{A.27}$$

$$P_3(x) = \frac{1}{2}(5x^3-3x), \tag{A.28}$$

$$P_4(x) = \frac{1}{8}(35x^4-30x^2+3), \tag{A.29}$$

$$P_5(x) = \frac{1}{8}(63x^5-70x^3+15x), \tag{A.30}$$

where $x = \cos\theta$. Higher order $P_l(x)$ may by obtained using the recursion relation

$$(l+1)P_{l+1}(x) = (2l+1)xP_l(x) - lP_{l-1}(x). \tag{A.31}$$

Then, $P_l^m(x)$ can be obtained from $P_l(x)$ using the following relation

$$P_l^m(x) = (-1)^m(1-x^2)^{m/2}\frac{\mathrm{d}^m}{\mathrm{d}x^m}P_l(x). \tag{A.32}$$

In Mie's theory, we have shown that $m = 1$ for the scattered wave and the internal filed because the incident light is a plane wave traveling in $z-$direction, and the incident electric field is polarized along $x-$direction. We list $P_l^1(\cos\theta)$ of $l = 1, 2, 3, 4, 5$ obtained by substituting Eq. (A.26)-(A.30) into Eq. (A.32) as follows

$$\begin{aligned}
P_1^1(\cos\theta) &= \sin\theta, && \text{(A.33)}\\
P_2^1(\cos\theta) &= 3\sin\theta\cos\theta, && \text{(A.34)}\\
P_3^1(\cos\theta) &= \frac{3}{2}\left(5\cos^2\theta - 1\right)\sin\theta, && \text{(A.35)}\\
P_4^1(\cos\theta) &= \frac{5}{2}\left(7\cos^3\theta - 3\cos\theta\right)\sin\theta, && \text{(A.36)}\\
P_5^1(\cos\theta) &= \frac{15}{8}\left(21\cos^4\theta - 14\cos^2\theta + 1\right)\sin\theta. && \text{(A.37)}
\end{aligned}$$

The important properties of the associated Legendre polynomials are given as follows

1. The relation between the associated Legendre Polynomial and the Legendre Polynomial ($m = 0$) is

$$\frac{\mathrm{d}P_l(\cos\theta)}{\mathrm{d}\theta} = -P_l^1(\cos\theta). \tag{A.38}$$

2. The orthogonalities of the associated Legendre polynomial is expressed as

$$\begin{aligned}
\int_{-1}^{1} P_l^m(x)P_k^m(x)\mathrm{d}x &= \frac{2}{2l+1}\frac{(l+m)!}{(l-m)!}\delta_{kl}, && \text{(A.39)}\\
\int_{-1}^{1} \frac{P_l^m(x)P_l^n(x)}{1-x^2}\mathrm{d}x &= \frac{(l+m)!}{m(l-m)!}\delta_{mn}. && \text{(A.40)}
\end{aligned}$$

3. The integral indentities of the associated polynomials used in Mie's theory :

$$\int_0^\pi \left(\frac{\mathrm{d}P_l^m}{\mathrm{d}\theta}\frac{\mathrm{d}P_k^m}{\mathrm{d}\theta} + m^2\frac{P_l^m}{\sin\theta}\frac{P_k^m}{\sin\theta}\right)\sin\theta\mathrm{d}\theta = \frac{2l(l+1)(l+m)!}{(2l+1)(l-m)!}\delta_{lk}, \quad \text{(A.41)}$$

$$\int_0^\pi \left(\frac{P_l^1}{\sin\theta}\frac{\mathrm{d}P_k^1}{\mathrm{d}\theta} + \frac{P_k^1}{\sin\theta}\frac{\mathrm{d}P_l^1}{\mathrm{d}\theta}\right)\sin\theta\mathrm{d}\theta = 0. \quad \text{(A.42)}$$

A.4 The spherical Bessel and the spherical Hankel functions

The spherical Bessel function $j_l(z)$ and the spherical Hankel function of the first kind $h_l^{(1)}(z)$ can be obtained from the Rayleigh formulas as follows

$$j_l(z) = (-1)^l z^l \left(\frac{1}{z}\frac{\mathrm{d}}{\mathrm{d}z}\right)^l \left(\frac{\sin z}{z}\right), \quad \text{(A.43)}$$

$$h_l^{(1)}(z) = -i(-1)^l z^l \left(\frac{1}{z}\frac{\mathrm{d}}{\mathrm{d}z}\right)^l \left(\frac{e^{iz}}{z}\right), \quad \text{(A.44)}$$

where $i = \sqrt{-1}$.

By using the Rayleigh formulas in Eq. (A.43), the spherical Bessel functions of the order $l = 0$ and $l = 1$ can be expressed as

$$j_0(z) = \frac{\sin z}{z}, \quad \text{(A.45)}$$

$$j_1(z) = \frac{\sin z}{z^2} - \frac{\cos z}{z}. \quad \text{(A.46)}$$

We cal also obtain the spherical Hankel functions of the first kind of the order $l = 0$ and $l = 1$ by using the Rayleigh formulas in Eq. (A.44).

$$h_0^{(1)}(z) = -\frac{ie^{iz}}{z}, \quad \text{(A.47)}$$

$$h_1^{(1)}(z) = \left(-\frac{1}{z} - \frac{i}{z^2}\right)e^{iz}. \quad \text{(A.48)}$$

The higher order spherical Bessel/Hankel functions can be obtained by using the

recurrence relations as follows :

$$f_{l-1}(z) + f_{l+1}(z) = \frac{2l+1}{z} f_l(z), \tag{A.49}$$

$$l f_{l-1}(z) - (l+1) f_{l+1}(z) = (2l+1) f_l^{'}(z), \tag{A.50}$$

where f_l may represent j_l and $h_l^{(1)}$.

The Riccati Bessel functions $\psi_l(z)$ and $\zeta_l(z)$ defined as $\psi_l(z) = z j_l(z)$ and $\zeta_l(z) = z h_l^{(1)}(z)$, respectively, of the higher order ($l > 2$) can be obtained form those of the order $l = 0$ and $l = 1$ by using the recurrence relations, derived from Eq. (A.49)-(A.50), as follows

$$g_{l-1}(z) + g_{l+1}(z) = \frac{2l+1}{z} g_l(z), \tag{A.51}$$

$$(l+1) g_{l-1}(z) - l g_{l+1}(z) = (2l+1) g_l^{'}(z), \tag{A.52}$$

where g_l may represent ψ_l and ζ_l.

Bibliography

[1] A. Jorio, M. Dresselhaus, R. Saito, and G. F. Dresselhaus, *Raman Spectroscopy in Graphene Related Systems*, Wiley-VCH, Germany, 2011.

[2] Ge. G. Samsonidze, et al., J. Nanosci. Nanotech. **3**, 431 (2003).

[3] A. Grüneis, *Resonance Raman spectroscopy of single wall carbon nanotubes*, PhD thesis, Tohoku University, 2004.

[4] Md. T. Chowdhury, *Polarization dependence of X-ray absorption spectra of graphene*, Master thesis, Tohoku University, 2011.

[5] E. B. Barros, et al., Phys. Rep. **431**, 261 (2006).

[6] E. B. Barros, et al., Phys. Rev. B **73**, 241406 (2006).

[7] J. Jiang, et al., Phys. Rev. B **75**, 035407 (2007).

[8] J. Jiang, et al., Phys. Rev. B **75**, 035405 (2007).

[9] R. Saito, G. Dresselhaus, and M. S. Dresselhaus, Phys. Rev. B **61**, 2981 (2000).

[10] A.R.T. Nugraha, *Exciton environmental effect of single wall carbon nanotubes*, Master thesis, Tohoku University, 2010.

[11] Ge. G. Samsonidze, et al., Appl. Phys. Lett. **85**, 5703 (2004).

[12] J. Maultzsch, et al., phys. stat.sol. (b) **243**, 3204 (2006).

[13] A. Hartschuh, et al., Phy. Rev. Lett. **90**, 095503 (2003).

[14] L. G. Cancado, et al., Phy. Rev. Lett. **103**, 186101 (2009).

[15] L. G. Cancado, et al., J. Raman. Sprectrosc. **40**, 1420 (2009).

[16] R. Saito, G. Dresselhaus, and M. S. Dresselhaus, *Physical Properties of Carbon Nanotubes*, Imperial College Press, London, 1998.

[17] N. Peica, et al., Phys. Status. Solidi B **247**, 2818 (2010).

[18] Z. Yang, et al., J. Raman. Sprectrosc. **40**, 1343 (2009).

[19] M. B. Raschke, et al., Appl. Phys. Lett. **83**, 5089 (2003).

[20] A. Hartschuh, Angew. Chem. Int. Ed. **47**, 8178 (2008).

[21] A. Hartschuh, J. Microscopy **210**, 234 (2003).

[22] A. Hartschuh, Phil. Trans. R. Soc. Lond. A **362**, 807 (2004).

[23] S. Kawata, and V. M. Shalaev, *Tip Enhancement : Advances in Nano-Optics and Nano-Photonics*, Elsevier, Amsterdam, 2007.

[24] R. V. Maximiano, et al., Phys. Rev. B **85**, 235434 (2012).

[25] G. Mie, Ann. Phys. **25**, 377 (1908).

[26] M. I. Mishchenko, and L. D. Travis, Bull. Amer. Meteorol. Soc. **89**, 1853 (2008).

[27] J. A. Stratton, *Electromagnetic theory*, IEEE Press, USA, 2007.

[28] C. F. Bohren, and D. R. Huffman, *Absorption and Scattering of Light by small Particles*, Wiley-Interscience, New York, 1983.

[29] J. A. Lock, and G. Gouesbet, JQRST **110**, 800 (2009).

[30] O. L. Muskens, et al., Appl. Phys. Lett **88**, 063109 (2006).

[31] O. Muskens, et al., J. Opt. A: Pure Appl. Opt. **8**, S264 (2006).

[32] T. Klar, et al., Phys. Rev. Lett. **80**, 4249 (1998).

[33] N. W. Ashcroft, and N. D. Mermin, *Solid States Physics*, Thomson Learning, Australia, 1976.

[34] N. G. Christensen, Phys. Rev. B **4**, 3321 (1971).

[35] J. E. Nestell, Jr., and R. W. Christy, App. Opt. **11**

[36] P. B. Johnson, and R. W. Christy, Phys. Rev. B **12**, 4370 (1972).

[37] S. Foteinopoulou, et al., Opt. Express **15**, 4253 (2007).

[38] P. G. Etchegoin, et al., J. Chem. Phys. **125**, 164705 (2006).

[39] S. Kawata, *Near-Field Optics and Surface Plasmon Polaritons*, Springer, Heidelberg, 2001.

[40] J. Vanderlinde, *classical Electromagnetic Theory 2nd ed.*, Kluwer Academic Publishers, Dordrecht , 2010.

[41] M. Meier, and A. Wokaun, Opt. Lett. **8**, 581 (1983).

[42] Y. C. Martin, H. F. Hamann, and H. K. Wickramasinghe, J. Appl. Phys. **89**, 5774 (2001).

[43] G. B. Arfken and H. J. Weber, *Mathematical methods for physicists 5nd ed.*, Harcourt/Academic Press, Florida, 2001.

[44] K. Sato, A. R. T. Nugraha, and R. Saito, e-J. Surf. Sci. Nanotech. **8**, 358 (2010).